Visual Analysis of Second and Third Order Tensor Fields in Structural Mechanics

Von der Fakultät für Mathematik und Informatik
der Universität Leipzig
angenommene

DISSERTATION

zur Erlangung des akademischen Grades

DOCTOR RERUM NATURALIUM
(Dr. rer. nat.)

im Fachgebiet

Informatik

Vorgelegt

von Dipl.-Math. Valentin Zobel

geboren am 7. Oktober 1983 in Kaufbeuren

Die Annahme der Dissertation wurde empfohlen von:

1. Professor Dr. Gerik Scheuermann (Universität Leipzig)
2. Professor Dr. Eugene Zhang (Oregon State University)

Die Verleihung des akademischen Grades erfolgt mit Bestehen
der Verteidigung am 7. Mai 2018 mit dem Gesamtprädikat magna cum laude.

Selbständigkeitserklärung

Hiermit erkläre ich, die vorliegende Dissertation selbständig und ohne unzulässige fremde Hilfe angefertigt zu haben. Ich habe keine anderen als die angeführten Quellen und Hilfsmittel benutzt und sämtliche Textstellen, die wörtlich oder sinngemäß aus veröffentlichten oder unveröffentlichten Schriften entnommen wurden, und alle Angaben, die auf mündlichen Auskünften beruhen, als solche kenntlich gemacht. Ebenfalls sind alle von anderen Personen bereitgestellten Materialen oder erbrachten Dienstleistungen als solche gekennzeichnet.

....
(Ort, Datum)

....
(Unterschrift)

Lebenslauf

Persönliche Daten

Name: Valentin Zobel

Geburtsdatum: 7. Oktober 1983

Geburtsort: Kaufbeuren

Beruflicher Werdegang

07/2013–03/2017	Wissenschaftlicher Mitarbeiter an der Universität Leipzig, Institut für Informatik, Abteilung *Bild- und Signalverarbeitung*
01/2011–06/2013	Wissenschaftlicher Mitarbeiter am Zuse-Institut Berlin, Abteilung *Visualisierung und Datenanalyse*
03/2007–12/2010	Studentische Hilfskraft am Zuse-Institut Berlin, Abteilung *Visualisierung und Datenanalyse*

Studium

04/2005–09/2010	*Mathematik* mit Nebenfach *Informatik* an der TU-Berlin Schwerpunkte: *Geometrie* und *Funktionalanalysis* Spezialisierung in der Informatik: *Computergraphik* Abschluss: Diplom

Publikationen

Diese Arbeit basiert auf den folgenden Publikationen des Autors:

[ZS17] Valentin Zobel and Gerik Scheuermann. Extremal curves and surfaces in symmetric tensor fields. *The Visual Computer*, 2017
`doi.org/10.1007/s00371-017-1450-1`

[ZSS17] Valentin Zobel, Markus Stommel, and Gerik Scheuermann. Visualizing gradients of stress tensor fields. In *Modeling, Analysis, and Visualization of Anisotropy*, pages 65–81. Springer, 2017
`doi.org/10.1007/978-3-319-61358-1_4`

[ZSS15] Valentin Zobel, Markus Stommel, and Gerik Scheuermann. Feature-based tensor field visualization for fiber reinforced polymers. In *2015 IEEE Scientific Visualization Conference (SciVis)*, pages 49–56. IEEE, 2015
`doi.org/10.1109/SciVis.2015.7429491`

[ZRH15] Valentin Zobel, Jan Reininghaus, and Ingrid Hotz. Visualizing symmetric indefinite 2d tensor fields using the heat kernel signature. In *Visualization and Processing of Higher Order Descriptors for Multi-Valued Data*, pages 257–267. Springer, 2015
`doi.org/10.1007/978-3-319-15090-1_13`

[ZRH14] Valentin Zobel, Jan Reininghaus, and Ingrid Hotz. Visualization of two-dimensional symmetric positive definite tensor fields using the heat kernel signature. In *Topological Methods in Data Analysis and Visualization III*, pages 249–262. Springer, 2014
`doi.org/10.1007/978-3-319-04099-8_16`

Danksagung

Mehrere Leute haben zum Gelingen dieser Arbeit beigetragen. Als Erstes möchte ich mich bei Prof. Dr. Gerik Scheuermann bedanken. Während meiner Zeit an der Universität Leipzig sind unter seiner Betreuung die in Kaptitel 3 - 5 beschriebenen Verfahren entstanden. Ohne diverse Anregungen und regelmäßige Diskussionen wäre das vorliegende Ergebnis nicht möglich gewesen.

Aus dem gleichen Grund bedanke ich mich bei Prof. Dr. Ingrid Hotz für die Betreuung während meiner Zeit am Zuse-Institut Berlin. In dieser Zeit ist das Verfahren in Kapitel 6 entstanden, wobei auch Jan Reininghaus sehr viele hilfreiche Anregungen gegeben hat.

Besonderer Dank geht auch an Prof. Dr. Markus Stommel, Inhaber des Lehrstuhls für Kunststofftechnologie der Technischen Universität Dortmund. Fragestellungen aus der Kunststofftechnologie bilden die Grundlage für einen großen Teil dieser Arbeit, ohne den regelmäßigen Austausch und viele wertvolle Hinweise wäre das nicht möglich gewesen. Auch bei Marc Schöneich, Michael Stanko und Jannik Nahrgang vom Lehrstuhl für Kunststofftechnologie bedanke ich mich für die gute Zusammenarbeit und die Bereitstellung diverser Datensätze.

Darüber hinaus möchte ich mich bei sämtlichen Kolleg*inn*en der Abteilung Bild- und Signalverarbeitung der Universität Leipzig sowie der Abteilung Visualisierung und Datenanalyse des Zuse-Instituts bedanken. Bei Fragen konnte ich immer mit Hilfsbereitschaft rechnen. Hervorzuheben sind hier Cornelia Auer und Andrea Kratz, die an ähnlichen Themen gearbeitet haben, sowie Roxana Bujack, Jens Kasten, Stefan Koch, Tom Liebmann und Sebastian Volke, mit denen ich längere Zeit ein Büro geteilt habe.

Schließlich bedanke ich mich ganz besonders bei meiner Familie. Bei Maria für die Unterstützung des gesamten Vorhabens und bei unserem Sohn Nathan für die nötige Ablenkung von der Arbeit.

Zusammenfassung

Tensorfelder erlauben die Beschreibung unterschiedlicher physikalischer Phänomene und sind in vielen verschiedenen Anwendungsgebieten von großer Bedeutung. Beispiele sind Diffusionstensoren, mit welchen sich die Bewegung von Wassermolekülen im menschlichen Gehirn untersuchen lässt, oder Spannungstensoren, welche den Spannungszustand von Bauteilen unter Last charakterisieren. Die Gewinnung von Tensorfeldern kann durch Messung erfolgen, zum Beispiel bei Diffusionstensoren durch diffusionsgewichtete Magnetresonanztomographie, oder durch numerische Simulationen, was bei Spannungstensoren üblicherweise der Fall ist. Durch die Fülle an Informationen, die in einem Tensorfeld enthalten sind, gestaltet sich die Analyse der resultierenden Daten als sehr schwierig. In dieser Arbeit werden vier neue Verfahren zur Analyse und Visualisierung von Tensorfeldern präsentiert. Im Mittelpunkt stehen dabei Tensorfelder, die im Rahmen strukturmechanischer Simulationen auftreten.

Das erste Verfahren befasst sich mit einer spezifischen Anwendung im Maschinenbau, und zwar dem Entwurf von Bauteilen aus kurzfaserverstärkten Kunststoffen, die im Spritzgussverfahren hergestellt werden. Bei derart gefertigten Bauteilen hängt die Stabilität von den Faserorientierungen ab, welche durch den Fertigungsprozess beeinflusst werden. Aus diesem Grund werden die unter Last auftretenden Spannungen sowie die Faserorientierungen analysiert. Die Spannungen und Faserorientierungen sind jeweils als Tensorfelder gegeben, diese werden mithilfe von Struktursimulationen bzw. Simulationen des Spritzgussprozesses berechnet. Für die Analyse der Tensorfelder werden vier Merkmale definiert, welche das Bauteil in rote, orange, gelbe und grüne Bereiche unterteilen. Rote und orange Bereiche bedeuten, dass das Bauteil hier der Belastung nicht standhalten wird, wobei im Fall von orange ein Versagen durch eine geeignetere Faserorientierung vermieden werden kann. Gelbe und grüne Bereiche geben an, dass kein Versagen zu erwarten ist, wobei gelbe Bereiche bei geänderter Faserorientierung versagen könnten. Für eine detaillierte Analyse der gelben und orangen Bereiche wurde ein Glyph entwickelt, welcher die zulässigen Faserorientierungen sowie die gegebene Faserorientierung darstellt. Mit diesen Visualisierungen kann der Ingenieur die gegebene Faserorientierung bewerten und bekommt Hinweise zur Verbesserung der Faserorientierung.

Viele Versagenskriterien berücksichtigen nur die Spannung an einem einzelnen Punkt. Es gibt allerdings Hinweise, dass die Stabilität eines Materials auch vom Verlauf der Spannung in der näheren Umgebung beeinflusst wird. Daher ist ein genaues Verständnis des Spannungsgradienten erstrebenswert. Das zweite Verfahren stellt Gradienten von Spannungstensoren mit Hilfe von Glyphen dar. Gradienten von Spannungstensoren sind Tensoren dritter Ordnung, die Darstellung stellt daher eine besondere Herausforderung dar und wurde bisher kaum untersucht. Um die Interpretation zu erleichtern dienen gebräuchliche Darstellungen des Spannungstensors als Ausgangspunkt für das Design der Glyphen. Neben einem Glyph, der sämtliche Informationen des Gradienten darstellt, werden mehrere Vereinfachungen diskutiert, die es dem Anwender erlauben bestimmte Eigenschaften des Spannungsgradienten leichter zu erfassen.

Von Tensorfeldern abgeleitete skalare Größen, die invariant unter Transformationen des Koordinatensystems sind, spielen in vielen Anwendungen eine wichtige Rolle. Die geeignete Auswahl solcher Invarianten ist allerdings häufig schwierig und hängt stark von der Anwendung ab. Das Ziel des dritten Verfahrens ist es daher, den gesamten invarianten Teil des Tensorfeldes zu analysieren. Hierzu wird der Begriff „extremaler Punkt“ eingeführt. Ein extremaler Punkt ist dadurch charakterisiert, dass es eine skalare Invariante gibt, welche an dieser Stelle einen kritischen Punkt hat, also ein Minimum, Maximum oder Sattelpunkt. Darüber hinaus wird gezeigt, dass die Extrema diverser gebräuchlicher Invarianten in der Menge der extremalen Punkte enthalten sind. Die resultierenden Linien im Fall von zweidimensionalen Tensorfeldern, beziehungsweise Flächen im dreidimensionalen Fall, dienen dementsprechend als wichtige Merkmale des invarianten Anteils des Tensorfeldes.

Im letzten vorgestellten Verfahren wird die Heat Kernel Signature (HKS) zur Visualisierung von Tensorfeldern verwendet. Die HKS wird aus dem Wärmeleitungskern (heat kernel) berechnet und wurde ursprünglich für Flächen entwickelt. Es handelt sich um eine zeitabhängige Funktion auf der Fläche, welche die Metrik auf der Fläche unter schwachen Voraussetzungen vollständig charakterisiert, d. h. die Form der Fläche wird bis auf isometrische Verformungen exakt bestimmt. Für kleine Zeitwerte sind die Werte der HKS der gaußschen Krümmung sehr ähnlich. Diese Eigenschaften machen die Anwendung der HKS auf Tensorfelder sehr interessant. Die Tatsache, dass jedes positiv definite Tensorfeld als Metrik einer riemannschen Mannigfaltigkeit aufgefasst werden kann, erlaubt eine direkte Anwendung der HKS. Es wird ein auf Tensorfelder angepasstes Berechnungsverfahren mit Hilfe der Finite-Elemente-Methode vorgestellt. Auch indefinite Tensorfelder können nach Abbildung auf positiv definite Tensorfelder mit Hilfe der HKS visualisiert werden.

Abstract

Tensor fields allow for the description of different physical phenomenons and they are of great importance in various applications. Examples are diffusion tensors, which are used to investigate the motion of water molecules in the human brain, or stress tensors, which characterize the state of stress of a component under load. Tensor fields can be obtained by measurements, e. g. by diffusion-weighted magnetic resonance imaging in case of diffusion tensors, or by numerical simulations, which is the usual case for stress tensors. Due to the wealth of information which is contained in a tensor field, the analysis of the resulting data is a very difficult task. In this work, four new methods for the analysis and visualization of tensor fields are presented. The focus is on tensor fields which arise in the context of structural mechanics simulations.

The first method deals with a specific application in mechanical engineering, namely the design of components made of short fiber reinforced polymers using injection molding. For components manufactured this way the stability depends on the fiber orientations, which are affected by the production process. For this reason, the stresses under load as well as the fiber orientations are analyzed. The stresses and the fiber orientations are each given as tensor fields, these are computed by structure simulations and simulations of the injection process, respectively. For the analysis of the tensor fields four features are defined which subdivide the component into red, orange, yellow and green regions. Red and orange regions mean that the component will not resist the load here, while in case of orange failure can be avoided by a more suitable fiber orientation. Yellow and green regions indicate that no failure is expected, while yellow regions might fail for a modified fiber orientation. For an in depth analysis of the yellow and orange regions a glyph was developed, which shows the admissible fiber orientations as well as the given fiber orientation. With these visualizations the engineer can rate a given fiber orientation and gets hints for improving the fiber orientation.

Many failure criteria consider only the stress at a singe point. However, there is some evidence that the stability of a material is also influenced by the progression of the stress within the closer neighborhood. Thus a thorough understanding of the stress gradient is desirable. The second method depicts gradients of stress tensors

using glyphs. Gradients of stress tensors are third order tensors, the visualization is therefore a great challenge and there is very little research on this subject so far. To simplify the interpretation, common depictions of the stress gradient serve as basis for the glyph design. Besides a glyph showing the complete information of the gradient, several simplifications are discussed, which allow the user to grasp certain properties of the stress gradient more easily.

Scalar quantities derived from tensor fields which are invariant under transformations of the coordinate system play an important role in many applications. However, the proper selection of such invariants is often difficult and depends strongly on the application. Thus the objective of the third method is to analyse the complete invariant part of the tensor field. For this, the notion of ”extremal point” is introduced. An extremal point is characterized by the fact that there is a scalar invariant which has a critical point at this position, i. e. a minimum, maximum, or a saddle point. Moreover it will be shown that the extrema of several common invariants are contained in the set of critical points. The resulting lines or surfaces in case of two- or three-dimensional tensor fields, respectively, serve consequently as important features of the invariant part of a tensor field.

The last method presented in this work uses the Heat Kernel Signature (HKS) for the visualization of tensor fields. The HKS is computed from the heat kernel and was originally developed for surfaces. It is a time dependent function on the surface, which completely characterizes the metric of the surface under weak assumptions, i. e. the shape of the surfaces is determined exactly up to isometric deformations. For small time values the values of the HKS are very similar to the Gaussian curvature. These properties make the application of the HKS on tensor fields very interesting. The fact that every positive definite tensor field can be considered as the metric of a Riemannian manifold allows for the direct application of the HKS. The computation is adapted to tensor fields using the finite element method. Also indefinite tensor fields can be visualized by the HKS after a mapping to positive definite tensor fields.

Contents

1

Introduction

1.1 Motivation

Tensor fields serve as a generalization of scalar and vector fields. They are widely studied in mathematics and physics, notably in differential geometry, general relativity, and continuum mechanics. There are many applications including engineering, geology, and medicine. In practice, tensor fields are usually obtained by computer simulations or measurements. But understanding the resulting data remains a difficult task. The visualization of these fields is challenging, even for the relatively simple, but frequent case of a symmetric tensor field of second order. In case of three dimensions, which is most relevant for practical applications, a symmetric tensor field of second order consists of six independent components. Consequently, six scalar values have to be taken into consideration to depict the complete tensor information at a single point of the dataset. The number of components increases rapidly for higher order tensors; a three-dimensional third order tensor without any symmetries consists of 27 independent components. The situation is easier for two-dimensional tensor fields, but even a symmetric tensor field of second order has three independent components.

Several methods for the visualization of symmetric tensor fields of second order have been developed in recent years. According to the survey by Kratz et al. [KASH13] most methods for the visualization of tensor fields fall into one of the following three categories: local methods, continuous methods, or methods for tensor field segmentation. Local methods depict tensors by a geometric object which is usually referred to as glyph. Several different types of glyphs have been developed, see for example [HYW$^+$03] or [SK10]. Glyphs are able to reflect all or at least most of the tensor information at discrete points. But different properties of the tensor are emphasized by different glyphs, thus the choice depends on the application. In order to reveal the global structure of the field, intelligent strategies for glyph placement are necessary. Moreover, such methods are usually restricted to two-dimensional subsets, see for example [HSH07], [KfW06], [KKH11]. Thus, first a proper selection of two-dimensional subsets is necessary. Otherwise, glyphs are strongly affected by the problem of occlusion for three-dimensional tensor fields.

Consequently, glyphs are more suitable for a detailed analysis of the tensor field, while the objective of continuous methods is to give an overview and to reveal global structures of the field. This is achieved by a reduction of the tensor information to derived quantities. In many cases scalar quantities are considered, possible choices include single eigenvalues, the trace, or more application specific quantities like the von Mises stress in case of stress tensors. Once such a scalar quantity is chosen, one can use methods for the visualization of scalar fields. In addition to deriving scalar quantities, also the eigenvector fields are frequently analyzed. This allows for the adaption of methods for vector field visualization, but some caution is necessary as the direction of eigenvectors is not uniquely defined. The most prominent example are tensor lines which are the integral lines of the eigenvectors. Such methods are suitable if it is sufficient to consider only a portion of the tensor, e. g. the usefulness of tensor lines is demonstrated in [KSZ$^+$14]. It is possible to analyse multiple derived quantities succesively, see for example [DGBW09]. A combination of different quantities is proposed in [HFH$^+$04] where the eigenvectors and eigenvalues of two-dimensional tensor fields are combined to fabric structures.

Tensor field segmentation aims at a partition of the field into regions with specific properties. Tensor field topology is certainly the best known method, see [DH94], [TSH01], [ZP04], [ZPP05a], [ZPP05b]. The tensor field topology consists of degenerate points and separating lines for two-dimensional tensor fields. In three dimensions the degenerate points form curves, additionally we obtain separating surfaces. This leads to complex structures that are difficult to compute. Degenerate points can be considered as singularities in the eigenvector field, while the separating lines or surfaces partition the field into regions with qualitative similar behavior of the eigenvector field. Consequently the tensor field topology is primarily suited for the analysis of the eigenvector fields. The only information on the eigenvalues is that degenerate points are characterized by repeating eigenvalues. Other segmentation methods for tensor fields use similarity measures and classical clustering methods, see for example [dLGALW09].

In this work, four new methods for the analysis of tensor fields are presented. The main focus is on tensor fields arising in the context of structural mechanics, especially stress tensor fields. First, the necessary theoretical background on tensor fields is provided in Chapter 2. The method proposed in Chapter 3 is motivated by a specific application, that is the design of technical components made from short fiber reinforced polymers. For simpler materials, material failure can be predicted from the stress tensor only by using yield criteria like the von Mises stress. In case of fiber reinforced polymers, the material property is determined by the fiber distribution at every position, and the fiber orientation can be influenced by the production process. The fiber orientation is often described as a tensor field. Thus a new method for combining the stress field and the fiber orientation field becomes necessary. Different features are defined which indicate if the material fails and if failure is affected by the fiber orientation. Moreover, a glyph is developed that informs of the current fiber orientation and the desired fiber orientation, which depends on the stresses. This leads to a feature-based visualization to provide an overview, while an application specific glyph is used for a detailed analysis. The resulting visualizations inform the engineer about potential improvements in the product development which can be achieved by modifying the fiber orientation.

The visualizations suggested in Chapter 4 are also motivated by the prediction of failure. In some applications, it is necessary to look into gradients of (symmetric) second order tensor fields. These tensors are of third order. In three-dimensional space, we have 18 independent coefficients at each position, so the visualization of these fields provides a major challenge. A particular case are stress gradients in structural mechanics. There are specific situations where the stress gradient is required together with the stress to study material behavior. Since the visualization community lacks methods to show these fields, some preliminary ideas to design appropriate glyphs are considered. The design of a first glyph is motivated by typical depictions of stress in engineering textbooks. This glyph contains the complete information of the stress gradient. Subsequently, simplified glyphs are considered, which are able to emphasize certain properties of the stress gradient.

As mentioned above, many applications rely on the analysis of scalar quantities. Such quantities are usually invariant with respect to changes of the coordinate system. Consequently they are also called invariants and can be defined as functions depending on the eigenvalues. However, it is often not obvious which scalar invariant reflects the relevant properties of a tensor field. Thus it is desirable to analyze the complete invariant part of the field at once. This is achieved by introducing the notion of extremal points in Chapter 5. Each extremal point of the tensor field is the extremum of a certain scalar invariant. Conversely, the extrema of several widely used scalar invariants are contained in the set of extremal points, as well as the degenerate points of a tensor field. In general, the extremal points form curves in case of two-dimensional tensor fields and surfaces in case of three-dimensional tensor field. They serve as lower dimensional structures characterizing the invariant part of the tensor field. Although the degenerate points are a subset of the extremal points, this approach can be considered complementary to the tensor field topology. The tensor field topology analyzes primarily the behavior of the eigenvectors, while the invariant part is defined by the eigenvalues of the tensor field.

In Chapter 6 the Heat Kernel Signature (HKS) is proposed for the visualization of two-dimensional tensor fields. The HKS was originally introduced as an isometry invariant shape signature [SOG09], it is a scalar quantity which is derived from the heat kernel of a surface. From a more general point of view, the HKS characterizes the metric of an arbitrary Riemannian manifold. A symmetric positive definite tensor field can be interpreted as the metric of a Riemannian manifold, thus the HKS can be used to visualize and analyze such tensor field. The HKS is closely related to the Gaussian curvature of the Riemannian manifold and the time parameter of the heat kernel allows for a level of detail analysis of tensor fields. This makes the HKS an interesting new scalar quantity derived from tensor fields, which differs significantly from usual tensor invariants. In order to use the HKS for the visualization of indefinite tensor fields, like the stress tensor, bijective mappings can be applied on the tensor field to obtain a positive definite tensor field.

1.2 Related Work

This section briefly states some publications which are related to the methods or applications considered in this thesis. For a comprehensive overview on visualization methods for tensor fields see again the state of the art report by Kratz et al. [KASH13] and the references therein.

Stress Tensors

The most important application in this thesis is the analysis of stress tensor fields, which serve as examples for all proposed methods. Especially the methods in Chapter 3 and 4 are motivated by the analysis of stress tensor fields which are obtained from structure simulations performed in engineering. Although stress tensor fields are prevalent in structure simulations, they are mostly considered as intermediate results. Usually the focus is on the derivation of scalar quantities without fully utilizing the tensor information. As a consequence, most visualization methods used in engineering are limited to basic visualizations of scalar fields, often restricted to two-dimensional slices. Sometimes also the major eigenvectors are plotted on grid points.

More advanced visualization methods for stress tensor fields from structure simulations are used by Kratz et al. [KSZ$^+$14]. Similar to the method in Chapter 3, the objective of this work is to improve the stability of a component without changing its weight and hence production cost. However, this is achieved by optimizing the geometry of the component, not the fiber orientations. Tensor lines are considered as major load paths and rib structures are constructed along tensor lines. These rib structures outperform the rib structure that was constructed according to best practice in mechanical engineering.

Another article focussing on stress tensor fields in a particular application is [JSF$^+$02], where stress tensor fields are considered in a geomechanical context. Different methods for the visualization of stress tensors are discussed, this includes glyphs, scalar quantities and hyperstreamlines, which are an advanced version of tensor lines.

In [DGBW09] stress tensor fields are analyzed for implant planning in orthopedics. Tensor lines visualizing the stress directions are combined with volume renderings of scalar quantities like the normal stress. Advanced rendering methods are proposed in order to improve perception.

Gradients of Tensors

In Chapter 4 visualizations of the gradient of the stress tensor are proposed. There seems to be very few work on the visualization of tensor gradients. Kriz et al. [KYHR05] visualize the gradients of a stress tensors at single points by showing a collection of ellipsoids as glyphs for second order tensors. One glyph represents the stress at the considered position itself, additional glyphs show the stress in nearby positions in the direction of the coordinate axes. The user can guess the gradient by comparing these glyphs.

Kindlmann et al. [KEWW07] analyze the gradients of diffusion tensors by examining gradients of scalar quantities derived from the tensor. The gradient of a tensor field is characterized by the gradients of three tensor invariants, as well as three rotation tangents describing the variation of the tensor orientation. For the visualization, the magnitudes of the gradients are shown by grayscale images.

Tensor Invariants

The extremal points suggested in Chapter 5 are computed from sets of invariants, which characterize the invariant part of the tensor. Besides the eigenvalues and the principal invariants, we make use of two other sets of invariants. The first one consisting of trace, norm of the deviator and tensor mode, the second one consisting of norm, fractional anisotropy and tensor mode. These invariants are investigated by Ennis et al. in [EK06]. As mentioned above, the gradients of these invariants are considered by Kindlmann et al. in [KEWW07].

Similarly as in Chapter 5, Palacios et al. [PYW$^+$16] use common invariants to extract feature surfaces. Neutral and traceless surfaces are defined as the surfaces where the tensor mode or the trace vanishes, respectively. This is in a way complementary to the extremal points presented in Chapter 5. While extremal points represent points where invariants become extremal, these feature surfaces mark transition points of the tensor field with respect to the considered invariants.

Tensor Field Topology

As mentioned above, the tensor field topology aims at analyzing the global behavior of the eigenvector fields. Thus it is complementary to methods based on the analysis of tensor invariants, since the eigenvectors are independent from the invariant part of a tensor. The topology of two-dimensional tensor fields is described by Delmarcelle and Hesslink in [DH94]. An extension to two-dimensional time dependent tensor fields and a simplification method is proposed by Tricoche et al. in [TSH01] and [TS04], respectively. The computation of degenerate curves in three-dimensional tensor fields is treated by Zheng et al. in [ZP04] and [ZPP05b]. Separating surfaces of three-dimensional tensor fields are considered by Zheng et al. in [ZPP05a], but most work using tensor field topology for three-dimensional tensor fields is limited to degenerate curves.

Tensor Glyphs

Glyphs are widely used for the visualization of tensor fields. In Chapter 3 glyphs for the simultaneous visualization of the stress tensor and the fiber orientation tensor are suggested, in Chapter 4 glyphs are used for visualizing the gradient of the stress tensor.

A comparison of different types of tensor glyphs is given given by Hashash et al. in [HYW+03]. Additionally a glyph focusing on the visualization of the shear stresses is provided. Superquadrics for positive definite tensor fields are introduced by Kindlmann in [Kin04], an extension to indefinite tensors is proposed in [SK10]. The state of the art report by Borgo et al. [BKC+13] gives general design guidelines for glyphs as well as strategies for glyph placement. A placement strategy similar to the method proposed in Chapter 3 is described by Brambilla et al. in [BAH13].

2

Mathematical Foundations on Tensor Fields

This chapter provides the mathematical foundations on tensors and tensor fields which are needed in the remainder of this thesis. Basic properties of tensors and tensor fields are briefly discussed in Section 2.1 and 2.2. More details can be found in several textbooks on differential geometry, see for example [BG68] or [Boo86]. For another short introduction see also [HG06]. Scalar invariants of symmetric second order tensors are discussed in Section 2.3, they are particularly important in Chapter 5. Two tensors which play an important role in this thesis are the stress tensor and the fiber orientation tensor, they are discussed in Sections 2.4 and 2.5, respectively.

2.1 Tensors on Vector Spaces

2.1.1 Definition and Basic Properties

Let V be a d-dimensional vector space over $\mathbb{R}$ and V^* its dual space. The dual space V^* is the set of linear functions from V to $\mathbb{R}$, which are also called covectors. A *tensor of type* (r,s) *on* V is a multilinear map

$$T : \underbrace{V \times \cdots \times V}_{r} \times \underbrace{V^* \times \cdots \times V^*}_{s} \to \mathbb{R}$$

taking r elements of V and s elements of V^* to a real number. The numbers r and s are called the *covariant order* and *contravariant order* of the tensor T, respectively. Sometimes we speak also of d-dimensional tensors, indicating that the dimension of the underlying vector space V is d. The set of tensors of type (r,s) forms a vector space which is denoted by $\mathcal{T}_r^s(V)$. Tensors of type $(r,0)$ are also called covariant tensors, while tensors of type $(0,s)$ are called contravariant tensors. The respective spaces of tensors are denoted by $\mathcal{T}_r(V)$ and $\mathcal{T}^s(V)$.

In practice, tensors are usually given by its components, which form $(r+s)$-dimensional arrays. Let $\{e_1,\dots,e_d\}$ be a basis of V and $\{\varepsilon^1,\dots,\varepsilon^d\}$ its dual basis, i. e. a basis of V^* with $\varepsilon^j(e_i)=\delta_i^j$. The value of δ_i^j is 1 for $i=j$ and 0 otherwise, it is usually referred to as Kronecker delta. The *components* of T with respect to these bases are now given by

$$T_{i_1,\dots,i_r}^{j_1,\dots,j_s}=T(e_{i_1},\dots,e_{i_r},\varepsilon^{j_1},\dots,\varepsilon^{j_s}) \ , \quad i_1,\dots,i_r,j_1,\dots,j_s\in\{1,\dots,d\} \ .$$

The lower indices are the covariant indices, the upper indices are the contravariant indices. A tensor is uniquely defined by its components with respect to a basis and its dual basis. For a tensor of type (r,s) we have $(r+s)d$ components, consequently $\mathcal{T}_r^s(V)$ can be identified with $\mathbb{R}^{(r+s)d}$. In this thesis, tensors will be mostly given by its components.

Next we study how to evaluate a tensor if the arguments, which are vectors and covectors, and the tensor itself are given by its components. Let $v_1,\dots,v_r\in V$ be vectors and $\alpha^1,\dots,\alpha^s\in V^*$ covectors given by its components with respect to the chosen basis and its dual basis, i. e.

$$v_1=v_1^{i_1}e_{i_1} \ , \quad \dots \ , \quad v_r=v_r^{i_r}e_{i_r} \ , \quad \alpha^1=\alpha_{j_1}^1\varepsilon^{j_1} \ , \quad \dots \ , \quad \alpha^s=\alpha_{j_s}^s\varepsilon^{j_s} \ .$$

Note that we use the Einstein summation convention here, which implies summation if an index occurs twice. The sum ranges over all possible values of that index, in our case the sum runs over $\{1,\dots,d\}$, e. g.

$$v_1^{i_1}e_{i_1}=\sum_{i_1=1}^{d}v_1^{i_1}e_{i_1} \ .$$

This results in double, triple, etc. sums if there are multiple indices occuring twice. Also note that we have used lower indices for the components of vectors and upper indices for the components of covectors. This is consistent with the upper and lower indices of tensor components. A covector $\alpha\in V^*$ is a tensor of type $(1,0)$. A vector $v\in V$ can be identified with a tensor of type $(0,1)$ as it defines a linear map

$$V^*\to\mathbb{R} \ , \quad \alpha\mapsto\alpha(v) \ ,$$

this is the canonical identification of V with V^{**}. Now we obtain by the multilinearity of T

$$\begin{aligned} T(v_1, \dots, v_r, \alpha^1, \dots, \alpha^s) &= T(v_1^{i_1} e_{i_1}, \dots, v_r^{i_r} e_{i_r}, \alpha^1_{j_1} \varepsilon^{j_1}, \dots, \alpha^s_{j_s} \varepsilon^{j_s}) \\ &= v_1^{i_1} \dots v_r^{i_r} \alpha^1_{j_1} \dots \alpha^s_{j_s} T(e_{i_1}, \dots, e_{i_r}, \varepsilon^{j_1}, \dots, \varepsilon^{j_s}) \\ &= v_1^{i_1} \dots v_r^{i_r} \alpha^1_{j_1} \dots \alpha^r_{j_s} T^{j_1, \dots, j_s}_{i_1, \dots, i_r} \ . \end{aligned} \tag{2.1}$$

Similaraly to equation (2.1) we obtain the formula for the transformation of the components of a tensor under a change of basis. Let $\{\tilde{e}_1, \dots, \tilde{e}_d\}$ be another basis of V and $\{\tilde{\varepsilon}^1, \dots, \tilde{\varepsilon}^d\}$ its dual basis. Then there are change of basis matrices $B = [b_i^k]$ and $C = [c_l^j]$ such that

$$\tilde{e}_i = b_i^k e_k \ , \quad \tilde{\varepsilon}^j = c_l^j \varepsilon^l \ . \tag{2.2}$$

Note that C is the inverse matrix of B, i. e. $C = B^{-1}$. Now the components $\tilde{T}^{j_1, \dots, j_s}_{i_1, \dots, i_r}$ of T with respect to the new bases are given by

$$\begin{aligned} \tilde{T}^{j_1, \dots, j_s}_{i_1, \dots, i_r} &= T(\tilde{e}_{i_1}, \dots, \tilde{e}_{i_r}, \tilde{\varepsilon}^{j_1}, \dots, \tilde{\varepsilon}^{j_s}) \\ &= T(b^{k_1}_{i_1} e_{k_1}, \dots, b^{k_r}_{i_r} e_{k_r}, c^{j_1}_{l_1} \varepsilon^{l_1}, \dots, c^{j_s}_{l_s} \varepsilon^{l_s}) \\ &= b^{k_1}_{i_1} \dots b^{k_r}_{i_r} c^{j_1}_{l_1} \dots c^{j_s}_{l_s} T(e_{k_1}, \dots, e_{k_r}, \varepsilon^{l_1}, \dots, \varepsilon^{l_s}) \\ &= b^{k_1}_{i_1} \dots b^{k_r}_{i_r} c^{j_1}_{l_1} \dots c^{j_s}_{l_s} T^{l_1, \dots, l_s}_{k_1, \dots, k_r} \ . \end{aligned} \tag{2.3}$$

This is the *transformation law* for tensors of type (r, s). It ensures that a tensor given by its components is independent of the chosen coordinate system.

In this thesis, we have mostly $V = \mathbb{R}^d$ equipped with the standard inner product $\langle \cdot \, , \cdot \rangle$. Moreover, we work with an orthonormal basis of $\mathbb{R}^d$. In this case it is not necessary to distinguish covariant and contravariant indices of tensor components. Since the map $v \mapsto \langle v \, , \cdot \rangle$ defines an isomorphism from V to V^*, we can identify V with V^*. Additionally, this isomorphism maps an orthonormal basis $\{e_1, \dots, e_d\}$ to its dual basis $\{\varepsilon^1, \dots, \varepsilon^d\}$ of V^*. This implies that a vector is mapped to a covector with the same components, and the change of basis matrices B and C defined in equation (2.2) satisfy $c_i^j = b_j^i$ or in matrix notation $C^\top = B$. Consequently, according to equation (2.3), the components of a tensor transform in the same way for covariant and contravariant indices. Thus it is not necessary to distinguish lower and upper indices of tensor components. We restrict ourselves from now on mostly to tensors of type $(r, 0)$ on $\mathbb{R}^d$, denoted by $\mathcal{T}_r(\mathbb{R}^d)$, which will be simply called (d-dimensional) tensors of order r. The most frequent case in this work will be two- or three-dimensional second order tensors ($r = 2$), furthermore we encounter third order ($r = 3$) and fourth order ($r = 4$) tensors.

2.1.2 Reinterpretation of Tensors

In many applications tensors are not interpreted as multilinear maps as defined above. For instance, second order tensors can be considered as linear maps from $\mathbb{R}^d$ to $\mathbb{R}^d$, represented by matrices in $\mathbb{R}^{d,d}$. This is a common interpretation of tensors in engineering or physics, an example is the stress tensor studied in Section 2.4.

A forthright way to reinterpret a second order tensor T as a linear map is to evaluate T with respect to the second variable while the rest is left unaltered. Let $v \in \mathbb{R}^d$ be a vector, then $T_{ij}v^j$ for $i = 1, \ldots, d$ define the components of a vector in $\mathbb{R}^d$, in this way we obtain a linear map $\mathbb{R}^d \to \mathbb{R}^d$. This linear map is represented by the matrix $[T_{ij}] \in \mathbb{R}^{d,d}$ defined by the components of T. We will usually consider second order tensors as linear maps in the remainder of this work. Moreover, we denote the linear map also simply by T, i. e.

$$T \ : \ \mathbb{R}^d \to \mathbb{R}^d \ , \quad v \mapsto Tv \ .$$

It will be clear from the context if T is considered as linear or multilinear map. Consequently, all properties of linear maps are also defined for tensors of second order. For example, we will frequently make use of the eigenvalues and eigenvectors of second order tensors.

Evaluating a tensor with respect to some of its variables leads to a general concept of reinterpreting tensors. A third order tensor can be evaluated with respect to one variable, e. g. $T_{ijk}v^i$ or $T_{ijk}v^k$. This defines linear maps $\mathbb{R}^d \to \mathcal{T}_2(\mathbb{R}^d)$ taking $v \in \mathbb{R}^d$ to a second order tensor or, equivalently, to a matrix in $\mathbb{R}^{d,d}$. Alternatively, a third order tensor can be evaluated with respect to two variables, e. g. $T_{ijk}v^j w^k$, defining a bilinear map $\mathbb{R}^d \times \mathbb{R}^d \to \mathbb{R}^d$. Analogously, this method can be continued for tensors of arbitrary order r, taking m elements of $\mathbb{R}^d$ to a tensor of order $r - m$.

Note that we need to be more careful with the reinterpretation of tensors if the components of T are not given with respect to an orthonormal basis. For instance, evaluating a tensor T of type $(2, 0)$ with respect to the second variable defines a map

$$\mathbb{R}^d \to \mathcal{T}_1(\mathbb{R}^d) = (\mathbb{R}^d)^* \ , \quad v \mapsto T(\cdot\, , v) \ ,$$

rather than a map $\mathbb{R}^d \to \mathbb{R}^d$ as claimed above. Accordingly, the components $T_{ij}v^j$ are the components of a covector, as indicated by the lower index i. Strictly speaking, only a tensor of type $(1, 1)$ can be reinterpreted as a linear map $\mathbb{R}^d \to \mathbb{R}^d$, since such a tensor defines a map

$$\mathbb{R}^d \to \mathcal{T}^1(\mathbb{R}^d) = (\mathbb{R}^d)^{**} \ , \quad v \mapsto T(v, \cdot) \ ,$$

while $(\mathbb{R}^d)^{**}$ can be canonically identified with $\mathbb{R}^d$. This becomes also apparent from the fact, that the components of tensors of type $(1, 1)$ transform like linear maps under an arbitrary change of basis. Using matrix notation, equation (2.3) can be written as $\tilde{T} = B^{-1}TB$ for a change of basis matrix B. In contrast, for tensors of type $(2,0)$ equation (2.3) becomes $\tilde{T} = B^{\top}TB$. But, as discussed above, when using orthonormal bases we do not need to distinguish between covariance and contravariance, i. e. between lower and upper indices. Also the components transform properly when changing between orthonormal bases, since in this case the change of basis matrix B is orthogonal, i e. we have $B^{-1} = B^{\top}$.

2.1.3 Symmetric and Positive Definite Tensors

Most tensors considered in this thesis have some kind of symmetry. We call a tensor T of order r on $\mathbb{R}^d$ *symmetric in the pth and qth variable* if

$$T(v_1, \dots, v_p, \dots, v_q, \dots, v_r) = T(v_1, \dots, v_q, \dots, v_p, \dots, v_r)$$

for all $v_1, \dots, v_r \in \mathbb{R}^d$. This is equivalent to the condition that the components of T are symmetric in the pth and qth index, i. e.

$$T_{i_1 \dots i_p \dots i_q \dots i_r} = T_{i_1 \dots i_q \dots i_p \dots i_r}$$

for all $i_1, \dots, i_r \in \{1, \dots, d\}$. A tensor is called *symmetric* if it is symmetric for each $p, q \in \{1, \dots, r\}$.

We are especially concerned with symmetric tensors of second order. By definition, such tensors satisfy $T(v,w) = T(w,v)$ for all $v, w \in \mathbb{R}^d$ or equivalently $T_{ij} = T_{ji}$ for all $i, j \in \{1, \dots, d\}$. Consequently, symmetric tensors of second order are represented by symmetric matrices, denoted by $\mathrm{Sym}(d)$. Note that all eigenvalues of a symmetric matrix are real, there are no complex eigenvalues. The stress tensor and the fiber orientation tensor discussed in Sections 2.4 and 2.5 are examples of such tensors.

A symmetric second order tensor T is called *positive definite* if

$$T(v,v) > 0$$

for all $v \in \mathbb{R}^d$ with $v \neq 0$. This implies that all eigenvalues of the corresponding matrix are positive. The fiber orientation tensor is an example of a positive definite tensor.

2.2 Tensor Fields

2.2.1 Definition and Basic Properties

In general, tensor fields are usually defined on arbitrary manifolds, see again [BG68] or [Boo86]. In this thesis we restrict ourselves to tensor fields defined on d-dimensional submanifolds $U \subset \mathbb{R}^d$, usually with boundary. A d-dimensional *tensor field* T of order r is a map

$$T \ : \ U \to \mathcal{T}_r(\mathbb{R}^d)$$

assigning a tensor of order r to each $p \in U$. All properties of tensors on $\mathbb{R}^d$ are defined pointwise for tensor fields. For instance, a tensor field is called symmetric or positive definite if $T(p)$ is a symmetric or positive definite tensor for all $p \in U$, respectively. As tensor fields are maps from a submanifold to the finite dimensional vector space $\mathcal{T}_r(\mathbb{R}^d)$, continuity and differentiability is also defined for tensor fields. A necessary and sufficient condition for continuity and differentiability is that this property holds componentwise, i. e. that

$$U \to \mathbb{R} \ , \quad p \mapsto T_{i_1 \dots i_r}(p) = T(p)(e_{i_1}, \dots, e_{i_r})$$

form continuous or differentiable functions for all $i_1, \dots, i_r \in \{1, \dots, d\}$.

In this thesis we are mostly concerned with symmetric tensor fields of second order. The tensor $T(p)$ at each $p \in U$ is usually interpreted as a symmetric matrix, thus we can consider a tensor field also as a map

$$T \ : \ U \to \mathrm{Sym}(d) \ .$$

In practice, tensor fields are usually given at discrete points, which form some kind of grid. The grid serves as discrete approximation of the submanifold U, i. e. U is partitioned into simple geometric objects, which are called cells or elements. The cells are mostly tetrahedrons or hexahedrons in the three-dimensional case, or triangles or quadrilaterals in the two-dimensional case. The tensors are commonly given at the vertices of the grid, in some cases the tensors are also defined for each cell. If the tensors are given at the vertices, then we obtain a continuous field by interpolating on the cells. In this work, linear interpolation is used on triangles or tetrahedrons, and bilinear or trilinear interpolation on quadrilaterals and hexahedrons, respectively.

An important application in this thesis are stress tensor fields, see Section 2.4. In this case U is usually the geometry of a technical component and the tensor field on U gives the stresses at each point of the component under a predefined load condition. The stress tensors are mostly computed by the finite element method (FEM), thus the tensors are given on the grid used for the FEM.

2.2.2 Gradients of Tensor Fields

Differentiation of a tensor field T of order r increases the order by one, so the gradient ∇T of T is a tensor field of order $r+1$. The components of $\nabla T(p)$ are given by

$$[\nabla T(p)]_{i_1 \dots i_r i_{r+1}} = \partial_{i_{r+1}} T_{i_1 \dots i_r}(p) \ ,$$

i. e. the components of $\nabla T(p)$ are the partial derivatives of the components of $T(p)$. According to Section 2.1.2 we can evaluate $\nabla T(p)$ with respect to the $(r+1)$th variable. In this way we interpret $\nabla T(p)$ also as a map

$$\nabla T(p) \ : \ \mathbb{R}^d \to \mathcal{T}_r(\mathbb{R}^d) \ , \quad v \mapsto [\nabla T(p)]_{i_1 \dots i_r i_{r+1}} v^{i_{r+1}} = [\nabla T(p)]v \ .$$

Now $[\nabla T(p)]v$ is nothing else than the directional derivative of T in direction v at the point p, which we also denote by $\nabla_v T(p)$. The gradient of symmetric tensor fields of second order is a tensor field of third order which is symmetric with respect to the first two variables, i. e. $[\nabla T(p)]_{ijk} = [\nabla T(p)]_{jik}$. Accordingly, $\nabla T(p)$ can be interpreted as a map

$$\nabla T(p) \ : \ \mathbb{R}^d \to \mathrm{Sym}(d) \ .$$

2.2.3 Degenerate Tensors

Tensor field topology subdivides the domain of a symmetric tensor field of second order into regions with similar behavior of the eigenvalues. Degenerate tensors form the central structure of tensor field topology, as they are the equivalent of singularities (zeros) of a vector field. A degenerate tensor is defined by the property that (at least) two eigenvalues are equal. Thus a two-dimensional tensor must satisfy

$$\lambda_1 = \lambda_2$$

and a three-dimensional tensor

$$\lambda_1 = \lambda_2 > \lambda_3 \quad \text{or} \quad \lambda_1 > \lambda_2 = \lambda_3 \quad \text{or} \quad \lambda_1 = \lambda_2 = \lambda_3 \ .$$

For a three-dimensional tensor the first two cases are referred to as double degeneracy, the third case as triple degeneracy. Moreover, a degenerate tensor is called planar if $\lambda_1 = \lambda_2 > \lambda_3$ and linear if $\lambda_1 > \lambda_2 = \lambda_3$. For a tensor field defined on $U \subset \mathbb{R}^d$, a point $p \in U$ is called a degenerate point if $T(p)$ is a degenerate tensor. In general, the degenerate points are isolated points for two-dimensional tensor fields, while the degenerate points form curves in three-dimensional tensor fields. A triple degeneracy of a three-dimensional tensor field is unstable, which means it vanishes under small perturbations of the field, see [ZP04] for details.

Double degeneracies of three-dimensional tensor fields are also determined by the value of the tensor mode, a scalar invariant which is also considered in Section 2.3.2. The tensor mode is equal to 1 or -1 if and only if the tensor is linear or planar, respectively. Since the mode is always in the interval $[-1, 1]$, the double degeneracies are extrema of the mode, see [TKW08]. Similarly, for two-dimensional tensor fields the degenerate points are minima of the invariants K_2 and R_2 discussed in Section 2.3.2, since the deviator $\tilde{T}$ is zero for degenerate T.

2.3 Invariants of Second Order Tensors

2.3.1 Definition and Basic Properties

In general, a scalar valued function depending on the components of a tensor is called *invariant* if it does not alter its value under a change of the coordinate system, cf. [BG68, Section 2.14.]. In this thesis, we are concerned with invariants of second order tensors which are interpreted as matrices $T \in \mathbb{R}^{d,d}$. Then an invariant function f depending on T must satisfy

$$f(T) = f(B^{-1}TB)$$

for each change of basis matrix $B \in \mathbb{R}^{d,d}$, cf. equation (2.3) and the remarks in the end of Section 2.1.2. An example for such invariants are the eigenvalues of T. If v is an eigenvector of T with corresponding eigenvalue λ, that is $Tv = \lambda v$, then λ is an eigenvalue of $B^{-1}TB$ with corresponding eigenvector $B^{-1}v$ since

$$(B^{-1}TB)B^{-1}v = B^{-1}Tv = \lambda(B^{-1}v) \ .$$

Consequently, each function depending on the eigenvalues of T is again an invariant of T.

There are different definitions whether the transformation B can be any invertible transformation, in this case B is an element of the general linear group $\mathrm{GL}(d)$. Or if B must be orthogonal, i. e. B is an element of the orthogonal group $\mathrm{O}(d)$, cf. [KEWW07]. A quantity which is invariant with respect to transformations $B \in \mathrm{GL}(d)$ is also invariant with respect to transformations $B \in \mathrm{O}(d)$, since $\mathrm{O}(d) \subset \mathrm{GL}(d)$. But an invariant with respect to $\mathrm{O}(d)$ is not necessarily an invariant with respect to $\mathrm{GL}(d)$. For example, easy computations show that the Frobenius norm is invariant with respect to $\mathrm{O}(d)$, but not invariant with respect to $\mathrm{GL}(d)$.

Here we restrict ourselves to symmetric tensors $\mathrm{Sym}(d)$ and invariants with respect to $\mathrm{O}(d)$, i. e. changes between different orthonormal systems. In this case there exist a transformation $B \in \mathrm{O}(d)$ and a diagonal matrix D with

$$BDB^{\top} = T \ .$$

The diagonal entries of D are the eigenvalues $\lambda_1, \ldots, \lambda_d$ of T and the columns of B the corresponding eigenvectors. As a consequence, the invariant part of a symmetric tensor T is defined by the eigenvalues, thus each invariant with respect to $\mathrm{O}(d)$ can be written as a function depending on the eigenvalues.

Similarly to Kindlmann et al. [KEWW07], we can also consider a tensor invariant as a function f which is constant on the orbits of the group action of $\mathrm{O}(d)$ on $\mathrm{Sym}(d)$. The group action is given by

$$\begin{aligned} \phi \ : \ \mathrm{O}(d) \times \mathrm{Sym}(d) &\to \mathrm{Sym}(d) \ , \\ (B, T) &\mapsto BTB^\top \ , \end{aligned}$$

and the respective orbit of a tensor $T \in \mathrm{Sym}(d)$ is given by

$$\left\{ BTB^\top \ : \ B \in \mathrm{O}(d) \right\} \ .$$

The requirement that f is constant on these orbits is equivalent to the definition of invariants above. Now the orbits represent all possible orientations of a tensor, which are given by the eigenvectors. Since an invariant function is constant on the orbits, its gradient is orthogonal to the orbits of ϕ. This gives a mathematical justification that changes of the invariants and the eigenvectors of a tensor are considered orthogonal to each other.

2.3.2 Sets of Invariants

In the following, we will discuss four common sets of invariants for two- and three-dimensional symmetric second order tensors and give its representation with respect to the eigenvalues. The eigenvalues of symmetric second order tensors are real-valued and we assume the eigenvalues to be sorted in descending order $\lambda_1 \geq \cdots \geq \lambda_d$. For brevity, we denote the deviator of T by

$$\tilde{T} = T - \left(\frac{1}{d} \operatorname{tr} T \right) E \ ,$$

where $\operatorname{tr} T$ denotes the trace of T and E is the identity matrix. We denote the eigenvalues of $\tilde{T}$ by $\tilde{\lambda}_1, \ldots \tilde{\lambda}_d$, which are given in terms of the eigenvalues of T by

$$\tilde{\lambda}_i = \lambda_i - \frac{1}{d} \sum_j \lambda_j \ .$$

Eigenvalues λ

As shown above, the eigenvalues of T are invariants and the invariant part of a tensor is completely described by the eigenvalues. Thus the eigenvalues $\lambda_1, \ldots, \lambda_d$ itself serve as a set of invariants.

Principal invariants I

The principal invariants $I_1, \ldots, I_d$ are the coefficients of the characteristic polynomial. They are given by

$$\begin{aligned} I_1 &= \operatorname{tr} T = \lambda_1 + \lambda_2 \ , \\ I_2 &= \det T = \lambda_1 \lambda_2 \end{aligned}$$

for two-dimensional tensors and by

$$\begin{aligned} I_1 &= \operatorname{tr} T = \lambda_1 + \lambda_2 + \lambda_3 \ , \\ I_2 &= T_{11}T_{22} + T_{22}T_{33} + T_{11}T_{33} - T_{12}T_{21} - T_{23}T_{32} - T_{13}T_{31} \\ &= \lambda_1\lambda_2 + \lambda_2\lambda_3 + \lambda_3\lambda_1 \ , \\ I_3 &= \det T = \lambda_1\lambda_2\lambda_3 \end{aligned}$$

for three-dimensional tensors, where $\operatorname{tr} T$ denotes the trace and $\det T$ the determinant of T. There is obviously a one-to-one correspondence between the principal invariants I and the eigenvalues λ, since the eigenvalues are the roots of the characteristic polynomial.

Invariants K

Another well-known set of invariants for three-dimensional tensors consists of the trace, the Frobenius norm $\|\cdot\|_F$ of the deviator, and the mode-of-distortion of the tensor. It was first introduced by Criscione et al. in [CHDH00] and is also studied in [EK06] and [KEWW07]. Usually the letter K is used for these invariants and they are given by

$$\begin{aligned} K_1 &= \operatorname{tr} T = \lambda_1 + \lambda_2 + \lambda_3 \ , \\ K_2 &= \|\tilde{T}\|_F = \sqrt{\tilde{\lambda}_1^2 + \tilde{\lambda}_2^2 + \tilde{\lambda}_3^2} \ , \\ K_3 &= 3\sqrt{6} \det \left(\frac{\tilde{T}}{\|\tilde{T}\|_F} \right) = 3\sqrt{6} \frac{\tilde{\lambda}_1 \tilde{\lambda}_2 \tilde{\lambda}_3}{(\tilde{\lambda}_1^2 + \tilde{\lambda}_2^2 + \tilde{\lambda}_3^2)^{\frac{3}{2}}} \ . \end{aligned}$$

The mode-of-distortion K_3 is sometimes simply called mode, as we do in the remainder of this work. Assuming the eigenvalues to be sorted $\lambda_1 \geq \lambda_2 \geq \lambda_3$, there is a one-to-one correspondence between the K-invariants and the eigenvalues for $K_2 \neq 0$. For $K_2 = 0$ the mode K_3 is undefined. Another nice property of these invariants is that they are orthogonal. Considering the K_i as functions depending on the tensor components, its gradients ∇K_i are mutually orthogonal, see the appendix of [EK06] for details.

These invariants have an important meaning for several applications. In the context of diffusion tensor imaging, the trace is a measure of diffusivity, while $\|\tilde{T}\|$ serves as a measure of anisotropy. For stress tensors (cf. Section 2.4) the trace is proportional to the mean stress $1/3 \operatorname{tr} T$. The norm of the deviator is proportional to the von Mises stress

$$\sigma_v = \sqrt{\frac{3}{2}} \|\tilde{T}\|_F = \sqrt{\frac{3}{2}} K_2 \ ,$$

a widely-used criterion of failure in material science, see Section 2.4.2. The tensor mode K_3 can be used to characterize the type of anisotropy. A mode close to 1 or -1 means that the two lower eigenvalues λ_2 and λ_3 or the larger eigenvalues λ_1 and λ_2 are close to each other, respectively. Consequently, for a stress tensor a mode of 1 indicates a tension in one direction or a compression in two directions. Similarly, a mode of -1 implies a compression in one direction or a tension in two directions.

By simply omitting K_3 we can use these invariants also for two-dimensional tensors, i. e. we consider the invariants

$$\begin{aligned} K_1 &= \operatorname{tr} T = \lambda_1 + \lambda_2 \ , \\ K_2 &= \|\tilde{T}\|_F = \sqrt{\tilde{\lambda}_1^2 + \tilde{\lambda}_2^2} = \sqrt{\frac{1}{2}} |\lambda_1 - \lambda_2| \ . \end{aligned}$$

These invariants have similar properties in the two-dimensional case. Simple computations show that there is also a one-to-one correspondence between K_1, K_2 and the (sorted) eigenvalues of T, and that these invariants are also orthogonal.

Invariants R

Another set of invariants for three-dimensional tensors consists of the Frobenius norm, the fractional anisotropy FA and the mode of the tensor, it is also discussed in [EK06] and [KEWW07]. These R-invariants are given by

$$\begin{aligned} R_1 &= \|T\|_F = \sqrt{\lambda_1^2 + \lambda_2^2 + \lambda_3^2} \ , \\ R_2 &= \mathrm{FA}(T) = \sqrt{\frac{3}{2}} \frac{\|\tilde{T}\|_F}{\|T\|_F} = \sqrt{\frac{3}{2}} \frac{\sqrt{\tilde{\lambda}_1^2 + \tilde{\lambda}_2^2 + \tilde{\lambda}_3^2}}{\sqrt{\lambda_1^2 + \lambda_2^2 + \lambda_3^2}} \ , \\ R_3 &= K_3 \ . \end{aligned}$$

Like the K-invariants, these invariants are also orthogonal, i. e. they have orthogonal gradients, see again [EK06] for details. In contrast to the sets of invariants discussed before, there is no one-to-one correspondence between the R-invariants and the eigenvalues of T. An easy computation shows that for each tensor T the tensor

$$\hat{T} = T - \left(\frac{2}{3}\operatorname{tr} T\right) E$$

has the same Frobenius norm and the same deviator as T. Consequently, all R-invariants of T and $\hat{T}$ are the same, while the eigenvalues are different. However, for positive definite tensors there is again a one-to-one correspondence between the R-invariants and the eigenvalues. For a positive definite tensor T, the tensor $\hat{T}$ must have a negative eigenvalue, thus $\hat{T}$ is not positive definite.

The R-invariants also play an important role in diffusion tensor imaging. Like the trace, the Frobenius norm is also used as a measure of diffusivity. The fractional anisotropy is a widely-used measure of anisotropy ranging between 0 and 1. It is equal to 0 for a uniform tensor, i. e. a multiple of the identity matrix, and it is equal to 1 for a traceless tensor.

Again, we can apply the definitions of R_1 and R_2 also on two-dimensional tensors. This yields

$$\begin{aligned} R_1 &= \|T\|_F = \sqrt{\lambda_1^2 + \lambda_2^2} \ , \\ R_2 &= \operatorname{FA}(T) = \sqrt{2}\frac{\|\tilde{T}\|_F}{\|T\|_F} = \sqrt{2}\frac{\sqrt{\tilde{\lambda}_1^2 + \tilde{\lambda}_2^2}}{\sqrt{\lambda_1^2 + \lambda_2^2}} = \sqrt{\frac{(\lambda_1 - \lambda_2)^2}{\lambda_1^2 + \lambda_2^2}} \ , \end{aligned}$$

which serves as a set of invariants for two-dimensional tensors with similar properties as in the three-dimensional case.

Other Sets of Invariants

In this work, we make only use of the four sets of invariants just discussed. Of course there are other common sets of invariants, two of them are to be mentioned here. The first one consists of the invariants I_1, J_2, J_3, where

$$\begin{aligned} J_2 &= -(\tilde{\lambda}_1\tilde{\lambda}_2 + \tilde{\lambda}_2\tilde{\lambda}_3 + \tilde{\lambda}_3\tilde{\lambda}_1) = \frac{1}{2}\|\tilde{T}\|^2 = \frac{1}{2}K_2^2 \ , \\ J_3 &= \tilde{\lambda}_1\tilde{\lambda}_2\tilde{\lambda}_3 = \det \tilde{T} \ , \end{aligned}$$

i. e. J_2 is the negative of the second principal invariant of the deviator and J_3 the third principal invariant of the deviator. Consequently, these invariants are similar to the K-invariants. They are frequently used to study stress tensors, see for example [GZZ$^+$11]. Another prevalent set of invariants is given by

$$\operatorname{tr}(T) \ , \quad \operatorname{tr}\left(T^2\right) \ , \quad \operatorname{tr}\left(T^3\right) \ ,$$

see for exmaple [SN09].

2.4 Stress Tensor

2.4.1 Definition and Basic Properties

The question whether a material can resist a certain load depends on the stresses arising inside the material. To answer this question we need to know about the stresses at each point of the component. The complete state of stress is given as a three-dimensional symmetric tensor field of second order, the *Cauchy stress tensor*. There are other kinds of stress tensors, but in this work only the Cauchy stress tensor will be used. For the sake of brevity it will usually be referred to simply as *stress tensor*. It is usually given by a matrix

$$\sigma = \begin{bmatrix} \sigma_x & \tau_{xy} & \tau_{xz} \\ \tau_{xy} & \sigma_y & \tau_{yz} \\ \tau_{xz} & \tau_{yz} & \sigma_z \end{bmatrix}$$

where σ and τ denote the normal and shear stresses, respectively. The subscripts x, y, z refer to the axes of an cartesian coordinate system defined by an orthonormal basis $\{e_1,\ e_2,\ e_3\}$. The stress tensor σ is usually interpreted in terms of the stress vector. Given a unit normal vector n, the *stress vector* σn describes the forces acting on a plane perpendicular to n. The projection of the stress vector σn on the normal n is called the *normal stress*, the projection on the plane perpendicular to n is called the *shear stress*. Consequently, the components σ_x, σ_y, σ_z are the normal stresses in the coordinate directions, the components τ_{xy}, τ_{xz}, τ_{yz} define the shear stresses in the planes perpendicular to the coordinate directions. Due to the symmetry of σ there is a orthonormal basis of eigenvectors of σ. The eigenvectors, denoted by n_1, n_2, n_3, are called *principal directions*. The corresponding eigenvalues are called *principal stresses* and commonly denoted by $\sigma_1, \sigma_2, \sigma_3$, not to be confused with the normal stresses $\sigma_x, \sigma_y, \sigma_z$ in an arbitrary coordinate system. The shear stresses vanish on the planes perpendicular to the eigenvectors n_1, n_2, n_3, there are only normal stresses. Positive eigenvalues indicate tensile stresses, negative values compressive stresses.

Stress vectors are often used to depict the stress tensor. Given an orthonormal coordinate system e_1, e_2, e_3, the stress tensor σ is completely described by the three stress vectors $\sigma e_1, \sigma e_2, \sigma e_3$. The three planes perpendicular to e_1, e_2, e_3 define the

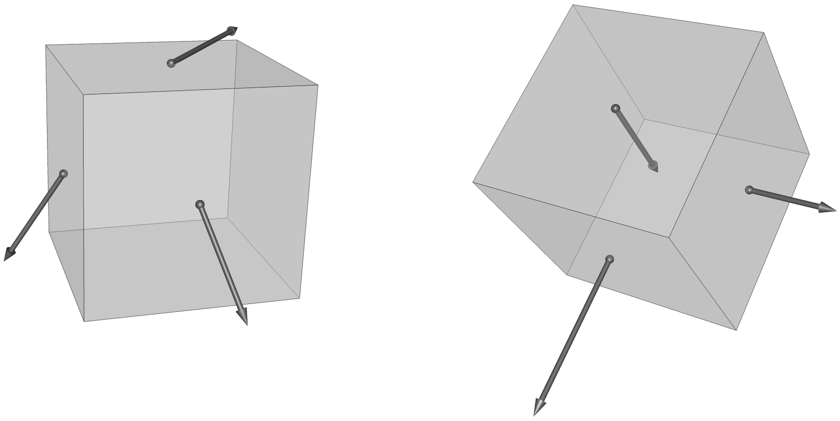

Figure 2.1: *Widely-used illustration of the stress tensor. The arrows depict stress vectors, that is the force acting on the planes given by the sides of the cube. For the right image the cube is oriented according to the principle stress directions, thus there is only normal stress and the stress vectors are perpendicular to the sides of the cube. An outward pointing arrow represents tension, an inward pointing arrow represents compression.*

sides of a cube, which is shown together with the three stress vectors, see Figure 2.1 left. If the eigenvectors of σ are used as coordinate system, the three stress vectors are perpendicular to the sides of the cube, see Figure 2.1 right. Similar illustrations of the stress tensor are used in many textbooks of solid mechanics, see for example [Hol00].

2.4.2 Yield Criteria

Yield criteria are used to predict if a material can resist a local stressing condition. In this section we discuss three yield criteria which are computed from the components of the stress tensor. We start with the von Mises stress, which is a common choice for predicting failure of isotropic materials. For anisotropic materials, e. g. the short fiber reinforced polymers studied in Chaper 3, more intricate criteria like the Tsai-Hill and the Tsai-Wu criterion are necessary. The latter is even more complex, since it incorporates a different tensile and compressive strength, which are assumed to be equal in the Tsai-Hill criterion.

Von Mises criterion

One widely used failure criterion is the von Mises stress [vM13] given by

$$\begin{aligned}\sigma_v &= \sqrt{\frac{(\sigma_y - \sigma_z)^2 + (\sigma_x - \sigma_z)^2 + (\sigma_x - \sigma_y)^2 - 6(\tau_{xy}^2 + \tau_{xz}^2 + \tau_{yz}^2)}{2}} \\ &= \sqrt{\frac{(\sigma_2 - \sigma_3)^2 + (\sigma_1 - \sigma_3)^2 + (\sigma_1 - \sigma_2)^2}{2}} = \sqrt{\frac{3}{2}} \|\tilde{\sigma}\|_F \ . \qquad (2.4)\end{aligned}$$

The material is assumed to fail if σ_v exceeds a certain threshold which has to be determined experimentally. This criterion is only meaningful for isotropic materials, i. e. it is independent of the orientation of the material with respect to the stress.

Tsai-Hill Criterion

A more advanced criterion is the Tsai-Hill criterion [Hil50] which is given by

$$F(\sigma_y - \sigma_z)^2 + G(\sigma_x - \sigma_z)^2 + H(\sigma_x - \sigma_y)^2 + 2(L\tau_{xy}^2 + M\tau_{xz}^2 + N\tau_{yz}^2) \leq 1 \ , \qquad (2.5)$$

while the constants F, G, H, L, M, N are given by

$$F = \frac{1}{2}\left(\frac{1}{Y^2} + \frac{1}{Z^2} - \frac{1}{X^2}\right) \ , \quad G = \frac{1}{2}\left(\frac{1}{X^2} + \frac{1}{Z^2} - \frac{1}{Y^2}\right) \ ,$$

$$H = \frac{1}{2}\left(\frac{1}{X^2} + \frac{1}{Y^2} - \frac{1}{Z^2}\right) \ ,$$

$$L = \frac{1}{2S_{xy}^2} \ , \quad M = \frac{1}{2S_{xz}^2} \ , \quad N = \frac{1}{2S_{yz}^2} \ .$$

The numbers X, Y, Z denote the failure strength in x-, y- and z-direction, there is no differentiation between compression and tension. S_{xy}, S_{xz}, S_{yz} denote the shear strength in the x-y-, x-z-, y-z-plane, respectively. These values have to be determined by tensile and shear testing, see Figure 2.2.

Because there are six material constants in the model, six experiments are necessary for calibration. For isotropic materials this criterion reduces to the von Mises stress. In case of transversal isotropy the number of experiments reduces to three. Transversal isotropy means that the material does not change its properties with arbitrary rotations around a particular axis. A fiber reinforced polymer with a unidirectional fiber distribution, that is all fibers are pointing in the same direction, fulfills this property. Here, the axis of symmetry is given by the direction of the fibers. If we choose a coordinate system where the x-axis coincides with the axis of symmetry, we have $Y = Z$ and $S_{xy} = S_{xz}$. Additionally the rotational symmetry implies $N = 2F + G$ which replaces S_{yz}. Consequently, we need experimentally determined values for X, Y, S_{xy}.

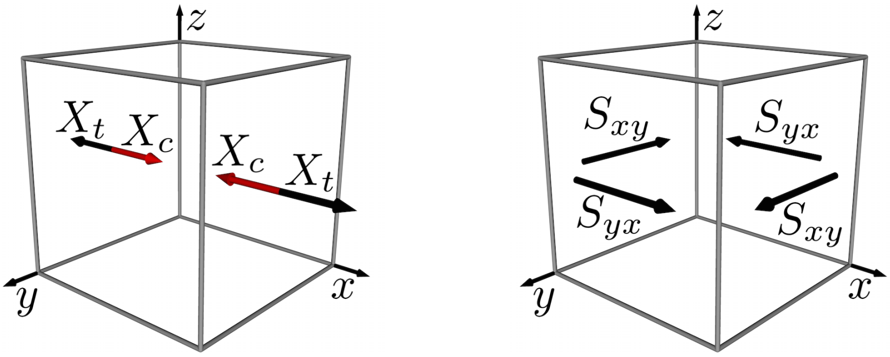

Figure 2.2: *Illustration of tensile and compressive testing in x direction (left) and shear testing in the x-y-plane (right). Testing S_{xy} or S_{yx} yields the same result.*

Tsai-Wu Criterion

The Tsai-Hill criterion does not distinguish between tensile and compressive stresses. A criterion incorporating this is the Tsai-Wu failure criterion [TW71] given by

$$\begin{aligned} & b_1\sigma_x + b_2\sigma_y + b_3\sigma_z + F_{11}\sigma_x^2 + F_{22}\sigma_y^2 + F_{33}\sigma_z^2 \\ + & 2F_{12}\sigma_x\sigma_y + 2F_{13}\sigma_x\sigma_z + 2F_{23}\sigma_y\sigma_z + F_{44}\tau_{xy}^2 + F_{55}\tau_{xz}^2 + F_{66}\tau_{yz}^2 \leq 1 \ . \end{aligned} \tag{2.6}$$

The b_i and F_{ij} are given by

$$b_1 = \frac{1}{X_t} - \frac{1}{X_c} \ , \quad b_2 = \frac{1}{Y_t} - \frac{1}{Y_c} \ , \quad b_3 = \frac{1}{Z_t} - \frac{1}{Z_c} \ ,$$

$$F_{11} = \frac{1}{X_tX_c} \ , \quad F_{22} = \frac{1}{Y_tY_c} \ , \quad F_{33} = \frac{1}{Z_tZ_c} \ ,$$

$$F_{44} = \frac{1}{S_{xy}^2} \ , \quad F_{55} = \frac{1}{S_{xz}^2} \ , \quad F_{66} = \frac{1}{S_{yz}^2} \ ,$$

$$F_{12} = -\frac{1}{2\sqrt{X_tX_cY_tY_c}} \ , \quad F_{13} = -\frac{1}{2\sqrt{X_tX_cZ_tZ_c}} \ ,$$

$$F_{23} = -\frac{1}{2\sqrt{Y_tY_cZ_tZ_c}} \ .$$

Here the indices t and c for X, Y, Z indicate tension or compression. In general, there are three more experiments necessary to calibrate this criterion, i. e. a total of nine experiments. In case of transversal isotropy the number of experiments reduces again, we obtain $b_2 = b_3$, $F_{22} = F_{33}$, $F_{44} = F_{55}$, $F_{12} = F_{13}$ and by rotational symmetry also $F_{66} = 3F_{22}$. Consequently, we need experimentally determined values $X_t, X_c, Y_c, Y_t, S_{xy}$, so there are only five experiments necessary.

2.5 Fiber Orientation Tensors and Fiber Distribution Functions

2.5.1 Definition and Basic Properties

In Chapter 3 we analyze the stability of technical components made of short fiber reinforced polymers by injection molding. The orientation of the fibers, which are enclosed by the polymer, is influenced by the injection process and differs for varying locations of the component. In contrast to homogeneous materials, it is much more difficult to decide if such a material can resist local stressing conditions. The orientation of the fibers influences the stability, thus the admissible stresses are different at varying locations of the material. At each point of the component the fiber orientation is given by a probability density function ψ defined on the unit sphere $\mathbb{S}^2$. The function ψ is also called the *fiber distribution function.* It specifies the probability that a fiber points in a certain direction. Alternatively, it can be seen as the distribution of fiber orientations in a small neighborhood.

The *(second order) fiber orientation tensor* a_{ij} is a three-dimensional tensor approximating the fiber distribution function ψ. The relation between ψ and a_{ij} is given by

$$a_{ij} = \int_{\mathbb{S}^2} v_i v_j \psi(v)\, dv \quad , \tag{2.7}$$

where $v = (v_1, v_2, v_3) \in \mathbb{S}^2$ is a point on the unit sphere, i.e. $\|v\| = 1$. From the properties of the probability distribution follows that a_{ij} is a symmetric positive definite tensor of second order with $\operatorname{trace}(a_{ij}) = 1$. While a_{ij} gives a rough approximation of the fiber distribution function ψ, a more precise approximation of ψ can be obtained if we also know the *fourth order fiber orientation tensor* a_{ijkl} which is defined similarly by

$$a_{ijkl} = \int_{\mathbb{S}^2} v_i v_j v_k v_l \psi(v)\, dv \quad .$$

2.5.2 Reconstruction of the Fiber Distribution Function

Simulations of the injection molding process are used in Chapter 3 in order to obtain information on the orientation of the fibers. The fiber orientations computed during the simulation process are outputted as second order fiber orientation tensors. In some cases, we are interested in the fiber distribution function rather than the fiber orientation tensor. A fiber distribution function can be approximately reconstructed from a given fiber orientation tensor. One such reconstruction, which is widely used in the context of short fiber composites, is briefly discussed in this section, for details we refer the reader to [JS04] and the references therein.

The fiber distribution function ψ can be expressed by the series expansion

$$\psi(v) = f_0 V_0 + f_{ij}(v) V_{ij} + f_{ijkl}(v) V_{ijkl} + \dots \ .$$

The basis functions f_0, f_{ij}, f_{ijkl}, $\dots$ as well as the coefficients V_0, V_{ij}, V_{ijkl}, $\dots$ have values in the space of tensors of order zero, two, four and so on. Note that the Einstein summation convention is used here for each term, i. e.

$$f_{ij}(v) V_{ij} = \sum_{i=1}^{3} \sum_{j=1}^{3} f_{ij}(v) V_{ij} \ .$$

Truncation after the fourth order term yields a fourth order reconstruction of the fiber distribution function. The basis functions up to order four are given by

$$\begin{aligned} f_0 &= 1 \\ f_{ij} &= v_i v_j - \frac{1}{3}\delta_{ij} \\ f_{ijkl} &= v_i v_j v_k v_l \\ &\quad - \frac{1}{7}(v_i v_j \delta_{kl} + v_i v_k \delta_{jl} + v_i v_l \delta_{jk} + v_j v_k \delta_{il} + v_j v_l \delta_{ik} + v_k v_l \delta_{ij}) \\ &\quad + \frac{1}{35}\left(\delta_{ij}\delta_{kl} + \delta_{ik}\delta_{jl} + \delta_{il}\delta_{jk}\right) \end{aligned}$$

where δ_{ij} denotes the Kronecker delta. The coefficients can be computed from the basis functions by

$$V_{i_1 \dots i_N} = \frac{1}{4\pi N!} \prod_{x=0}^{N} (2x+1) \int_{\mathbb{S}^2} \psi(v) f_{i_1 \dots i_N} \, dv \ . \tag{2.8}$$

For V_{ij} the integral in equation (2.8) can be rewritten to

$$\int_{\mathbb{S}^2} \psi(v) f_{ij} \, dv = a_{ij} - \frac{1}{3}\delta_{ij} \ ,$$

by $\int_{\mathbb{S}^2} \psi(v) \, dv = 1$ and the definition of the fiber orientation tensor (2.7). Consequently it is easy to compute V_{ij} for a given fiber orientation tensor. The computation of V_{ijkl} is more difficult, since the integral becomes

$$\int_{\mathbb{S}^2} \psi(v) f_{ijkl}\, dv = \int_{\mathbb{S}^2} \psi(v) v_i v_j v_k v_l\, dv - \ldots = a_{ijkl} - \ldots \quad ,$$

i. e. the fourth order fiber orientation tensor a_{ijkl} is involved here. Since a_{ijkl} is not an output of the injection molding simulation, it is a common practice to approximate it from the second order fiber orientation tensor a_{ij}.

Several so-called closure approximations have been proposed to approximate a_{ijkl}, see for example [CJTI95] and [DT06]. One of the simplest closure approximations is the quadratic closure which is given by

$$a_{ijkl} = a_{ij} a_{kl} \quad .$$

The linear closure is defined by

$$\begin{aligned} a_{ijkl} = &-\frac{1}{7}(a_{ij}\delta_{kl} + a_{ik}\delta_{jl} + a_{il}\delta_{jk} + a_{jk}\delta_{il} + a_{jl}\delta_{ik} + a_{kl}\delta_{ij}) \\ &+ \frac{1}{35}\left(\delta_{ij}\delta_{kl} + \delta_{ik}\delta_{jl} + \delta_{il}\delta_{jk}\right) \quad . \end{aligned}$$

While the quadratic closure is exact for unidirectional fiber orientations, the linear closure is exact for uniform (random) fiber orientations. In Chapter 3 we use the so-called hybrid closure approximation, which is basically a combination of the quadratic and the linear closure. For details, we refer the reader to [DT06].

3

Feature-Based Tensor Field Visualization for Fiber Reinforced Polymers

The design of components is a central task in mechanical engineering. Nearly all modern products consist of several components that were subject to an engineering design process. Of course, aesthetics and usability play often an important role. Also, many components have to resist one or several predefined mechanical load conditions. Besides these constraints, the engineer tries to minimize an overall cost function, which often includes production cost, production speed and component weight. Essentially, the engineer has to optimize the component design under a number of constraints. Besides the geometry, he has to select a material and to define the production process. Eventually, an engineer has a rather strict time budget to carry out the task.

In this chapter, we consider a specific, but frequent case of engineering design. We assume that the design aims at a component with a predefined static load condition. Furthermore, we assume that weight and production cost play a major role. Therefore, a lightweight composite material, specifically a short fiber reinforced polymer, is selected which allows for cheap mass production using injection molding. There is a very large number of different components with these specifications on the market at the moment, and this number is increasing rapidly. Many mechanical engineers carry out this task every day. Consequently, there is a strong interest in computational methods that support this design process.

One important step during the design process is a virtual test of the design with respect to the load condition. A structural mechanics simulation using the finite element method (FEM) is the standard choice for this task. The system computes the stress and strain tensor field together with other field information. From there, the engineer tries to answer his major questions:

1. Does the current design fulfill the load condition?
2. If the design fails the virtual test, where does it fail?

To get answers to these questions, the engineer reduces the tensor field information usually to a scalar field using a yield criterion. By thresholds defining the strength of the material the field is further reduced to a boolean field, cf. Section 2.4.2. The development of yield criteria for short fiber reinforced polymers is still in its infancy, so criteria for homogeneous materials like the von Mises criterion (2.4) are often used despite their serious limitations in this context. The more involved yield criteria like the Tsai-Hill (2.5) or the Tsai-Wu (2.6) criterion use anisotropic material properties in their evaluation. To obtain the anisotropic, inhomogeneous material properties, the injection molding process is simulated. This results in a fiber orientation tensor (2.7) for every finite element, which defines the local material properties. The material properties can be incorporated in the Tsai-Hill and Tsai-Wu criterion by the constants given in equation (2.5) and (2.6). However, it is very difficult to find these constants for arbitrary fiber orientations.

Moreover, all these criteria are used to reduce the whole field information to a simple boolean field that says if the material fails at a certain position. The resulting visualization is rather simple and has two variants. First, the boolean criterion is shown directly. Second, since these criteria define a scalar field, the scalar field may be shown, usually by color coding or isosurfaces. From an engineer's point of view, there are actually additional questions. If the component fails the virtual test, he needs to improve the design. A typical question is:

3. Can the material properties be changed (by changing the injection molding process) to pass the test with the current geometric design?

Depending on the answer of question 3 the engineer might further ask:

4. If the geometric design has to be changed, how should it be changed?
5. If the component copes with the load condition, can the costs be reduced without violating the constraints?

Regarding questions 4 and 5 see another recent article by Kratz et al. [KSZ$^+$14]. In this chapter we focus on question 3. Current systems do not give visual support regarding this question. The goal is to demonstrate that additional analysis and visualization allow to derive more helpful information from the data than just a boolean or scalar field.

From a visualization researcher's point of view, we have clearly stated questions to derive a suitable visualization solution. Therefore, a feature-based approach is proposed, which allows to focus the engineer's attention to the critical regions and present detail information on the problems or chances of the current design on demand. As two tensor fields, the stress tensor and the fiber orientation tensor, are at the center of the idea, it is called a feature-based tensor field visualization for fiber reinforced polymers.

A feature is defined as "data that are important or relevant in some respect (features)" [PPVWS95, sec. 3] in the visualization literature. In our case, with respect to question 3, we distinguish three cases:

(R) Red feature: it is a region of the component where a change of the local fiber distribution will not allow to pass the test. Such a feature in the component forces the engineer to change the geometric design.

(O) Orange feature: This is a region in the component where the current fiber orientation fails under the local stress condition. However, a change in the fiber orientation may lead to a positive test. The engineer may try to change the injection molding process to get a valid design without geometric changes that usually require more material and increase production cost.

(Y) Yellow feature: This is a region where the current fiber orientation sustains the local stress, but a change in fiber orientation may lead to failure. If the engineer wants to remove an orange feature, he has to keep the yellow features in mind.

The remaining case is called "green": These are regions where any fiber orientation allows to cope with the local stress.

The visualization proposed in this chapter tries to concentrate on the engineer's questions. As an initial overview, graphs are shown which give the number of red, orange and yellow elements for the single time steps of the simulation. A time step in the simulation reflects a certain load. This helps the engineer to select a load where the stress becomes critical. Now a time step can be selected from the graph interactively and the most critical features in the data are presented. If there are red features, only these are shown. The engineer knows now that his geometric design should undergo a change. If there are orange features but no red features, only the orange features are shown. The engineer knows that his current design fails, but he may try to change the injection molding process to solve the problem. If there are neither red nor orange regions, the yellow regions are shown and the engineer knows that the fibers improve the stability of the component. If there are neither red, orange nor yellow features, then the engineer knows that the component is stable enough for any fiber orientation. In the last case, he might consider to use the plain polymer without reinforcement. A further reduction of material volume using a different geometric design is another option.

In a second step, detail information on the local situation in the orange and yellow regions is given. A glyph is used to indicate the current local fiber distribution and a double cone to illustrate the suitable fiber directions for the current stress. This allows the engineer to get an idea on how the fiber direction needs to be changed in the orange regions and which changes have to be avoided in the yellow regions. Of course, this is far from solving the question of how to change the injection molding, but it is very valuable information that other approaches miss.

3.1 Application

The example considered in this chapter and the simulated data were provided by our cooperation partners Prof. Dr. Markus Stommel and Michael Stanko from the Chair for Plastics Technology at TU Dortmund University. A metal triangular wrench has to be replaced by a lightweight version, see Figure 3.1. The design of the wrench has to fulfill certain constraints. As the wrench has to fit to the intended nut, a part of the geometry is predefined. In addition, the use by a human hand determines part of the surface geometry. This resulted in a CAD model, see Figure 3.2. To reduce the weight a short fiber reinforced polymer is selected as material, specifically, PBT (polybutylene terephthalate) reinforced by 20% short glass fibers. This material allows to use injection molding for cheap mass production.

The next step was a virtual test using the commercial FEM software package ABAQUS (Dassault Systèmes Simulia Corp., Providence, RI, USA). An anisotropic elasto-plastic material model is assumed. The dimensions of the component are 148x56x44 mm and the mesh resolution is 1 mm edge length of the finite elements. This results in a medium sized mesh of approximately 170,000 elements. The used finite elements are 10-node second-order quadratic tetrahedra, which enable a detailed geometrical representation and provide accurate simulation results.

While the previous work [KSZ$^+$14] aimed at optimizing the geometric design using tensor visualization methods, this chapter focusses on visualizations that lead to an improvement of the injection molding process. Therefore, the injection process needs to be simulated. The commercial tool MOLDFLOW (Moldflow Corporation Framingham, MA, USA) was used by our cooperation partners for this purpose. The resulting field is mapped to the ABAQUS mesh using the tool CONVERSE (Simcon GmbH, 52146 Würselen, Germany). This defines a fiber orientation tensor for each element. From this field, an inhomogeneous and anisotropic mechanical behavior can be derived, which is the basis of the visualization effort in this chapter.

Figure 3.1: *Original metal version of the triangular wrench*

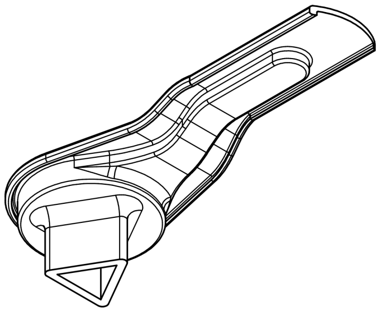

Figure 3.2: *Full CAD model of new plastic design*

3.2 Method

With the method proposed in this chapter we want to find out whether a component can be improved by a modified fiber orientation, and if so, we are interested in possible improvements of the fiber orientation. To do this we have to be able to predict potential failure in dependence of a fiber orientation. This allows us to distinguish four simple cases: The material fails in case of any fiber orientation (red), the material never fails (green), or it depends on the fiber orientation. The latter case also considers whether the actual fiber orientation fails (orange) or not (yellow). Using glyphs visualizing admissible fiber directions alongside the given fiber orientation, possible improvements of the fiber orientation are shown. Since common tensor glyphs are not directly usable for visualizing fiber orientation tensors, an adapted version of superquadrics is proposed.

3.2.1 Predicting Failure

Short fiber reinforced polymers produced by injection molding are inhomogeneous materials, i. e. the fiber distribution varies from point to point. Thus, in each point, the constants of a yield criterion like the Tsai-Hill criterion (2.5) or the Tsai-Wu criterion (2.6) have to be defined differently. It would be necessary to perform tensile and shear testing for every possible fiber distribution. This would not only be a big effort, it would also be necessary to produce specimen with specific fiber orientations, which is not possible. Only the production of specimen with (nearly) unidirectional fiber orientations is feasible, i. e. only in case of unidirectional fiber orientations failure can be predicted precisely. In order to estimate failure for an arbitrary fiber orientation, the following heuristic is proposed. In a first step we assume different unidirectional fiber orientations and compute whether the material would fail under the given stress. In a second step, the fiber distribution function is employed to compute the percentage of fibers pointing in failing directions. If this value exceeds a predefined threshold, then the material is assumed to fail.

For the first step we need to apply the Tsai-Hill (2.5) or the Tsai-Wu criterion (2.6) on unidirectional fiber orientations. Unidirectional fiber orientations result in a transversal isotropic material, and we assume that the constants in equation (2.5) or (2.6) are chosen for fibers pointing in x-direction. Instead of changing the constants for other fiber directions, we rotate the given stress tensor σ. If v is the fiber direction, we just need a rotation matrix R which maps the first unit vector e_1 on v, i. e.

$$Re_1 = v \ .$$

By applying the Tsai-Hill criterion or the Tsai-Wu criterion on

$$\sigma' = R^T \sigma R$$

we can compute if a material with fibers pointing in direction v can resist a local stressing condition σ. Due to the transversal isotropy the result of the yield criteria is invariant under rotations of σ around the x-axis. This explains why it is only necessary that R maps e_1 to v. The mapping of e_2 and e_3 is arbitrary.

Now we divide the set of all fiber directions into bundles of similar fiber directions. This is equivalent to a partition of the sphere into small regions $A_i \subset \mathbb{S}^2$. The fiber directions represented by $A_1, \ldots, A_n$ are approximated by a single direction $v_1, \ldots, v_n \in \mathbb{S}^2$. Next, we evaluate a yield criterion for each direction v_i as described above. In this way, we can compute all unidirectional fiber directions v_i which cause failure.

For rating arbitrary fiber orientations, we make use of the fiber distribution function ψ, which can be approximated from the fiber orientation tensor a_{ij}. The reconstruction of ψ was briefly discussed in Section 2.5.2, for details on the implementation of this method see [DT06]. With the help of ψ we are able to rate the fiber orientation by computing

$$f(\psi) = \sum_{i \in I_f} A_i \psi(v_i)$$

while the sum runs over the set of indices $i \in I_f$ for which the fiber directions v_i fails. This gives the percentage of fibers pointing in directions where unidirectional fiber orientations would cause failure. Now, a fiber orientation is assumed to fail if this percentage exceeds a predefined threshold t.

The function f was constructed in a discrete way for a more vivid presentation and since this reflects the implementation. Alternatively, f can be defined continuously.

Let $F \subset \mathbb{S}^2$ be the set of fiber directions v for which the material fails, then

$$f(\psi) = \int_{F \subset \mathbb{S}^2} \psi(v)\, dv$$

is again the percentage of fibers causing failure.

3.2.2 Classifying Regions

In order to show possible optimizations of the fiber orientation, we want to partition the component into four different regions, colored green, yellow, orange, and red. Green regions classify parts where the failure criterion indicates that the material resists, independent of the fiber orientation. Yellow and orange regions mark parts where the fiber orientation influences the result of the yield criterion. If the actual fiber orientation indicates failure it is colored orange, otherwise yellow. Regions where no local fiber orientation can prevent failure are colored red.

From a theoretical point of view, a point with a set of failing fiber directions F and fiber distribution ψ is

- red, if $F = \mathbb{S}^2$,
- orange, if $\emptyset \neq F \subsetneq \mathbb{S}^2$ and $f(\psi) > t$,
- yellow, if $\emptyset \neq F \subsetneq \mathbb{S}^2$ and $f(\psi) \leq t$,
- green, if $F = \emptyset$.

However, in case of orange F might cover almost the whole sphere, leaving just a small area uncovered. Then a specific, almost unidirectional fiber orientation would be necessary to avoid failure, which might be impossible in practice. The reconstruction of the fiber distribution function reflects this fact, i. e. the reconstructed fiber distribution functions, as described in Section 2.5.2, are rather smooth. In particular, unidirectional fiber orientations are excluded, since the corresponding fiber distribution function is a Dirac delta function.

Thus we want to consider only regions as orange if there is a real chance that a reconstructed fiber distribution function ψ fulfills $f(\psi) \leq t$. Since it is very costly to compute if there exists a reconstructed ψ for an arbitrary F satisfying this condition, we define a global maximum for the area of F on $\mathbb{S}^2$. For this we consider the sharpest possible reconstructed ψ, which is the reconstruction from the fiber orientation tensor a_{ij} representing an unidirectional fiber orientation. Lets assume fibers pointing in x-direction, i. e. $a_{11} = 1$ and $a_{ij} = 0$ for all other components. Now we want to compute the maximal area of F which allows that ψ fulfills $f(\psi) \leq t$. Due the spherical symmetry of our ψ around the x-axis the desired F covers the whole sphere with the exception of spherical regions around the poles of $\mathbb{S}^2$ on the

x-axis. Thus we can find an upper bound for the area of F by integrating ψ over increasing regions around the pole. If this integral exceeds $1 - t$, the complement of the domain of integration is the desired F.

The upper bound computed in this way is precise if F is a circular region, otherwise it serves as an approximation. Similarly, a lower bound is computed for the area of F in case of yellow. If F is small enough that even the worst reconstructed fiber distribution satisfies $f(\psi) \leq t$, then we want to consider these regions as green. In this case we proceed as above, but here F is given as the spherical region around the poles for which the integral is equal to t.

3.2.3 Visualization Using Glyphs

We have distinguished four different regions of a component in the last section, where orange regions are especially interesting. In this regions an optimization of the component might be possible by modifying the fiber orientation. To indicate improved fiber orientations we use two kinds of glyphs. The first glyph is designed to show the preferred directions for the fibers. Moreover we use a modified version of superquadrics to visualize the current fiber orientation. Using the function $f(\psi)$, which gives the amount of fibers pointing in disadvantageous directions, we can easily place the glyphs at the crucial points.

Visualizing Preferred Fiber Directions

In Section 3.2.1 the set $F \subset \mathbb{S}^2$ was defined as the directions where unidirectional fiber orientations would cause failure. The goal is a fiber distribution with as few as possible fiber directions contained in F, thus it is comprehensible to visualize the directions F. For this we consider the boundary points of F and connect them with the origin, this results in a cone separating fiber orientations causing failure from those that do not. This new kind of glyph makes it easy to identify the desired fiber orientations. Some examples of this glyphs are shown in Figure 3.3 alongside with the glyphs for the fiber orientation described in the next section.

Visualizing Fiber Orientation Tensors

In our case we are mostly interested in the fiber distribution function which is associated with the fiber orientation tensor. Thus a visualization of the reconstructed fiber orientation function ψ, as described in Section 2.5.2, might be a solution. This could, for example, be achieved by altering the radius of a sphere according to the function values. However, as mentioned above the reconstructed ψ is rather smooth, moreover it can have small negative values. Due to such artifacts this does not result in an easily understood visualization. Instead we consider the precise reconstruction of the fiber distribution function for a unidirectional fiber orientation.

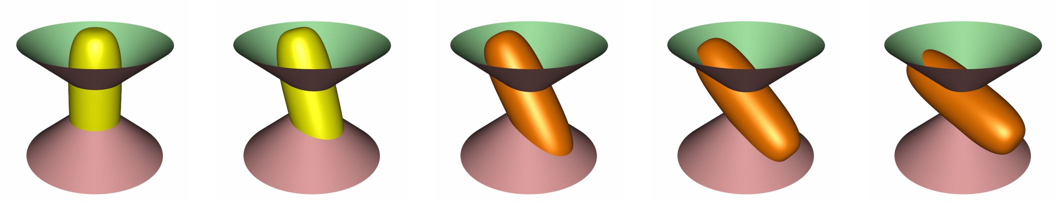

(a) *Stress is constant while the fiber orientation tensor rotates*

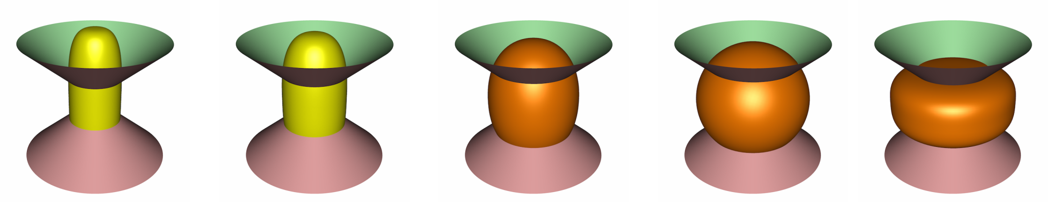

(b) *Stress is constant while the fiber orientation changes from a rather aligned to a rather planar distribution*

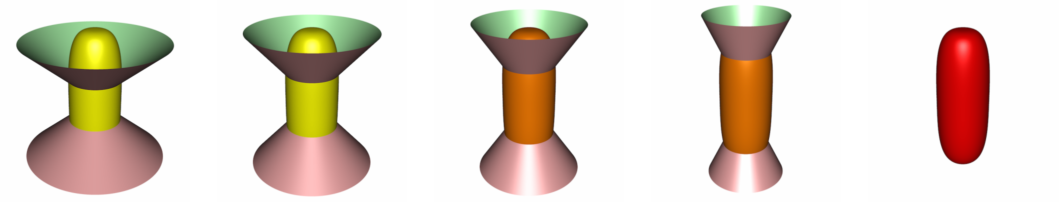

(c) *Fiber orientation is constant while the stress in z-direction increases*

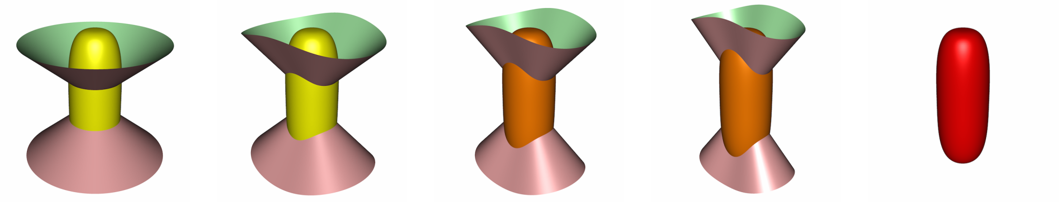

(d) *Fiber orientation and stress in z-direction is constant while additional stress in y-direction is added*

Figure 3.3: *Glyphs visualizing the desired fiber directions and the fiber orientation tensor. Admissible fiber directions lie on the green side of the cones, directions causing failure are located on the red side. These directions depend on the stress tensor. For the visualization of the fiber orientations superquadrics are used. The color indicates if the fiber orientation causes failure (orange/red) or not (yellow), while red means that every other fiber orientation would also fail.*

This is represented by a fiber distribution tensor with eigenvalues $\lambda_1 = 1$, $\lambda_2 = \lambda_3 = 0$, and the precise reconstruction would yield a Dirac delta function. Of course, it is also not possible to properly visualize a Dirac delta function but one would expect a rod-shaped glyph in this case. Similarly, for a planar distribution, which corresponds to eigenvalues of $\lambda_1 = \lambda_2 = 1/2$, $\lambda_3 = 0$, one would expect a disk-shaped glyph, and for a uniform distribution with eigenvalues $\lambda_1 = \lambda_2 = \lambda_3 = 1/3$ a sphere is preferable. These three cases are also denoted as linear, planar and spherical, respectively. Superquadrics, see [Kin04] and [SK10] for details, are quite close to what we want here, but some adjustments are needed to meet our requirements. Like many other tensor glyphs superquadrics vanish when an eigenvalue of the tensor is zero, and this is the case for unidirectional and planar fiber distributions. To avoid this, we shift zero eigenvalues slightly in the positive range. Furthermore, since the fiber orientation tensor has a trace of one, the spherical glyph has a radius of 1/3, a disc-shaped glyph has a radius of 1/2 and a rod-shaped glyph has length one. This makes the spherical and the disc-shaped glyph to look rather small. So we adjust the radii of these glyphs to create glyphs which appear to be equally sized. This is achieved by an affine linear transformation of the eigenvalues of each fiber orientation tensor

$$\lambda \mapsto m + \left(\frac{M - m}{\lambda_1}\right)\lambda \ ,$$

where M is the desired maximal radius and m the desired minimal radius, i. e. the largest eigenvalue is mapped to M and an eigenvalue of zero is mapped to m. We choose M and m separately for the linear, planar, spherical case, and interpolate between the three cases using the anisotropy metrics c_l, c_p and c_s by Westin [WPG$^+$97]. Now, if M_l, M_p, M_s and m_l, m_p, m_s are the maximal and minimal radii for the planar, linear and spherical case, respectively, we set

$$M = c_l M_l + c_p M_p + c_s M_s \ ,$$

$$m = c_l m_l + c_p m_p + c_s m_s \ .$$

The values used in this work are given by $M_l = 1.0$, $M_p = 0.75$, $M_s = 0.6$ and $m_l = 0.1$, $m_p = 0.05$, $m_s = 0$. The resulting glyphs are shown in Figure 3.4.

Glyph Placement

Our goal is to place glyphs preferably at points where the current fiber distribution is disadvantageous. The value $f(\psi)$ is used for this purpose. The higher the value, the more disadvantageous the fiber distribution is. This allows an easy approach for placing glyphs on all relevant positions. First, the value of $f(\psi)$ is computed for all data points and sorted in decreasing order. Then, the first point is chosen, i. e. the point with the highest value. Subsequently, all points within a neighborhood of

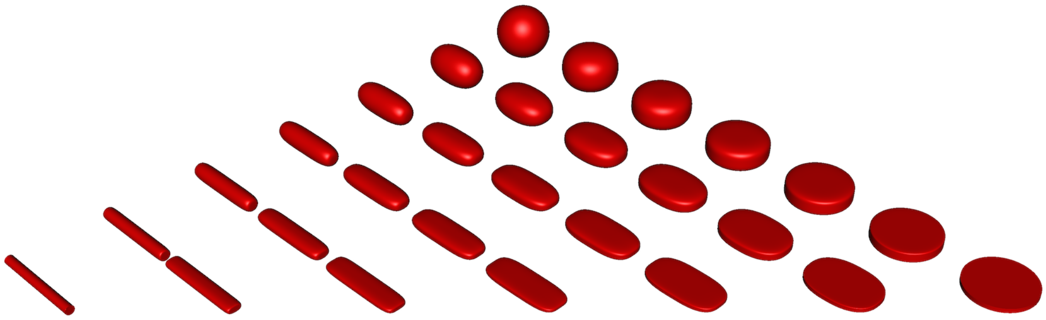

Figure 3.4: *Superquadrics adapted for the visualization of fiber orientation tensors. The tensors are interpolated over a triangle with vertices representing the linear, planar and spherical case.*

predefined size are removed. This procedure of choosing the first point and removing all points within a neighborhood is repeated until there are no points left. The size of the neighborhood has to be chosen carefully, if the size is too large important features can be missed, a small size results in a high number of glyphs and produces clutter. To find the proper value easily, the user can interactively control the size of the regions, as well as the size of the glyphs.

3.3 Results and Discussion

Two datasets are used to evaluate the proposed method. The first is a tensile bar, a specimen used to perform experiments as depicted in Figure 2.2. Such specimen can be produced with an almost unidirectional fiber orientation in tensile direction, so we know that the fiber orientation is satisfactory here. This allows to check if the proposed method works properly. The dataset was created by Marc Schoeneich from the Chair for Plastics Technology at TU Dortmund University. As a second example the triangular wrench described in Section 3.1 is used, three different fiber orientations are compared here. This datasets were created by Michael Stanko from the Chair for Plastics Technology at TU Dortmund University.

As failure criterion the Tsai-Wu criterion is used. Due to its ability of distinguishing tensile and compressive stresses, it is the more advanced one. For the calibration of this failure criteria the constants X_t, X_c, Y_t, Y_c, S_{12} are needed. The material used in the simulations is PBT GF 20, a polybutylene terephthalate with 20% short glass fibers. This material is considered also in [Kai13, p. 91] where the values $X_t = 102.54$, $X_c = 140.30$, and $S_{12} = 57.87$ are measured experimentally. Furthermore, $Y_t = 52$ and $Y_c = 72$ are determined virtually by simulation since it is not feasible to perform the necessary experiments, see [Kai13, p. 105].

It is also necessary to choose the threshold t which defines the maximum percentage of fibers allowed to point in directions where unidirectional fiber distributions would cause failure. Obviously, it would make not much sense to choose $t > 0.5$, since this would allow that a majority of fibers points into directions causing failure. In contrast, a very strict choice, e. g. $t = 0.1$ or less, would make it rather hard for a fiber distribution to meet this requirement in many situations. Defining a precise value for t would certainly need a thorough investigation including experiments which is beyond the scope of this work. For experiments discussed here $t = 0.2$ was used, which is a cautious choice but not too restrictive.

Tensile Bar

A stretching of 1 mm is simulated for the tensile bar, see Figure 3.5. During the simulation process the stretching is increased progressively, which leads to a time parameter ranging from 0 to 1. At first the red, orange and yellow regions for all time steps are computed and its temporal development is shown in a graph, see Figure 3.6. The graph shows the number of elements of the respective regions during the simulation process. We can observe here that the first yellow elements arise after a stretching of about 0.27 mm and increase rapidly. However, the first orange elements appear much later when the stretching reaches 0.64 mm. Shortly after, at about 0.68 mm, the first elements turn red. This indicates that the fiber orientation is really good here and there is not much to optimize. And this is exactly what is expected here, since the fibers are almost perfectly aligned in the direction of stretching.

Now we can select a time step from the graph and have a closer look at the colored regions for a stretching of 0.64 mm, 0.68 mm and 0.75 mm, see Figure 3.7 top. Considering our glyphs showing preferred fiber directions and the current fiber distribution, we can also see that the fibers are pretty much aligned in stressing direction, see Figure 3.7 bottom. Moreover we observe that the cones are diminishing with increasing stretching. This indicates that decreasing variations of the fiber orientation are allowed if the stresses increase.

Triangular Wrench

As a second example we consider the triangular wrench. We investigate the fiber orientations produced by three different gates, i. e. three different points of injection, see Figure 3.8. An increasing force of up to 200 N acting on the wrench is simulated. We start with a fiber orientation produced with a gate on the side, see Figure 3.8a. The first orange elements occur after a time of 0.4 which corresponds to a force of 80 N, i. e. the force becomes critical here. The orange region is shown in the upper

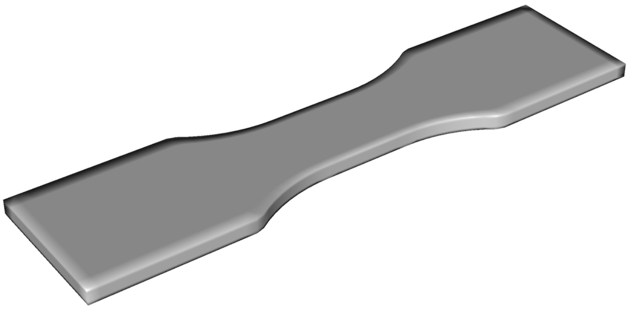

Figure 3.5: *Geometry of the tensile bar*

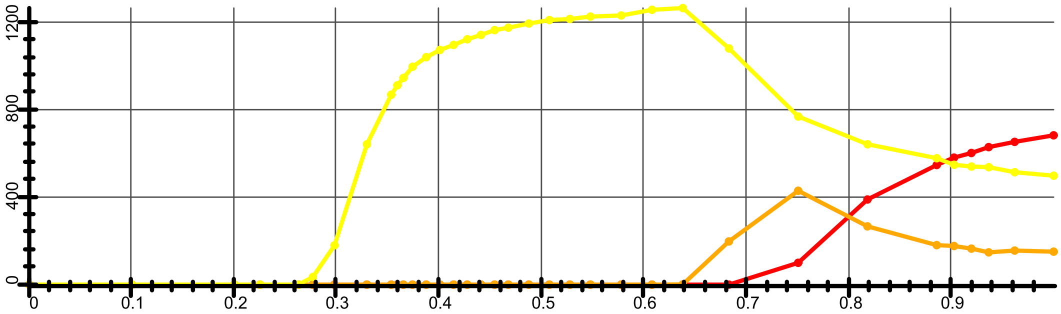

Figure 3.6: *Graph showing the number of red, orange and yellow elements over time*

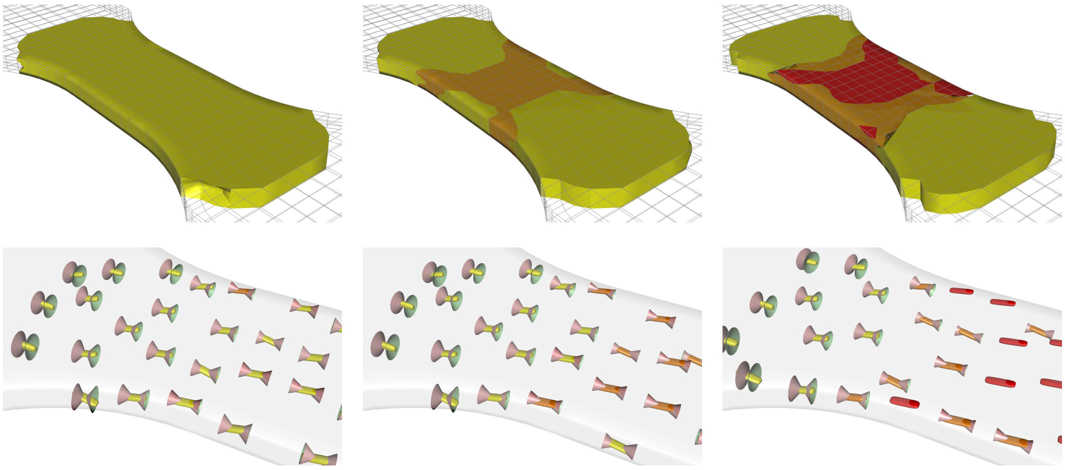

Figure 3.7: *The tensile bar for a stretching of 0.64 mm, 0.68 mm and 0.75 mm (from left to right). Red, orange and yellow regions are shown in the upper row, glyphs visualizing fiber orientations and admissible fibers are shown in the lower row.*

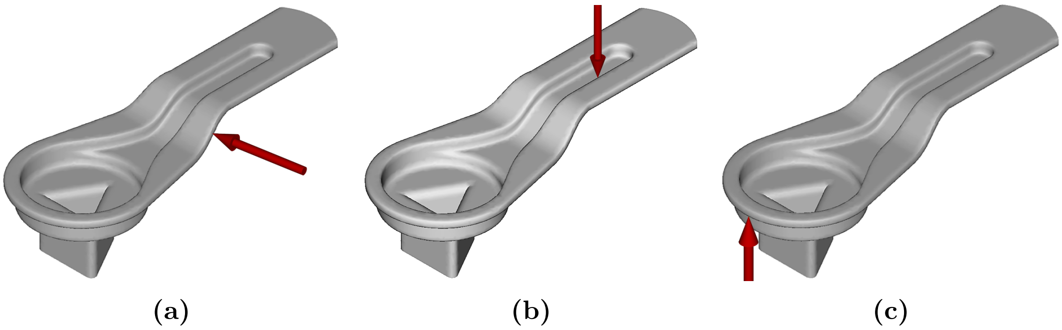

Figure 3.8: *Different gates for producing the wrench by injection molding*

image of Figure 3.9a. The glyphs for this region (lower image) reveal that the fiber orientation is very inadequate to sustain the load. Many fibers point in directions which are on the red side of the cone, so the fiber orientation is obviously responsible for the material failure here.

This is clearly a result of the chosen gate on the side, since the fibers are aligned with the flow of the melt. Next the gate is moved to the top, see Figure 3.8b. This brings a significant improvement, the number of orange elements for 80 N is reduced from 362 for case (a) to 47 for case (b). Consequently the orange region (Figure 3.9b top) is much smaller. The corresponding glyphs show that the fiber orientation is much better and even in the orange regions a large number of fibers points into admissible directions. Consequently the glyphs also show if the fiber orientation in an orange region might still be acceptable or if it is inappropriate. Unfortunately, a new orange region arises at the end of the wrench for case (b).

Moving the gate to the front of the wrench (3.8c) reduces the number of orange elements further to 41. As we can see in Figure (3.9c), the orange region at the end of the wrench disappears almost completely, while the fiber orientation in the middle of the wrench is very similar to case (b), i. e. we have no significant loss in this region.

Discussion

As we have seen it is possible to achieve a better fiber orientation by modifying the gate. There are also other parameters in the injection process, like the injection direction, the temperature or the pressure, which can influence the resulting fiber orientation. However, there is no way to precisely control the fiber orientation in an injection process. Moreover, it is possible that even the best parameters for the injection process lead to a fiber orientation which is still not perfect. However, an experienced engineer will be able to choose reasonable injection parameters much better if he knows about the desired fiber orientation. Thus the proposed glyphs

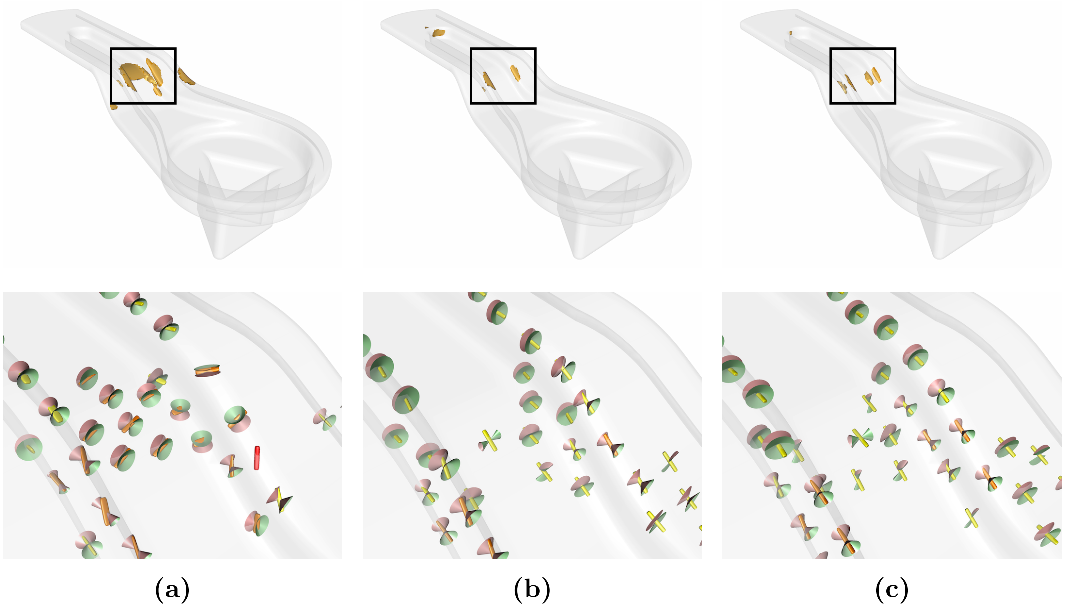
(a) (b) (c)

Figure 3.9: *Orange regions and glyphs for the wrench at a force of 80 N*

give helpful information for the engineer in order to improve the injection process.

Naturally, the question arises whether an automatic optimization of the injection parameters is possible. The computation of the stresses with regard to the fiber orientation takes several hours. Thus very few simulation runs are possible within an acceptable amount of time. This makes an automatic or even semi-automatic optimization not practical with current simulation methods and computing power, though this is a desirable goal for the future.

3.4 Conclusion and Future Work

The design of components is a central task in mechanical engineering. Essentially, the engineer is solving an optimization problem with constraints. After an initial design, a virtual test using structural simulations is performed. This results in a stress tensor field besides other field information. The central question is the potential failure of the design under the predefined load. This question is answered by a failure criterion suitable for the chosen material. This results usually in a simple boolean or single scalar field visualization with fixed threshold.

However, it was shown in this chapter that after the virtual test, there is always the question of potential improvement. This is not really supported by current visualization methods besides indicating the failure region. The engineer can always change the geometric design. In case of composite materials, he can also steer the material properties in a certain region by changing the production process, in our case injection molding. This opens an interesting way of improvement because it typically won't change production cost, production speed, or component weight, i. e. the overall cost function. The new feature-based visualization proposed in this chapter does not only inform the engineer where his design might fail, it also shows how far failure is caused by a disadvantageous fiber orientation and how it can be improved. This information is presumably very useful for changing the production process in order to obtain a fiber orientation which leads to a more stable component. The visualization gives a simple, efficient overview and presents details in the critical parts of the design. This includes a new type of glyph showing the admissible fiber directions, as well as modified superquadrics for visualizing fiber orientation tensors. In the results section it is demonstrated how this visualization can be interpreted.

Regarding the future work, there are several aspects of this work that leave room for improvements. So far, there is only informal evidence for the use of this method. Therefore, it needs to be checked in how far the used hypothesis is suitable to predict failure in dependence of arbitrary fiber distributions. This includes also a proper investigation of the threshold t. Also the influence of the fiber orientations in the structure simulation needs to be studied. Modified fiber orientations can have an effect on the stresses. Currently, this effect is ignored but its influence needs to be checked, especially in the context of optimizing the injection molding process.

4

Visualizing Gradients of Stress Tensor Fields

The methods proposed in this chapter are again motivated by the prediction of failure in engineering. We have already discussed in the last chapter, that for the prediction of failure usually a structure simulation is performed, which computes the stresses inside the material under a predefined load condition. In a next step, a failure criterion is used to evaluate the resulting stress tensor. Such yield criteria, like the von Mises stress or the Tsai-Hill criterion, are usually functions depending on the stress tensor, cf. Section 2.4.2. However, there is some evidence that not only the stress at a single point is decisive for failure, but also the stress values in the vicinity, i. e. the gradient of the stress tensor. For example, the stress gradient is used to analyze the effect of stress concentrations caused by notches. The so-called notch effect plays an important role for fatigue of materials, see for example [MRK03] or [Rad13]. In this case, the material is analyzed under a simple load condition, i. e. a unidirectional stretching, such that the stress can be reduced to a scalar quantity. Then the derivative in direction perpendicular to the notch surface is considered.

This makes it promising to consider the gradient of the stress tensor for failure prediction also in other situations. But for many technical materials there is no obvious or sufficiently proven way to reduce the stress tensor to a scalar value that describes the material stressing adequate. Thus a thorough understanding of the whole stress gradient is desirable to examine the effects of the stress gradient on material failure. In this chapter some first visualizations to analyze the whole gradient of the stress tensor are proposed. The gradient of a three-dimensional stress tensor consists of 18 independent components, given by the partial derivatives of the 6 components of the symmetric stress tensor, cf. Section 2.2.2. Together with the stress tensor itself there are 24 components at each position which have to be visualized. This makes the visualization of these data very challenging.

In this chapter, glyphs are suggested that allow to analyze the stress tensor and its gradient at discrete points. In engineering textbooks the stress tensor is often depicted in terms of the stress tensor, similar to Figure 2.1. Based on such illustrations a glyph that completely visualizes the stress tensor and the gradient is proposed. Due to the complexity of this glyph, the shown information is systematically reduced in the next step, which allows for simpler visualizations. For example, if we are interested in the overall change of the tensor in certain directions, we can reduce directional derivatives, which are symmetric second order tensors, to scalar quantities. Similarly, we can focus on the normal stress in certain directions while neglecting the direction of differentiation. Such visualizations allow to highlight different properties of the full gradient of the tensor consecutively.

4.1 Glyphs for Gradients of Stress Tensor Fields

Our goal is to visualize the stress tensor σ and its gradient $\nabla\sigma$ at single points of a stress tensor field. From such visualizations we want to gain a thorough understanding of the tensor field at points of high load. The information of the stress tensor and its gradient is given by the linearization L of the stress tensor field at a point p, which is given by

$$\begin{aligned} L \ : \ & \mathbb{R}^3 \to \mathrm{Sym}(3) \ , \\ & v \mapsto \sigma(p) + \nabla_v \sigma(p) \ . \end{aligned} \tag{4.1}$$

Thus $L(v)$ is the first order Taylor approximation of σ around p, where $\nabla_v\sigma(p)$ is the directional derivative of σ in direction v, cf. Section 2.2.2. We will usually omit p in the following formulas, since the point p is secondary for the glyphs suggested in the remainder of this section. As mentioned before, we focus on the stress vector. Based on the linearization L we define a map

$$\begin{aligned} \mathbf{t} \ : \ & \mathbb{S}^2 \times \mathbb{S}^2 \to \mathbb{R}^3 \ , \\ & (v, n) \mapsto \sigma n + \varepsilon \nabla_v \sigma n \ , \end{aligned} \tag{4.2}$$

where $\varepsilon > 0$ and $\mathbb{S}^2 \subset \mathbb{R}^3$ denotes the unit sphere. For a given direction of differentiation $v \in \mathbb{S}^2$ and a normal vector $n \in \mathbb{S}^2$, $\mathbf{t}(v, n)$ is the (linearized) change of the stress vector σn for a displacement by ε in direction v. Note that $\nabla_v\sigma n$ is the partial derivative of the stress vector σn. This can be considered as a reinterpretation of the third order tensor $\nabla\sigma$ as a map $\mathbb{R}^3 \times \mathbb{R}^3 \to \mathbb{R}^3$, $(v, n) \mapsto \nabla_v\sigma n$, in terms of Section 2.1.2. The parameter ε serves as a scaling of the gradient, it controls the size of the (linearized) neighborhood taken into consideration. A meaningful choice depends on the dimensions of the data. The stress tensor σ and its gradient $\nabla\sigma$ are still completely characterized by the graph of $\mathbf{t}$ which is given by

$$\left\{(v, n, \mathbf{t}(v, n)) \in \mathbb{R}^3 \times \mathbb{R}^3 \times \mathbb{R}^3 \mid n \in \mathbb{S}^2,\ \ v \in \mathbb{S}^2\right\} \ .$$

The glyphs presented in the following can be considered as visualizations of (parts of) the graph of $\mathbf{t}$. Of course, the graph of $\mathbf{t}$ contains redundant information, thus it is not necessary to visualize the whole graph in order to visualize σ and $\nabla\sigma$. The map $\mathbf{t}$ is linear with respect to n and affine linear with respect to v, moreover σ is symmetric. Thus it is possible to show portions of the graph of $\mathbf{t}$ without losing information. But glyphs which do not show the complete information of σ and $\nabla\sigma$ will be also discussed, with the benefit of easier understandable visualizations.

4.1.1 Visualizing Gradients of Stress Vectors

The glyphs presented in this section extend the depiction of the stress vectors shown in Figure 2.1 with information on the gradient of the stress vectors. The first glyph uses additional arrows which give information on the partial derivatives of the stress vectors. A variant of this glyph shows all stress vectors that occur in a linearized neighborhood.

Partial Derivatives of Stress Vectors

At first the basis vectors are depicted similarly to Figure 2.1. We choose a basis of eigenvectors n_1, n_2, n_3 and show a cube with sides defined by the planes normal to n_1, n_2, n_3. The respective stress vectors $\sigma n_1, \sigma n_2, \sigma n_3$ are shown as gray tubes. Since we use a basis of eigenvectors they are perpendicular to the sides of the cube. Now, the variations of the stress vectors in the coordinate directions e_1, e_2, e_3 are depicted as arrows in red, green or blue, respectively. These arrows are the partial derivatives of the stress vector $\varepsilon\partial_i\sigma n_j$ for $i, j = 1, \ldots, 3$, while the ε adjusts the displacement as in equation (4.2). An example is shown in Figure 4.1. Note that the coordinate system e_1, e_2, e_3 for the directional derivatives might be different to the coordinate system defined by the eigenvectors n_1, n_2, n_3. The coordinate system e_1, e_2, e_3 is usually a global coordinate system which is consistent with the application and intuitive for the user. For example, the tensile bars considered in the next section are aligned parallel to the coordinate axes and the stress direction is parallel to e_3.

The proposed visualization of the stress vectors and its partial derivatives contains the subset

$$\{(v, n, \mathbf{t}(v, n)) \mid n = n_1, n_2, n_3,\ \ v = 0, e_1, e_2, e_3\}$$

of the graph of $\mathbf{t}$. Since $\mathbf{t}$ is linear with respect to n and affine linear with respect to v, this subset describes $\mathbf{t}$ completely. Equivalently, a stress tensor σ is completely

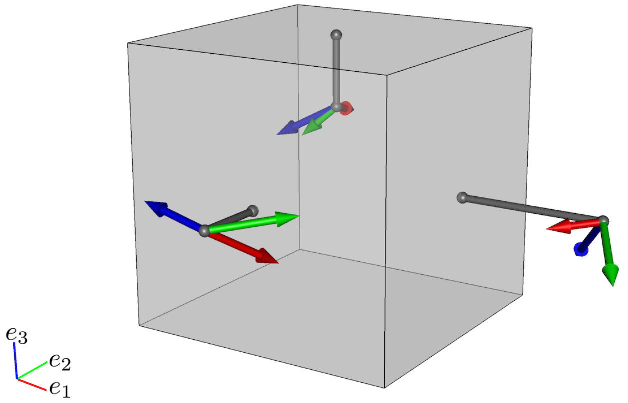

Figure 4.1: *The colored arrows depict directional derivatives of the stress vectors. The red, green, blue arrows correspond to a displacement in direction of* e_1, e_2, e_3*, respectively.*

defined by the three stress vectors $\sigma n_1, \sigma n_2, \sigma n_3$ and the gradient $\nabla\sigma$ is completely defined by the partial derivatives of the stress vectors $\partial_i \sigma n_j$ for $i, j = 1, \ldots, 3$. Consequently, all information of σ and $\nabla\sigma$ is included in this visualization. An obvious drawback of this method is that it needs a thorough examination to read all the information. Especially the direction of differentiation, which is encoded in the colors red, green and blue, might not be immediately apparent for many users. This makes it comprehensible to reduce the presented information and, in return, obtain a visualization that is easier to understand.

Envelope of Stress Vectors under Linear Approximation

As a first simplification of the glyph proposed in the previous section we replace the partial derivatives of the stress vectors, which are shown as red, green and blue arrows. Instead of showing single arrows for the partial derivatives of the stress vectors we show the envelope of all directional derivatives of the stress vectors, i. e. $\varepsilon\nabla_v \sigma n$ for all $v \in \mathbb{S}^2$. In this way we show all stress vectors that occur in a linearized neighborhood of radius ε. An example is shown in Figure 4.2. For a fixed normal vector n, the envelope of all directional derivatives is the image of the unit sphere $\mathbb{S}^2$ under the linear transformation

$$\begin{aligned} \varepsilon\nabla\sigma n \ : \ & \mathbb{R}^3 \to \mathbb{R}^3 \\ & v \mapsto \varepsilon\nabla_v \sigma n \ . \end{aligned}$$

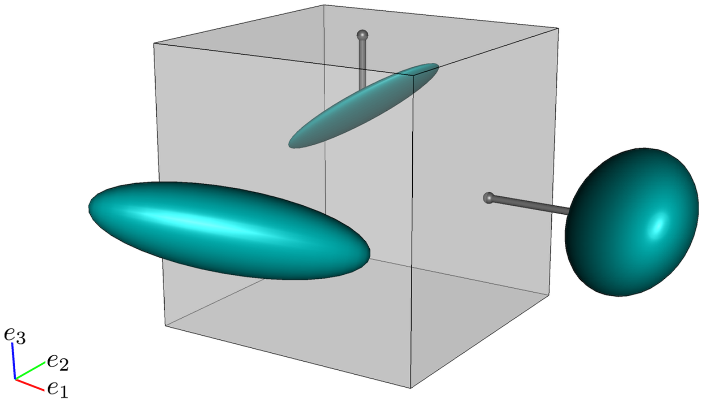

Figure 4.2: *The ellipsoids depict the envelopes of the stress vectors within a linearized neighborhood, i. e. the ellipsoid marks the end points of all stress vectors occurring in this neighborhood.*

Thus the envelopes form ellipsoids, while the principal axes are defined by the eigenvectors of $\varepsilon \nabla \sigma n$ and their radii are given by the absolute values of the corresponding eigenvalues. The depicted information can be summarized as

$$\left\{ (n, \mathbf{t}(v, n)) \mid n = n_1, n_2, n_3, \;\; v \in \mathbb{S}^2 \right\} \ .$$

Note that we lose information on the preimage of v here, but compared to the visualization in Section 4.1.1 we show the image of all $v \in \mathbb{S}^2$ rather than only the image of the three basis vectors. So, if one is interested in the change of the stress vectors in all directions, but the particular direction is not important at first, then this visualization might be simpler to read than the visualization in the previous section.

4.1.2 Reducing Directional Derivatives to Scalar Quantities

In the previous section we have visualized the gradient of the stress tensor completely, but the resulting visualizations might be difficult to read. Now we want to reduce the shown information by focussing on special properties of the gradient. The basic idea is to consider a fixed direction of differentiation $v \in \mathbb{S}^2$ and measure the change of the stress vectors for all normal directions $n \in \mathbb{S}^2$. Or, conversely, for a normal direction $n \in \mathbb{S}^2$ we measure the overall change for all directions of differentiation $v \in \mathbb{S}^2$.

To realize this we reduce $\nabla_v \sigma n$ to a scalar quantity, first. An obvious choice is to use the magnitude, i. e. the euclidean norm $\|\nabla_v \sigma n\|$. Another possibility is using only the directional derivative of the normal stress of $\nabla_v \sigma n$ which is given by $\nabla_v n^\top \sigma n = n^\top \nabla_v \sigma n$. In the next step we compute the average, the maximum or the minimum of these scalar quantities for variable n or v, while v or n is fixed, respectively. This yields functions $\mathbb{S}^2 \to \mathbb{R}$ depending on v or n, which are easier to visualize than the complete gradient.

Magnitude of Directional Derivatives of Stress Vectors

At first we consider the magnitude of the directional derivatives of the stress vector. Computing the average/minimum/maximum of $\|\nabla_v \sigma n\|$ for all n or v might seem expensive, but by using some mathematical conversions these quantities can be computed efficiently. Note that we have for any matrix $A \in \mathbb{R}^{3,3}$

$$\int_{\mathbb{S}^2} x^\top A x \, dx = \frac{4\pi}{3} \operatorname{tr} A \ . \tag{4.3}$$

Thus, if we use the L^2-norm for averaging $\|\nabla_v \sigma n\|$ over $n \in \mathbb{S}^2$ we obtain

$$\begin{aligned}\sqrt{\int_{\mathbb{S}^2} \|\nabla_v \sigma n\|^2 \, dn} &= \sqrt{\int_{\mathbb{S}^2} n^T (\nabla_v \sigma)^T (\nabla_v \sigma) n \, dn} \\ &= \sqrt{\frac{4\pi}{3}} \sqrt{\operatorname{tr}\left((\nabla_v \sigma)^\top (\nabla_v \sigma)\right)} = \sqrt{\frac{4\pi}{3}} \|\nabla_v \sigma\|_F \ ,\end{aligned}$$

where $\|\nabla_v \sigma\|_F$ denotes the Frobenius norm of $\nabla_v \sigma \in \mathbb{R}^{3,3}$, i. e. the Frobenius norm of the directional derivative of σ in direction v. Similarly, for the average over $v \in \mathbb{S}^2$ we have

$$\sqrt{\int_{\mathbb{S}^2} \|\nabla_v \sigma n\|^2 \, dv} = \sqrt{\frac{4\pi}{3}} \|\nabla \sigma n\|_F \ ,$$

while $\nabla \sigma n$ is the gradient of the stress vector σn. In this way we can compute the average by computing the Frobenius norm of a matrix, rather than computing the integral.

The extrema of $\|\nabla_v \sigma n\|$ for all $n \in \mathbb{S}^2$ or all $v \in \mathbb{S}^2$ can be computed from the following consequence of the Courant-Fischer theorem. For any symmetric matrix A we have

$$\max_{x \in \mathbb{S}^2} x^\top A x = \lambda_{max}(A) \ , \quad \min_{x \in \mathbb{S}^2} x^\top A x = \lambda_{min}(A) \ , \tag{4.4}$$

while $\lambda_{min}(A)$ and $\lambda_{max}(A)$ denote the smallest and the largest eigenvalue of A, respectively. Now, the maximum of $\|\nabla_v \sigma n\|$ for all $n \in \mathbb{S}^2$ is given by

$$\max_{n\in\mathbb{S}^2} \|\nabla_v \sigma n\| = \sqrt{\max_{n\in\mathbb{S}^2} n^T (\nabla_v \sigma)^\top (\nabla_v \sigma) n} = \sqrt{\lambda_{max}\left((\nabla_v \sigma)^\top (\nabla_v \sigma)\right)} \ ,$$

and the minimum is given by

$$\min_{n\in\mathbb{S}^2} \|\nabla_v \sigma n\| = \sqrt{\lambda_{min}\left((\nabla_v \sigma)^\top (\nabla_v \sigma)\right)} \ .$$

In a similar way we obtain for the extrema of $\|\nabla_v \sigma n\|$ with respect to v, which are given by

$$\max_{v\in\mathbb{S}^2} \|\nabla_v \sigma n\| = \sqrt{\lambda_{max}\left((\nabla \sigma n)^\top (\nabla \sigma n)\right)} \ ,$$

$$\min_{v\in\mathbb{S}^2} \|\nabla_v \sigma n\| = \sqrt{\lambda_{min}\left((\nabla \sigma n)^\top (\nabla \sigma n)\right)} \ .$$

Note that for any matrix A the largest singular value is $\sqrt{\lambda_{max}(A^\top A)}$, and the smallest singular value is $\sqrt{\lambda_{min}(A^\top A)}$, so the extrema of $\|\nabla_v \sigma n\|$ over n or v are given by the largest and smallest singular values of $\nabla_v \sigma$ and $\nabla \sigma n$, respectively. Since $\nabla_v \sigma$ is symmetric, the largest and smallest singular values of $\nabla_v \sigma$ are also largest and smallest absolute eigenvalues of $\nabla_v \sigma$, respectively.

To sum up, for a fixed direction of differentiation $v \in \mathbb{S}^2$ we can compute the average/minimal/maximal change of the stress vectors for all $n \in \mathbb{S}^2$ from the Frobenius norm or the singular values of $\nabla_v \sigma$. And for a fixed normal vector $n \in \mathbb{S}^2$ we can compute the average/minimum/maximum over all directions of differentiation $v \in \mathbb{S}^2$ from the Frobenius norm or the singular values of $\nabla \sigma n$.

As an example we consider the average of $\|\nabla_v \sigma n\|$ for all normal vectors $n \in \mathbb{S}^2$, i. e. we want to visualize $\sqrt{4\pi/3}\|\nabla_v \sigma\|_F$ for each direction v. The values of $\|\nabla_v \sigma\|_F$ can be computed for each v by a quadratic form which is defined by a matrix Q. If we denote the partial derivatives of σ by $\partial_1\sigma, \partial_2\sigma, \partial_3\sigma$ we have

$$\begin{aligned}
\|\nabla_v\sigma\|_F &= \|v_1\partial_1\sigma + v_2\partial_2\sigma + v_3\partial_3\sigma\|_F \\
&= \left(\operatorname{tr}\left((v_1\partial_1\sigma + v_2\partial_2\sigma + v_3\partial_3\sigma)^T(v_1\partial_1\sigma + v_2\partial_2\sigma + v_3\partial_3\sigma)\right)\right)^{\frac{1}{2}} \\
&= \left(v_1^2\operatorname{tr}(\partial_1\sigma^2) + v_2^2\operatorname{tr}(\partial_2\sigma^2) + v_3^2\operatorname{tr}(\partial_3\sigma^2)\right. \\
&\qquad \left.+2v_1v_2\operatorname{tr}(\partial_1\sigma\partial_2\sigma) + 2v_1v_3\operatorname{tr}(\partial_1\sigma\partial_3\sigma) + 2v_2v_3\operatorname{tr}(\partial_2\sigma\partial_3\sigma)\right)^{\frac{1}{2}} \\
&= \left(v^T\begin{bmatrix} \operatorname{tr}(\partial_1\sigma^2) & \operatorname{tr}(\partial_1\sigma\partial_2\sigma) & \operatorname{tr}(\partial_1\sigma\partial_3\sigma) \\ \operatorname{tr}(\partial_1\sigma\partial_2\sigma) & \operatorname{tr}(\partial_2\sigma^2) & \operatorname{tr}(\partial_2\sigma\partial_3\sigma) \\ \operatorname{tr}(\partial_1\sigma\partial_3\sigma) & \operatorname{tr}(\partial_2\sigma\partial_3\sigma) & \operatorname{tr}(\partial_3\sigma^2)\end{bmatrix} v\right)^{\frac{1}{2}} =: \left(v^TQv\right)^{\frac{1}{2}} \quad .
\end{aligned}$$

The matrix Q is symmetric and positive semidefinite, this allows for a simple visualization of Q by an ellipsoid. We use the eigenvectors v_1, v_2, v_3 of Q as the principal axes and the square roots of the eigenvalues as the corresponding radii. If we scale Q by $4\pi\varepsilon^2/3$, then the radii are equal to $\sqrt{4\pi/3}\|\varepsilon\nabla_{v_i}\sigma\|_F$ for $i = 1, 2, 3$. This is the average variation of all stress vectors σn for a displacement by ε in direction v_i, measured by $\|\nabla_{v_i}\sigma n\|$ as described above. The information shown by such an ellipsoid can be summarized as

$$\left\{\left(v, \sqrt{\frac{4\pi}{3}}\|\varepsilon\nabla_v\sigma\|_F\right) \mid v \in \mathbb{S}^2\right\} \quad .$$

The resulting ellipsoid is shown in Figure 4.3 in purple, it shows the same gradient as in the previous Figures 4.1 and 4.2. Additionally the stress tensor is shown as an ellipsoid in yellow, while an exponential mapping has been applied on the stress tensor in order to obtain positive eigenvalues. Of course we are losing a lot of information by showing the gradient in this way. However, the overall change of the stress vectors in a certain direction can be seen much easier than from the visualization in Section 4.1.1.

Directional Derivatives of Normal Stress

Now we derive the average/minimum/maximum of the directional derivative of the normal stress $n^\top\nabla_v\sigma n$ for all n while v is fixed or for all v while n is fixed. If we integrate $n^\top\nabla_v\sigma n$ for all $n \in \mathbb{S}^2$ to compute the average, then we obtain by equation (4.3)

$$\int_{\mathbb{S}^2} n^\top\nabla_v\sigma n \, dn = \frac{4\pi}{3}\operatorname{tr}\left(\nabla_v\sigma\right) \quad .$$

An average with respect to v makes no sense here, since $n^\top\nabla_v\sigma n$ is linear in v, thus the integral would be zero. Using equation (4.4) the extrema of $n^\top\nabla_v\sigma n$ for $n \in \mathbb{S}^2$

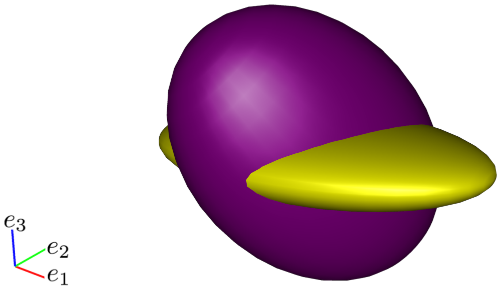

Figure 4.3: *The purple ellipsoid visualizes how much the stress tensor changes in certain directions. This is measured by the Frobenius norm of the directional derivative, which is equivalent to an averaged change of all stress vectors. The yellow ellipsoid shows the stress tensor itself.*

are given by

$$\max_{n\in\mathbb{S}^2} n^\top \nabla_v \sigma n = \lambda_{max}(\nabla_v\sigma) \ , \quad \min_{n\in\mathbb{S}^2} n^\top \nabla_v \sigma n = \lambda_{min}(\nabla_v\sigma) \ .$$

For the extrema with respect to $v \in \mathbb{S}^2$ we obtain

$$\max_{v\in\mathbb{S}^2} n^\top \nabla_v \sigma n = \|n^\top \nabla\sigma n\| \ , \quad \min_{v\in\mathbb{S}^2} n^\top \nabla_v \sigma n = -\|n^\top \nabla\sigma n\| \ .$$

due to the linearity of $n^\top \nabla_v \sigma n$ in v. Note that $n^\top \nabla \sigma n = \nabla(n^\top \sigma n) \in \mathbb{R}^3$ is the gradient of the normal stress with respect to n.

As an example we consider $n^\top \varepsilon \nabla_v \sigma n$ for fixed n and consider the minimum and the maximum change of the normal stress in all directions $v \in \mathbb{S}^2$, i. e. the minimal or maximal normal stress in a linearized neighbourhood of radius ε. If we add this minimum or maximum to the actual normal stress $n^\top \sigma n$ we obtain the minimal/maximal normal stress of $\mathbf{t}(v,n)$ in a linearized neighborhood, which is given by

$$\max_{v\in\mathbb{S}^2} n^\top \mathbf{t}(v,n) = n^\top \sigma n + \max_{v\in\mathbb{S}^2} n^\top \varepsilon \nabla_v \sigma n = n^\top \sigma n + \varepsilon \|n^\top \nabla \sigma n\| \ ,$$

and for the minimum

$$\min_{v\in\mathbb{S}^2} n^\top \mathbf{t}(v,n) = n^\top \sigma n - \varepsilon \|n^\top \nabla \sigma n\| \ .$$

The computed extrema are visualized for each n by a surface, while the distance of the surface from the origin is given by the respective extrema. If the normal stress

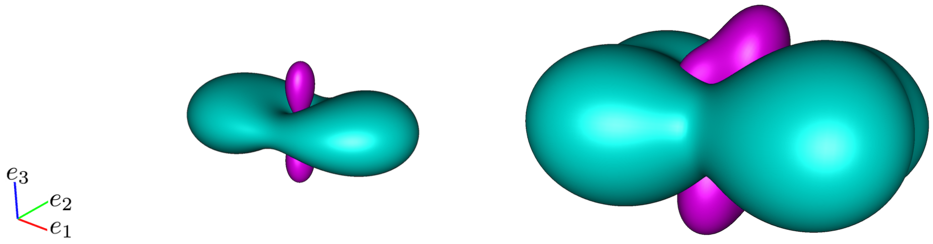

Figure 4.4: *The left image shows a Reynolds glyph, the distance from the origin depicts normal stress in this direction. Turquoise corresponds to positive values, pink corresponds to negative values. The right image shows the envelope of all Reynolds glyphs in a linearized neighborhood.*

$n^\top \sigma n$ is positive the maximum is shown in turquoise, if it is negative the minimum is shown in pink. Consequently, the visualized information is given by

$$\left\{\left(n, \max_{v\in\mathbb{S}^2} |n^\top \mathbf{t}(v,n)|\right) \,\middle|\, n \in \mathbb{S}^2\right\} \ .$$

Note that the surface with distance $n^\top \sigma n$ from the origin forms a Reynolds glyph, i. e. the glyph is obtained by scaling all normal vectors n by the normal stress of σ with respect to n, see for example [HYW$^+$03]. Thus the shown surface can be considered as the envelope of all Reynold glyphs in a linearized neighborhood of radius ε, an example is shown in Figure 4.4.

4.2 Application to Tensile Bars

As a simple practical example we consider simulated stress tensor fields for two different tensile bars. The datasets were provided by Prof. Dr. Markus Stommel and Jannik Nahrgang from the Chair for Plastics Technology at TU Dortmund University. The commercial software package ABAQUS was used to perform the simulations. Tensile bars are used to check the behavior of a material under load. Here we consider two tensile bars with differently curved notches, which result in different stressing conditions. The stress becomes maximal at the notch and the load was adjusted in order to obtain similar stress tensors at this point. For the stronger curved notch a lower nominal tensile load is necessary to obtain a similar stress tensor.

The geometries of the tensile bars are shown in Figure 4.5, the green dots at the center of the notches indicate the points where we want to analyze the gradients. In Figure 4.6 we show the stress vectors and their gradients as described in Section

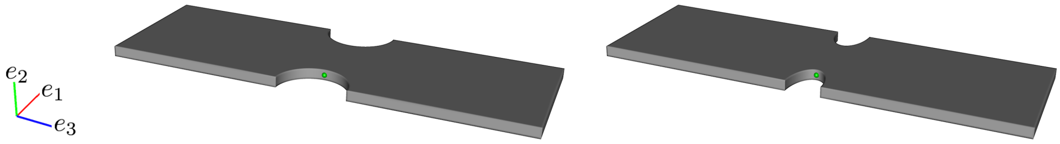

Figure 4.5: *Geometry of the two tensile bars, one with a less curved notch on the left and one with a stronger curved notch on the right. The green dot indicates the point where we analyze the gradient.*

4.1.1, the upper image belongs to the tensile bar with less curved notch, the lower image to the tensile bar with stronger curved notch. The gray tubes show that there is almost only tension in e_3-direction, this is the direction in which the bar is stretched. As intended, the stress is very similar for both tensile bars. The red arrows indicate the variation of the stress vectors for a displacement in e_1-direction, i. e. to the middle of the tensile bar. Here we can see for both tensile bars that the normal stress in e_3 direction is decreasing, while some additional normal stress in e_1-direction arises. This effect is more distinct with the stronger curved notch. Thus, while we obtain a similar stress for a lower load in case of the stronger curved notch, the stress decreases also much faster, suggesting a smaller region of high stress. When moving in e_3-direction we obtain additional shear stresses for both tensile bars, as indicated by the blue arrows. This indicates a variation of the principal stress directions, which is caused by the curvature of the notches, consequently this effect is also stronger for the tensile bar with the stronger curved notch.

Figure 4.7 shows the envelopes of the stress vectors introduced in Section 4.1.1. Of course, this visualization does not reveal any new information, but it is easy to see which stress vectors occur in a linearized neighborhood, and that the variation for the second tensile bar is much stronger. Note that the considered point is on the boundary of the tensile bar, thus the linearized neighbourhood exceeds the actual data. Consequently, the ellipsoids show the envelope of the stress vectors for a linear extrapolation of the data.

In Figure 4.8 the Frobenius norm of the directional derivative is visualized by an ellipsoid, alongside with an ellipsoid visualizing the stress tensor as suggested in Section 4.1.2. With this visualization it is easy to see that the stress tensor changes rapidly in x direction, while there is almost no change in y-direction. Again, it is easy to see that the stress tensor changes much faster for the tensile bar with the stronger curved notch.

The Reynolds glyph and the envelope of the Reynolds glyph for a linearized neighborhood are shown in Figure 4.9. These glyphs offer an overview over the absolute variation of the normal stresses, which is, of course, also much bigger for the tensile bar with stronger curved notch.

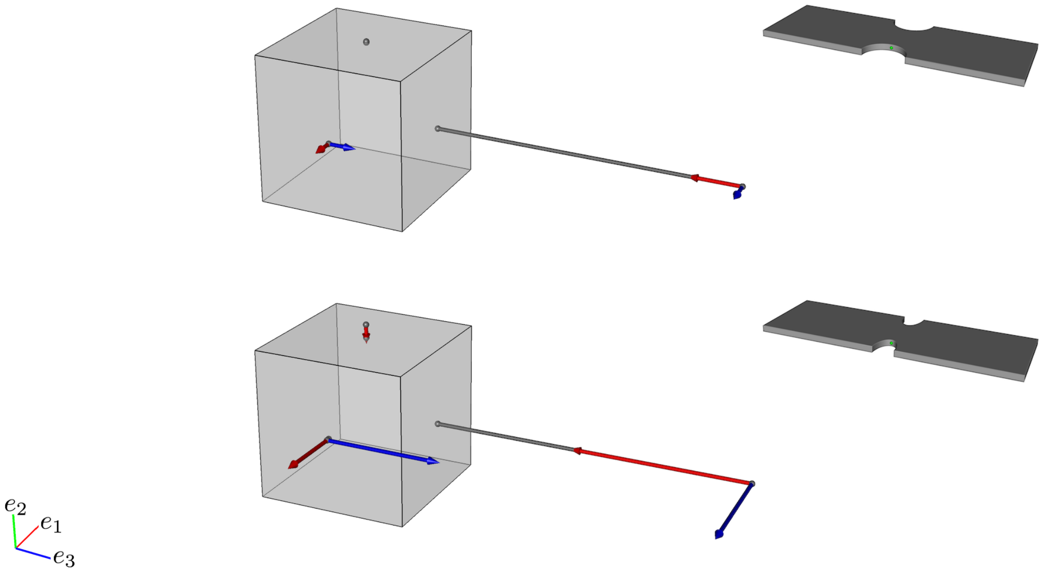

Figure 4.6: *Variation of the stress vectors for a displacement in the coordinate directions. The upper image corresponds to the less curved tensile bar, the lower image to the stronger curved tensile bar.*

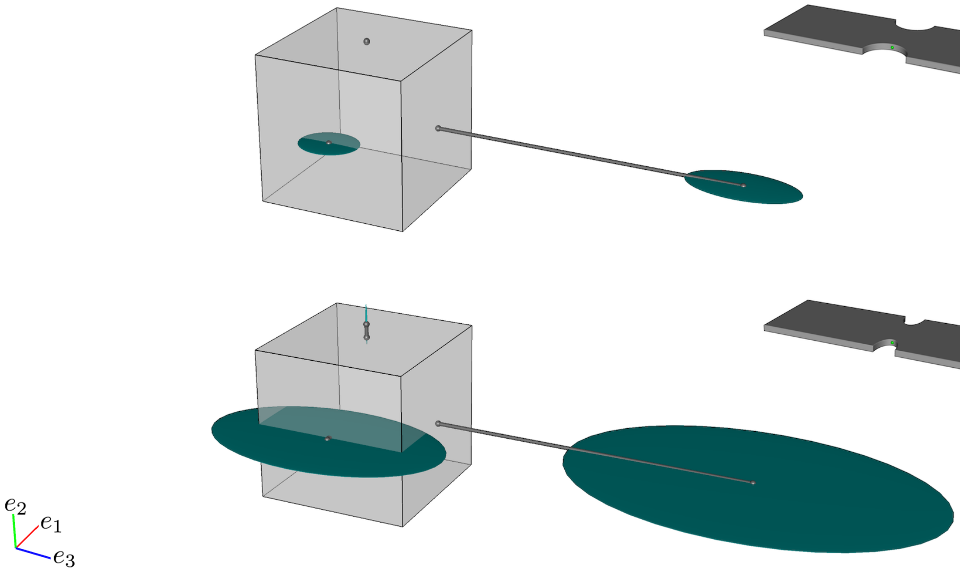

Figure 4.7: *Envelope of the stress vectors in a linearized neighborhood. The upper image corresponds to the less curved tensile bar, the lower image to the stronger curved tensile bar.*

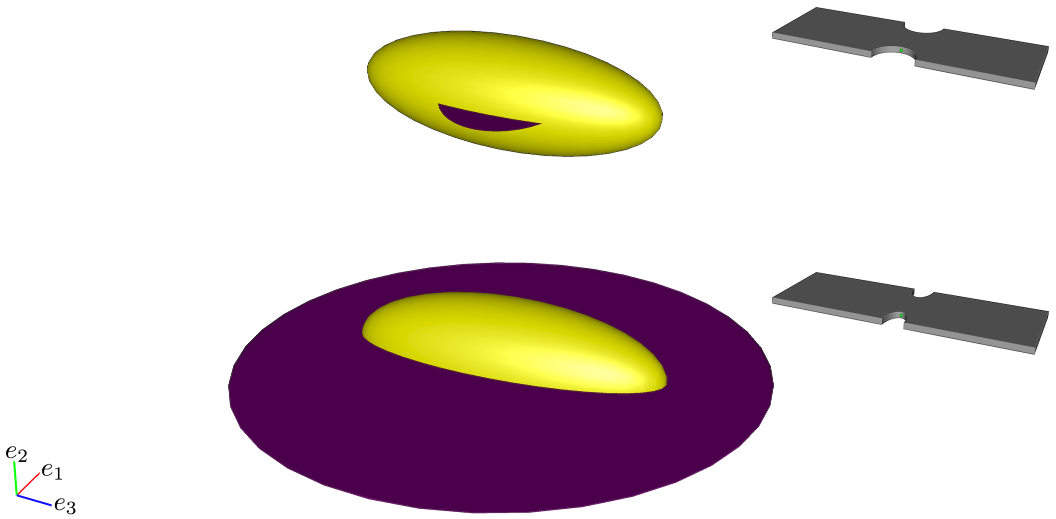

Figure 4.8: *The purple ellipsoid shows the overall change of the stress tensor in all spatial directions, the yellow ellipsoid visualizes the stress tensor. The upper image corresponds to the less curved tensile bar, the lower image to the stronger curved tensile bar.*

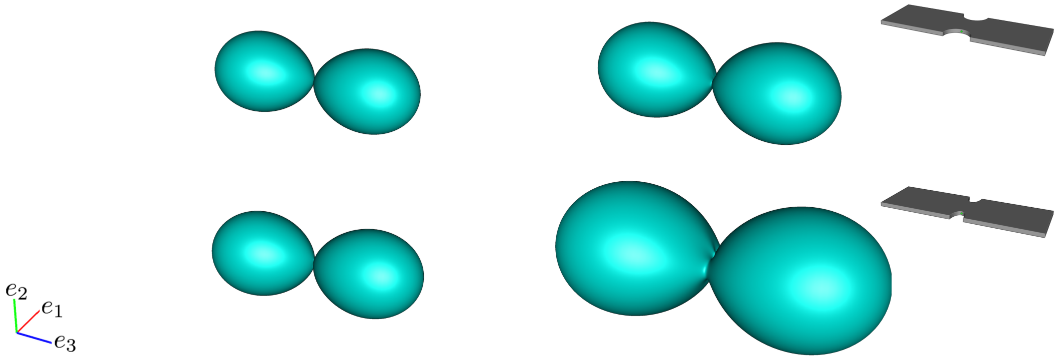

Figure 4.9: *The images show the Reynolds glyph (left) and its envelope (right). The upper image corresponds to the less curved tensile bar, the lower image to the stronger curved tensile bar.*

4.3 Conclusion and Future Work

In this chapter several first ideas for the visualization of the gradient of the stress tensor were suggested. The basic idea was the visualization of the stress vectors and their variation in a linearized neighborhood. A glyph showing the complete information contained in the stress tensor and its gradient was proposed, which is based on commonly used depictions in engineering textbooks. Due to the complexity of this information, several simplifications based on mathematical considerations were discussed. Two of them were selected and visualized using glyphs. To make the proposed visualizations comprehensible, two tensile bars served as simple examples.

The proposed visualization showing the stress vectors and its partial derivatives contains all information on the stress tensor and the stress gradient. But it might need some familiarization for the user to interpret the shown information. Since the stress tensor and its gradient consist of 24 independent components, this might be similar for any glyph which tries to visualize the complete information of these tensors. Thus it seems less promising to focus on glyphs that provide all the information at the same time, instead the focus should be on interaction in the future. This includes comfortable ways to select the normal direction as well as the direction of differentiation. Together with the proposed simplifications of the gradient the user should be able to investigate different properties of the gradient in an interactive way. With such a tool one might come closer to the overarching objective, i. e. finding out which information of the gradient is relevant. For the considered application this means to find out how the stress must change such that it influences the stability limit of a technical component.

5

Extremal Curves and Surfaces in Symmetric Tensor Fields

This chapter is concerned with the extraction of features characterizing the invariant part of a tensor field, i. e. the part of the tensor which is defined by the eigenvalues while the eigenvectors are ignored. As mentioned in the introduction, glyphs are able to reflect all or at least most of the tensor information at discrete points. Thus glyphs are a popular choice for the visualization of tensor fields, as we have also seen in the previous chapters. But the drawback of glyphs is that they do not allow for a continuous representation of the data. And even with advanced methods for glyph placement it is difficult to find global structures in the tensor field. If a thorough understanding of the eigenvector fields is required, then the tensor field topology might be helpful. It characterizes the global behavior of the eigenvector fields, but it does not tell much about the eigenvalues. However, for many applications the behavior of the eigenvectors is secondary, while the focus is on the analysis of quantities depending on the eigenvalues. Such quantities are invariant with respect to transformations of the local coordinate system. Important examples are the trace, the fractional anisotropy, which is widely used in diffusion tensor imaging, or the von Mises stress, which is a common yield criterion in material science, cf. Section 2.4.2. In most applications, one is interested in the maxima or the minima of such scalar invariants. However, the choice of the relevant invariants is mostly difficult.

The goal of this chapter is to overcome the restriction to a single scalar invariant. Instead we want to analyze the global behavior of the whole invariant part of the tensor field. This leads to the introduction of *extremal points* of a tensor field. The extremal points form usually curves in two dimensions and surfaces in three dimensions. This is achieved by considering a set of d invariants for a d-dimensional tensor field, see the sets of invariants considered in Section 2.3. Consequently, extremal points are features which are also invariant, they do not depend on the eigenvectors. We will see that each extremal point is the critical point of a scalar invariant. Additionally, the maxima or minima of several widely-used scalar invariants are included, not only those d invariants which are used for computation. Thus extremal points include features which are important for many applications.

Extremal points of a tensor field are defined in a mathematically rigorous way. Given a set of d invariants, an extremal point is a critical point of the map taking a point of the domain to a vector containing the d invariants. It will be shown that the same extremal points can be obtained as the critical points of maps from different meaningful and widely used systems of invariants, cf. Section 2.3. The principal invariants I, the eigenvalues λ and the K-invariants produce the same extremal points. The R-invariants also include surfaces where the trace of the tensor field is zero. However, for positive definite tensor fields such surfaces of vanishing trace do not occur, i e. equivalence holds for positive definite tensor fields.

As an immediate consequence of these equivalences, the local extrema of several widely used quantities in tensor field analysis are included in the set of extremal points. This includes the eigenvalues itself, the trace, the von Mises stress and, for positive definite tensor fields, also the fractional anisotropy. Since the degenerate points of a tensor field can be described as extrema of invariants, the extremal points also contain the degenerate points. Thus, extremal points can be considered as an extension of degenerate points in tensor field topology, but opposed to the separating curves and surfaces used in tensor field topology they characterize the behavior of invariant quantities.

As a further contribution, different ways to compute the extremal points of a tensor field numerically are discussed. Several synthetic datasets are used to illustrate the theoretical results and to show basic properties of extremal points. Moreover, the method is applied to stress tensor fields from structure simulations of different tensile bars, a specimen used for tensile testing. The resulting surfaces appear to be useful to distinguish different states of stress in the respective tensile bars.

5.1 Defintion of Extremal Points

In this section we introduce the new notion of extremal points of a tensor field. We start with the definitions of Jacobi sets and critical points, which will be used to define the extremal points of a tensor field. Let

$$g_1, \dots, g_k \ : \ \mathbb{R}^d \supset U \mapsto \mathbb{R}$$

be k differentiable functions where $k \leq d$. These functions define a map

$$g \;:\; U \to \mathbb{R}^k \;, \quad p \mapsto \begin{bmatrix} g_1(p) \\ \vdots \\ g_k(p) \end{bmatrix} \;, \tag{5.1}$$

and a point $p \in U$ is called a *critical point* if the Jacobian $Jg(p) \in \mathbb{R}^{k,d}$ at p does not define a surjective linear map from $\mathbb{R}^d$ to $\mathbb{R}^k$, cf. [DC76, p. 58]. The Jacobian Jg of g is the matrix representation of the derivative Dg of g. Note that this is different to the commonly used definition of critical points in the context of vector fields, where the zeros of the vector field are considered to be critical points. In [EH02] the *Jacobi set* for k functions $g_1, \ldots, g_k$ is defined by

$$\mathbb{J} = \{p \in U \mid \operatorname{rank} Jg(p) < k\} \;\; .$$

Consequently, the definition of the Jacobi set is equivalent to the definition of critical points.

Now we define the extremal points of a tensor field. Given is a symmetric tensor field T defined on a subset $U \subset \mathbb{R}^d$

$$T \;\; : U \to \mathbb{R}^{d,d}$$

and a set of d arbitrary tensor invariants $\{f_1, \ldots, f_d\}$, e. g. one of the sets of invariants given in Section 2.3. This defines a map

$$f \;:\; \mathbb{R}^{d,d} \to \mathbb{R}^d \;, \quad T \mapsto \begin{bmatrix} f_1(T) \\ \vdots \\ f_d(T) \end{bmatrix} \;, \tag{5.2}$$

and we assume that the map f as well as our tensor field T is continuously differentiable. Now we consider the map

$$f \circ T \;:\; U \to \mathbb{R}^d \;. \tag{5.3}$$

We call a point $p' \in U$ *extremal* with respect to the invariants f_i if and only if p' is a critical point of the map $f \circ T$, as defined above.

Since $f \circ T$ is a map from $\mathbb{R}^d$ to $\mathbb{R}^d$ the Jacobian $J(f \circ T)(p')$ is a square matrix, consequently a critical point of $f \circ T$ is given by

$$\det \left[J(f \circ T)(p') \right] = 0 \;. \tag{5.4}$$

According to the preceding paragraph, the set of extremal points can also be considered as the Jacobi set $\mathbb{J}$ of the functions $f_1 \circ T, \dots, f_d \circ T$. In general, the extremal points of a two-dimensional tensor field form curves, the extremal points of a three-dimensional tensor field form surfaces, see [EH02]. Thus we will also speak of *extremal curves* and *extremal surfaces*, respectively.

5.2 Equivalence of Extremal Curves and Surfaces w. r. t. Different Invariants

We will see in this section that for symmetric two- or three-dimensional tensor fields the three sets of invariants $\{\lambda_1, \dots, \lambda_d\}$, $\{I_1, \dots, I_d\}$, $\{K_1, \dots, K_d\}$ result in the same extremal points. For positive definite tensor fields, also the set of invariants $\{R_1, \dots, R_d\}$ produces the same extremal points. This is shown for the more difficult three-dimensional case at first, then we briefly discuss the two-dimensional case.

Three-Dimensional Case

For a three-dimensional tensor field T we assume that T has three distinct eigenvalues $\lambda_1 > \lambda_2 > \lambda_3$ at a point $p' \subset U$, i. e. p' is not a degenerate point of T. It is a well-known fact that the map taking a tensor to its eigenvalues

$$\lambda \ : \ \mathbb{R}^{3,3} \to \mathbb{R}^3$$

is differentiable in a neighborhood of nondegenerate tensors, see for example [Mag85]. Thus there is a neighborhood N of p' where the map taking p to the eigenvalues of $T(p)$ is differentiable. In accordance with equation (5.2) and (5.3) this defines a differentiable map

$$\lambda \circ T \ : \ N \to \mathbb{R}^3 \ ,$$

and the extremal points with respect to the eigenvalues λ_i are the critical points of the map $\lambda \circ T$.

Moreover, in Section 2.3 we have seen that all invariants can be expressed as functions depending on the eigenvalues. We use a bar to distinguish an invariant function $\bar{f}_i$ depending on the eigenvalues from an invariant function f_i depending on the tensor components. This defines a map

$$\bar{f} \ : \ \mathbb{R}^3 \to \mathbb{R}^3 \ , \quad (\lambda_1, \lambda_2, \lambda_3) \mapsto \begin{bmatrix} \bar{f}_1(\lambda_1, \lambda_2, \lambda_3) \\ \bar{f}_2(\lambda_1, \lambda_2, \lambda_3) \\ \bar{f}_3(\lambda_1, \lambda_2, \lambda_3) \end{bmatrix} \ ,$$

which takes the eigenvalues to the same vector of invariants as the map f in equation

(5.2) and the relation between $\bar{f}$ and f is given by

$$\bar{f} \circ \lambda = f \ . \tag{5.5}$$

Now, according to equations (5.4) and (5.5), a point p' is extremal with respect to f if and only if

$$\det \left[J(\bar{f} \circ \lambda \circ T)(p') \right] = 0 \ .$$

By the chain rule and the multiplicativity of the determinant this is equivalent to

$$\det \left[J\bar{f}(\lambda(p')) \right] \det \left[J(\lambda \circ T)(p') \right] = 0 \ .$$

Consequently, we have an extremal point with respect to the eigenvalues λ_i if and only if the second determinant vanishes. Thus we need

$$\det \left[J\bar{f}(\lambda(p')) \right] \neq 0 \tag{5.6}$$

to obtain the same extremal points from the invariants f_i and λ_i.

We want to show now, that this is true for all nondegenerate points of the tensor field T, i. e. $\lambda_1 > \lambda_2 > \lambda_3$, in case of the I-invariants and the K-invariants. For the R-invariants we have to make the additional assumption that the tensor field is positive definite, i. e. $\lambda_1 > \lambda_2 > \lambda_3 > 0$. The Jacobians of $\bar{I}$, $\bar{K}$ and $\bar{R}$ can be obtained by straightforward computations, the resulting Jacobians are given in Appendix A.1. Here we just state the resulting determinants. The determinant of $J\bar{I}$ is

$$\det \left[J\bar{I}(\lambda_1, \lambda_2, \lambda_3) \right] = (\lambda_1 - \lambda_2)(\lambda_1 - \lambda_3)(\lambda_2 - \lambda_3) \tag{5.7}$$

and the determinant of $J\bar{K}$ is given by

$$\begin{aligned} &\det \left[J\bar{K}(\lambda_1, \lambda_2, \lambda_3) \right] = \\ &= 3\sqrt{6} \|\tilde{T}\|^{-4} (\lambda_1 - \lambda_2)(\lambda_2 - \lambda_3)(\lambda_3 - \lambda_1) \ . \end{aligned} \tag{5.8}$$

This shows that the determinant of $J\bar{I}$ and $J\bar{K}$ is zero if and only if two eigenvalues are equal, i. e. for a degenerate tensor. For the determinant of $J\bar{R}$ we obtain

$$\begin{aligned} \det \left[J\bar{R}(\lambda_1, \lambda_2, \lambda_3) \right] &= 3\|T\|^{-2} \|\tilde{T}\|^{-4} \\ &(\lambda_1 - \lambda_2)(\lambda_2 - \lambda_3)(\lambda_3 - \lambda_1)(\lambda_1 + \lambda_2 + \lambda_3) \ . \end{aligned} \tag{5.9}$$

Consequently, $\det J\bar{R}$ is nonzero if there are no equal eigenvalues and if the trace is nonzero. Especially, this is true for all nondegenerate points of positive definite tensor fields.

Now, for the nondegenerate points of the tensor field, we have shown the equivalence of extremal surfaces for different sets of invariants. In case of degenerate points, the definition of extremal surfaces is strictly speaking not applicable for the eigenvalues, since the map λ is not differentiable here. However, at a degenerate point there is an eigenvalue which has an extremum, thus it makes sense to consider degenerate points also as extremal. For the other sets of invariants the determinant of the Jacobian becomes zero at a degenerate point. In this way, the equivalence of the extremal surfaces is also established at degenerate points.

Two-Dimensional Case

The equivalence of extremal curves of two-dimensional tensor fields with respect to different sets of invariants can be shown in the same way as for three-dimensional tensor fields. In this case the determinants of $J\bar{I}, J\bar{K}, J\bar{R}$ are given by

$$\det\left[J\bar{I}(\lambda_1,\lambda_2)\right] = (\lambda_1-\lambda_2)\ ,$$

$$\det\left[J\bar{K}(\lambda_1,\lambda_2)\right] = -\|\tilde{T}\|^{-1}(\lambda_1-\lambda_2)\ ,$$

$$\det\left[J\bar{R}(\lambda_1,\lambda_2)\right] = -\sqrt{2}\|T\|^{-2}\|\tilde{T}\|^{-1}(\lambda_1-\lambda_2)(\lambda_1+\lambda_2)\ .$$

This implies the equivalence of the extremal curves with respect to the λ-, I- and K-invariants, and the additional equivalence with respect to the R-invariants if the trace of T is nonzero.

5.3 Interpretation of Extremal Points

We discuss different properties and interpretations of extremal points in this section. This includes the important property that the extremal points contain the extrema of several widely used invariants, and that each extremal point is an extremum or saddle of a certain scalar invariant.

In the preceding section we have seen that the extremal points produced by the I- and the K-invariants, and for positive definite tensors also the R-invariants, produce the same extremal points as the eigenvalues. This shows that the extremal points with respect to any of these invariants are inherent with the tensor field, they are not properties of the specific set of invariants. It is easy to see that this is not true for an arbitrary set of invariants. For example, if we consider extremal surfaces with respect to the R-invariants for a tensor field which is not positive definite, then equation (5.9) shows that also the surfaces where the trace vanishes are included. On the other hand, it is easy to construct further sets of invariants which produce the same extremal surfaces. For each map $f : \mathbb{R}^3 \to \mathbb{R}^3$ with nonvanishing determinant of the Jacobian Jf equation (5.6) is fulfilled. This is true for each diffeomorphism on $\mathbb{R}^3$.

Although these equivalences might seem to make other sets of invariants than the eigenvalues redundant, they bring two major benefits. First, we can freely choose the set of invariants used for the computation. We will discuss this issue in Section 5.6. Secondly, this allows for a much stronger interpretation of the resulting surfaces. Each critical point p' of a single invariant of the tensor field $f_i \circ T$, i. e.

$$\nabla(f_i \circ T)(p') = 0 \ ,$$

results in a critical point of $f \circ T$. So we have that the extremal surfaces contain the critical points, i. e. an extremum or a saddle, of a numerous number of widely-used tensor invariants. This includes trace, norm, von Mises stress, determinant and eigenvalues. In case of diffusion tensors, which are positive definite, we can also add the fractional anisotropy, a quantity that is widely-used in this context. Additionally, as mentioned above, the mode ensures that also degenerate points of the tensor field are included.

Moreover, each point of an extremal surface is a critical point of some invariant function. Equation (5.4) implies that at a critical point p' we can choose $\alpha_1, \alpha_2, \alpha_3 \in \mathbb{R}$ such that

$$\begin{aligned} 0 &= \alpha_1 \nabla(f_1 \circ T)(p') + \alpha_2 \nabla(f_2 \circ T)(p') + \alpha_3 \nabla(f_3 \circ T)(p') \\ &= \nabla\left((\alpha_1 f_1 + \alpha_2 f_2 + \alpha_3 f_3) \circ T\right)(p') \ . \end{aligned}$$

Thus the invariant function $\alpha_1 f_1 + \alpha_2 f_2 + \alpha_3 f_3$ has a critical point at p'. Conversely, all critical points of linear combinations of the invariants f_1, f_2, f_3 are contained in the extremal surfaces.

Similarly, we can consider the transposed problem. We have an extremal point p' if and only if there is a direction $v \in \mathbb{R}^3$ such that

$$\begin{aligned} 0 &= v_1 \partial_1(f \circ T)(p') + v_2 \partial_2(f \circ T)(p') + v_3 \partial_3(f \circ T)(p') \\ &= \partial_v (f \circ T)(p') \ , \end{aligned}$$

i. e. the directional derivative of f in direction v is zero. This means that the directional derivatives of all single invariants f_i vanish in direction v. Consequently, there is a line passing through each extremal point p' such that the restriction of each f_i to this line has a critical point at p', and vice versa. If these critical points are produced by minima or maxima, then extremal points correspond to points where the image of the tensor field under f is folded. Thus we speak of extremal points.

We give a geometric interpretation of the findings above using continuous scatter plots. Continuous scatter plots were proposed by Bachthaler et al. in [BW08]. A continuous scatter plot visualizes a map $g : \mathbb{R}^d \to \mathbb{R}^k$, where $\mathbb{R}^d$ is called the spatial domain and $\mathbb{R}^k$ the data domain. The continuous scatter plot is now a density function

$$\psi : \mathbb{R}^k \to \mathbb{R}$$

defined on the data domain, which assigns to each point the frequency that this point occurs in the data. In case of $k = 2$ the density function ψ allows for an easy visualization, so we can use continuous scatter plots to visualize the map $f \circ T$ for the map f defined by a set of invariants and a two dimensional tensor field T.

As an example we consider the linear tensor field given by

$$[-1,1]^2 \to \mathbb{R}^{2,2} \ , \quad p \mapsto \begin{bmatrix} p_1 & p_1 \\ p_1 & 1 - \frac{p_2}{2} \end{bmatrix} \ . \tag{5.10}$$

Figure 5.1 shows the extremal curves and the continuous scatter plot of this field for different sets of invariants. Easy computations show that the extremal curves of a linear tensor field are straight lines. As shown above, the extremal lines are the same for the λ-, I-, and K-invariants. For the R-invariants we obtain an additional line where the trace of the field is zero. The continuous scatter plots show how the spatial domain of the tensor field is mapped to the space of invariants, that is our data domain. The horizontal axis corresponds to the first invariant, while the vertical axis corresponds the second invariant. The red curves in the space of invariants show where the image of the tensor field is folded. The preimage of these curves are the extremal curves of the tensor field. They are (locally) the extremal points in the space of invariants, that is why we call these curves extremal. Note that the continuous scatter plots for the λ-, I-, and K-invariants look very different, so it is not obvious that the extremal points for these invariants are the same.

5.4 Implementation

The newly defined extremal points demand for new methods to compute them. We assume given triangular or tetrahedral meshes with the values of the invariants given at the vertices. As mentioned above, the computation of the extremal surfaces is equivalent to the computation of Jacobi sets. This allows to use methods for computing Jacobi sets, however, stable methods are still subject of research. A discrete method for the computation of Jacobi sets was proposed by Edelsbrunner et al. in [EH02]. This method extracts the faces of the mesh which belong to the Jacobi set. Unfortunately, this method is very sensitive to noise, the resulting Jacobi sets tend to be very complex. There are methods to simplify Jacobi sets of two functions, see [BWN$^+$15] and [SN11]. We briefly discuss the discrete method presented in [EH02] in this section. As an alternative, we propose an approach by

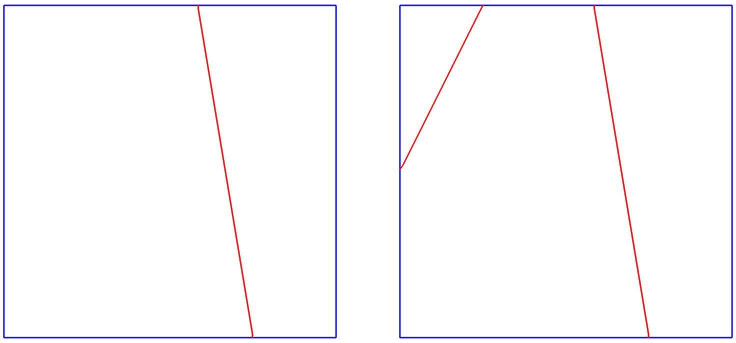

(a) *λ, I- or K-invariants* **(b)** *R-invariants*

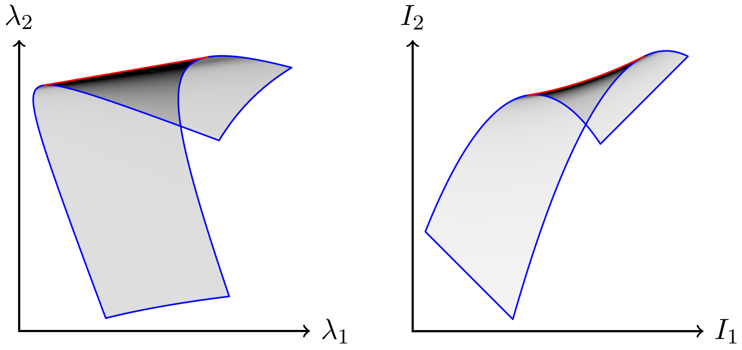

(c) *λ-invariants* **(d)** *I-invariants*

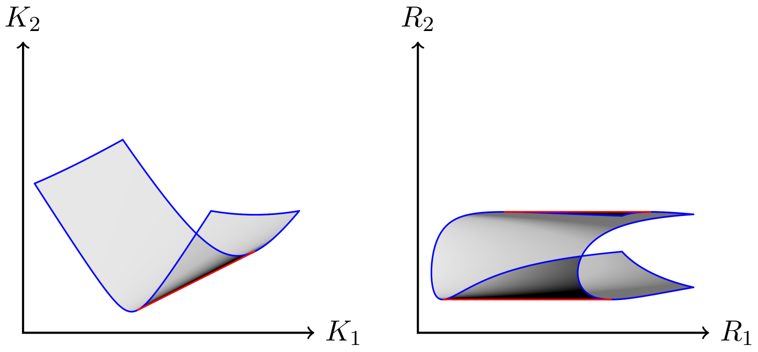

(e) *K-invariants* **(f)** *R-invariants*

Figure 5.1: *Figures (a) and (b) show the critical curves for the linear tensor field given by equation (5.10). Figures (c) to (f) show the corresponding continuous scatter plots for different sets of invariants.*

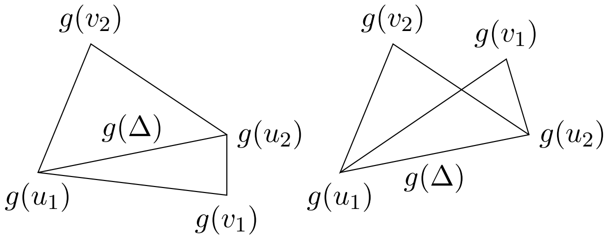

Figure 5.2: *Example of two triangles mapped in the data domain. If $g(v_1)$ and $g(v_2)$ are on different sides of the edge $g(\Delta)$, then Δ is not an extremal edge (left), otherwise it is (right).*

approximating the determinant of the Jacobian at the vertices of the mesh and use the marching cubes algorithm in order to extract the curves or surfaces where the determinant vanishes.

In [EH02] a method is proposed to compute the Jacobi set for k functions $g_1, \ldots, g_k$ which are defined on the vertices of a triangulated d-dimensional mesh. We are only interested in the case $k = d$, in this case the algorithm works in the following way: Let Δ be a $d-1$-simplex, i. e. an edge in case of a triangular mesh or a triangle in case of a tetrahedral mesh, and $u_1, \ldots, u_d$ the vertices of Δ. Consider the function

$$h = g_j + \sum_{i \neq j} \alpha_i g_i$$

while the α_i are chosen such that

$$h(u_1) = \ldots = h(u_d) \ .$$

If the $d-1$-simplex Δ does not belong to the boundary of the mesh, then there are two neighboring d-simplices contained in the mesh. Let v_1 and v_2 be the vertices of these d-simplices, which do not belong to Δ. Then Δ belongs to the Jacobi set if and only if

$$h(v_i) < h(u_1) \qquad \text{or} \qquad h(v_i) > h(u_1) \ , \quad i = 1, 2 \ . \tag{5.11}$$

This condition gives a nice interpretation for a simplex to be extremal in our sense. Consider the image $g(\Delta)$ of the simplex Δ under the map g given in equation 5.1, i. e. we consider the image of Δ in the data domain. The vertices $g(u_1), \ldots, g(u_d)$ span a $d-1$-dimensional hyperplane. Now simple computations show that equation (5.11) holds if and only if $g(v_1)$ and $g(v_2)$ are on the same side of this hyperplane. In this case the mesh is folded at the simplex Δ, an illustration is given in Figure 5.2.

An alternative approach computing the extremal points is to compute the determinant of the Jacobian Jg of the map g. For a triangulated mesh we can compute $\det[Jg]$ directly for each d-simplex Δ by

$$\frac{\mathrm{vol}(g(\Delta))}{\mathrm{vol}(\Delta)} \;,$$

where vol denotes the volume of a simplex. This is equivalent to the determinant of the Jacobian for the linear interpolated field on Δ and yields a scalar field defined on the d-simplices of the mesh. Note that the $d-1$-simplices of the mesh, which are adjacent to two d-simplices where the sign of the determinant changes, are exactly the $d-1$-simplices of the Jacobi set computed by the method described above. In order to get smoother curves we map the scalar field defined on the simplices to a scalar field defined on the vertices. We assign to each vertex the average over the values on the d-simplices which are adjacent to this vertex. Then we obtain a continuous scalar field by linear interpolation which allows us to extract the extremal curves or surfaces by using a marching cubes method.

A similar approach is to approximate the Jacobian at each vertex and compute the determinant of the resulting Jacobian. To obtain the Jacobian at each vertex we compute the Jacobian of the linear interpolated map g for all adjacent d-simplices and take the average of the resulting matrices. The difference to the approach described above is that we average the Jacobian matrices and compute the determinant afterwards, instead of computing the determinant of the Jacobian for each d-simplex and averaging the resulting determinants.

We study results of the different methods and the effect of noise in Figure 5.3. The left column shows the results for the linear field given in equation (5.10), while the domain is uniformly sampled with 100×100 points and triangulated. Additional Gaussian noise with a standard deviation of 0.001 and 0.003 is added for the results in the middle and the right columns. The top and middle rows show the results using marching cubes. In the top row the Jacobian is approximated and the determinant is computed afterwards, in the middle row the determinant of the Jacobian is approximated directly, see above. The methods using marching cubes (top and middle row) produce very similar results and allow for the extraction of smooth lines. In contrast, the discrete approach for computing Jacobi sets (bottom row) is restricted to the edges of the mesh. All methods are sensitive to noise, but the effect is much stronger for the discrete approach.

5.5 Results

In this section several results are discussed. This includes linear tensor fields which will demonstrate basic properties of extremal surfaces, as well as the findings of Sec-

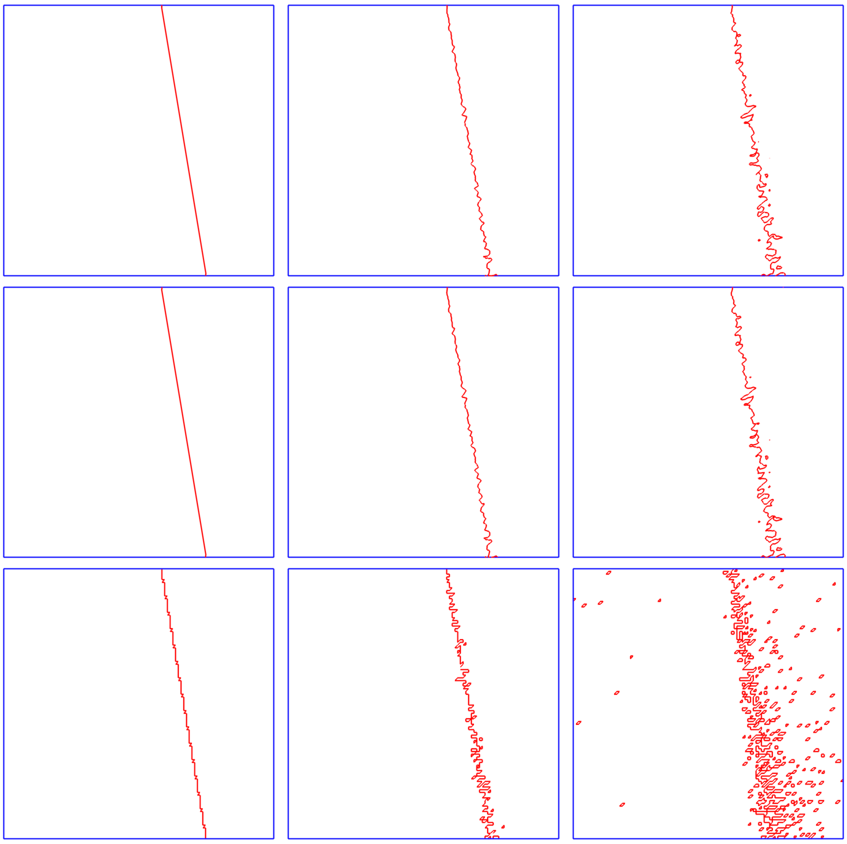

Figure 5.3: *Comparison of the different methods for computing the extremal curves of a linear tensor field with increasing noise from left to right. In the top row a finite difference approach is used to compute the Jacobian first, then the marching cube method is applied on its determinant. In the middle row the determinant of the Jacobian is computed directly for each simplex, then the marching cube method is used. The bottom row shows the discrete approach for computing the Jacobi sets.*

tion 5.2. Further synthetic examples demonstrate the connection between extremal points and degenerate points. Moreover results for the double point load example are given, which is a well studied benchmark dataset in tensor field visualization. We will also consider simulated stress tensor fields of different tensile bars. These are specimens used to perform tensile testing in order to analyze material properties.

The extremal surfaces are computed in the following way: First, the three considered invariant functions f_1, f_2, f_3 of the tensor field are computed. In this way we obtain the map $f \circ T$, compare equation (5.2) and (5.3). Now the extremal surfaces are computed as described in the previous section by setting $g = f \circ T$. Since the discrete approach is very sensitive to noise, it is preferable to approximate the Jacobian matrix $J(f \circ T)$ for each vertex and use the marching cubes method to compute the surfaces where the determinant of the Jacobian vanishes. By equation (5.4) these are the points where the tensor field is extremal.

Linear Tensor Fields

As a first simple test case we consider two randomly chosen affine linear tensor fields, see Figure 5.4. The fields are given by

$$\begin{aligned} T \ : \ & [-1,1]^3 \to \mathbb{R}^{3,3} \ , \\ & p \mapsto T^{(0)} + p_1 T^{(1)} + p_2 T^{(2)} + p_3 T^{(3)} \end{aligned}$$

with $T^{(0)}, \ldots, T^{(3)} \in R^{3,3}$. The components of $T^{(0)}, \ldots, T^{(3)}$ are chosen randomly in the interval $[-1, 1]$.

The extremal surfaces are computed once with the λ-invariants (green), I-invariants (red), K-invariants (blue) and R-invariants (yellow). The resulting surfaces demonstrate what has been shown in Section 5.2. In case of the λ-, I- and K-invariants we obtain exactly the same result. For the R-invariants there is an additional surface in the lower row of Figure 5.4. As expected, this is the surface where the trace vanishes, which is a plane for a linear tensor field. The dataset used in the upper row of Figure 5.4 does not contain tensors of trace zero in the considered domain, thus all invariants yield the same result. The yellow lines are the degenerate lines of the tensor field, as expected they lie on the surfaces.

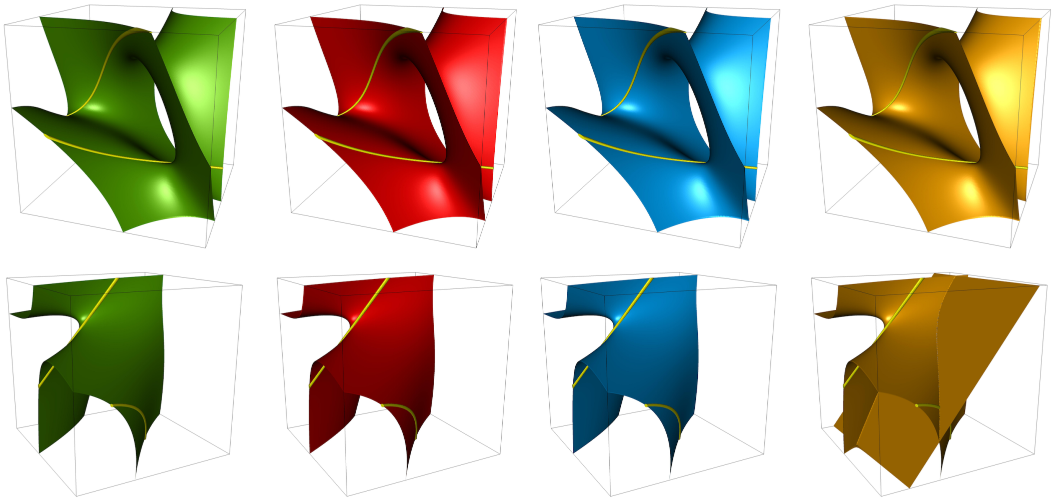

(a) *λ-invariants* **(b)** *I-invariants* **(c)** *K-invariants* **(d)** *R-invariants*

Figure 5.4: *Extremal surfaces of two randomly produced linear tensor field computed by different sets of invariants. No surface of trace zero is contained in the upper row, thus all results are the same. In the lower row there is a plane where the trace is zero, this plane is included when the R-invariants are used.*

Eigenvalues Defined by Quadratic Functions

For the next example three simple quadratic functions $q_1, q_2, q_3 : \mathbb{R}^3 \to \mathbb{R}$ are considered, for $p \in \mathbb{R}^3$ they are given by

$$\begin{aligned} q_1(p) &= (p_1 - 0.5)^2 + p_2^2 - p_3^2 \ , \\ q_2(p) &= p_1^2 - (p_2 - 0.3)^2 - p_3^2 \ , \\ q_3(p) &= p_1^2 + p_2^2 + p_3^2 \ . \end{aligned}$$

Now we define the tensor field

$$T \ : \ [-1,1]^3 \to \mathbb{R}^{3,3} \ , \quad p \mapsto \begin{bmatrix} q_1(p) & & \\ & q_2(p) & \\ & & q_3(p) \end{bmatrix} \ .$$

Consequently, the quadratic functions q_i are the eigenvalues of T. The resulting extremal surfaces of T are shown in Figure 5.5a, the results are computed using the I-invariants.

Note that the extremal surfaces of T are not equivalent to the critical points of

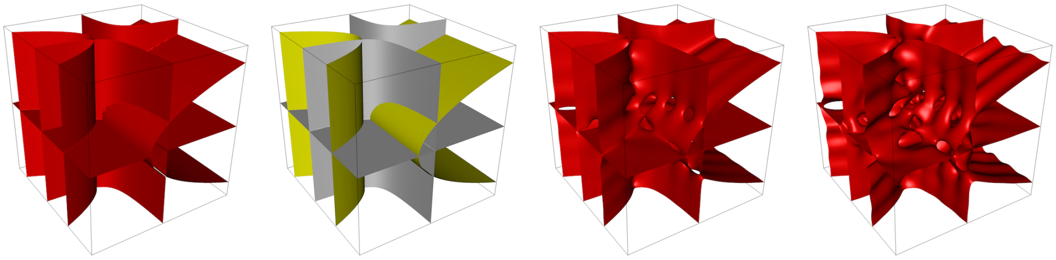

(a) (b) (c) (d)

Figure 5.5: *Extremal surfaces for an analytic tensor field given by quadratic functions on the diagonal. Figure (b) shows the degenerate surfaces in yellow and remaining critical surfaces in gray. Figures (c) and (d) show results with perturbed off-diagonal elements.*

the map q defined by

$$q \quad : \quad [-1,1]^3 \to \mathbb{R}^{3,3} \quad , \quad p \mapsto \begin{bmatrix} q_1(p) \\ q_2(p) \\ q_3(p) \end{bmatrix} \quad .$$

Of course, the critical points of q are also extremal surfaces of T. But in addition, points, where two of the functions q_i are equal, are contained in the extremal surfaces of T. These are the degenerate points of the tensor field T. We have also computed these two kinds of surfaces separately. The gray surfaces in Figure 5.5b are the critical points of q, the surfaces, where two of the q_i are equal, are shown in yellow.

Note that such fields with three given smooth functions for the eigenvalues are unusual in practice. Degenerate surfaces are not stable under small perturbations of the tensor values, see [ZP04] for details. However, considered as extremal surfaces, the yellow surfaces in Figure 5.5b do not disappear under small perturbations. Figures 5.5c and 5.5d show results with a smaller and a stronger perturbation of the off-diagonal elements, respectively. We can see here that all surfaces are deformed under the perturbation. But the formerly degenerate surface is still existent, although it is not a degenerate surface anymore.

Double Point Load

Next we consider the well-known double point load example. The stresses in the interior of a soil mass, caused by a vertical point load applied at the ground surface, can be computed analytically by using the Boussinesq equation, see [SD03]. The load is applied on a half-space bounded on the top by an infinite horizontal plane. By superposition of two point loads we obtain the double point load dataset considered

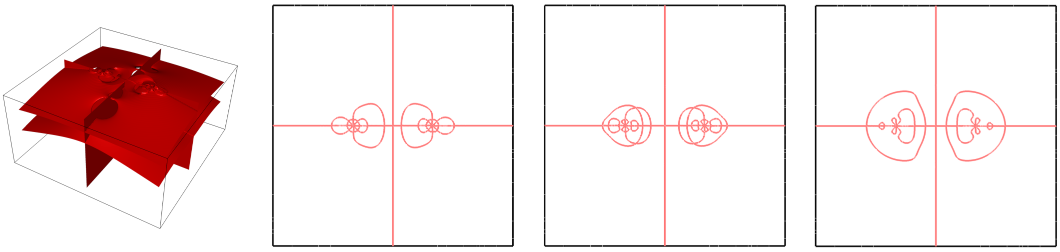

(a) *3D view* **(b)** $z = 0.01$ **(c)** $z = 0.03$ **(d)** $z = 0.05$

Figure 5.6: *Extremal surfaces of a double point load in three dimensions, and three slices at different depth* z*. The extremal surfaces show a rich structure close to the load points.*

in Figure 5.6. The horizontal plane ranges from -1 to 1 here, while the depth ranges from 0.01 to 1. The point loads are located with a distance of 1/3 from the origin.

Due to the occlusion of the extremal surfaces given in Figure 5.6a we also show slices of the extremal surfaces. The slices are parallel to the ground surface at different depths of 0.01, 0.03 and 0.05, see Figure 5.6b, 5.6c, 5.6d. This example shows that extremal points are suitable to hint at the interesting regions of a tensor field. Close to the load points the extremal surfaces have a rich structure. More distant from the load points there are only two horizontal surfaces, see Figure 5.6a, as well as the planes of symmetry in the dataset. Planes of symmetry are always extremal surfaces. If we consider a line orthogonal to a plane of symmetry then each of the three single invariants must have a local minimum or a maximum at the point where the line intersects the plane. This is a sufficient condition for an extremal point as discussed in Section 5.3. Since we want to use extremal surfaces to analyze the global structure of tensor fields, it makes sense to have planes of symmetry included.

Tensile Bar Datasets

As in Chapter 4, we consider simulated stress tensors of different tensile bars. The datasets were created by Prof. Dr. Markus Stommel and Jannik Nahrgang from the Chair for Plastics Technology at TU Dortmund University by using the commercial software package ABAQUS. Here we consider additional tensile bars with differently curved notches, as well as tensile bars with notches in the center, see Figure 5.7. These notches serve for the purpose of causing different stressing conditions on a quite simple specimen.

For the computation of the extremal surfaces we use again the I-invariants. The result for the tensile bar with the circular notch on the side is shown in Figure 5.8. We observe that there is a plane separating the narrow side in the middle. This is again

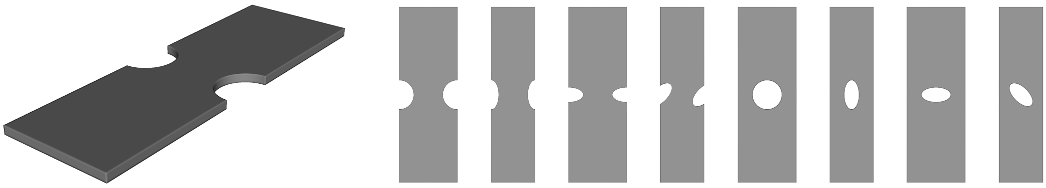

Figure 5.7: *Geometry of tensile bars with differently curved notches. For the first four bars the notches are placed on the side, for the second four in the center. A 3D view of the first one is shown on the left.*

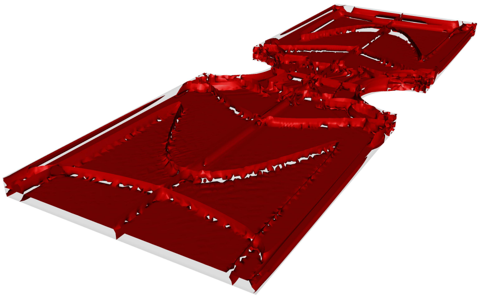

Figure 5.8: *Extremal surfaces of the tensile bar with circular notch on the side. Since we have a symmetric state of stress, there are extremal surfaces on all planes of symmetry.*

a plane of symmetry in the dataset. The remaining surfaces are nearly orthogonal to this plane of symmetry, which makes it reasonable to consider any two-dimensional slice of the result, since the different slices show very similar structures.

Slices of the extremal surfaces of the tensile bar are shown in Figure 5.9. For the symmetric datasets with notches on the side in Figures 5.9a, 5.9b, 5.9c and the symmetric datasets with notches in the center in Figures 5.9e, 5.9f, 5.9g, the planes of symmetry are again contained in the extremal surfaces. Moreover, the extremal surfaces of the symmetric datasets with different notches on the side form a similar pattern, indicating a similar state of stress in all three cases. The same holds for the three tensile bars with notches in the center. In case of the asymmetric tensile bars in Figures 5.9d and 5.9h there are no planes of symmetry. Also the structure differs significantly from the other results. This indicates a different state of stress. For the asymmetric tensile bar with the notch in the center we observe some noise, see Figure 5.9h. This indicates a volume of extremal points. We discuss this issue in the next section.

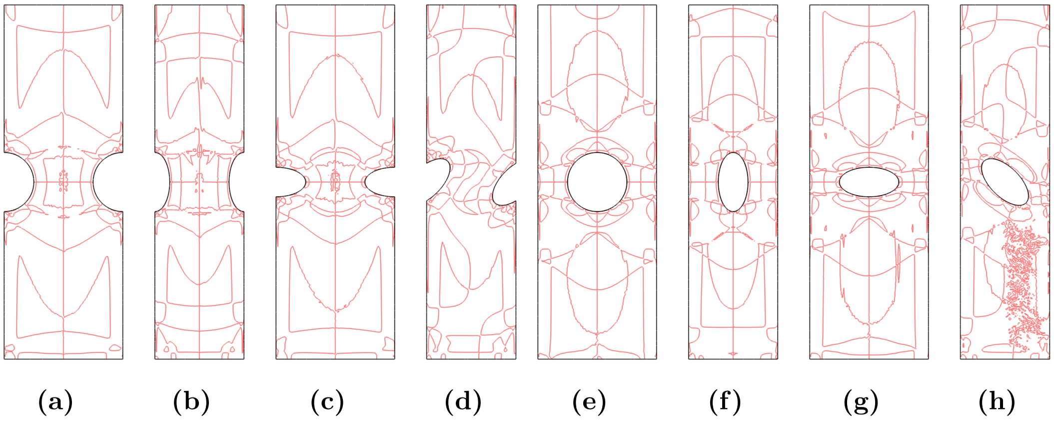

Figure 5.9: *A slice of the extremal surfaces for different tensile bars. The patterns allow to identify similar stressing conditions for the tensile bars (a), (b), (c) and (e), (f), (g), respectively.*

5.6 Discussion

The applicability of extremal surfaces was demonstrated in the preceding section. Nonetheless, there are some things to consider when computing the extremal surfaces and some difficulties which can occur. We will discuss these issues in this section.

First of all, there are volumes of extremal points as encountered in Figure 5.9h. Of course, this is a degenerate case, but it is not impossible in practice. For example, it might occur that there is a region where two invariant functions grow simultaneously, i. e. their gradients are parallel. Or it might happen that one invariant is almost constant. In such cases, we obtain volumes of extremal points. Consequently, there are strategies needed to treat such regions.

A second issue is that we lack stable methods for the numerical computation of the extremal surfaces. In theory the λ, I- and K-invariants produce the same extremal surfaces. In practice there may be deviations for numerical reasons. Thus, we need to ensure that we choose a set of invariants which produces reliable results. According to our observations, the I-invariants yield the best results. This is not surprising as the I-invariants are the easiest to compute, only elementary arithmetic is necessary. We obtain similar results if the eigenvalues are used as invariants, but the surfaces are not as smooth as for the I-invariants. On the one hand, this might be a consequence of the fact that the eigenvalues do not form smooth functions in general. If we try to differentiate them numerically, this may cause problems. On the other hand, the computation of the eigenvalues is a quite complex numerical method, compared to the simple computations needed to obtain the I-invariants. Thus smaller errors in the result are expectable. For the K-invariants, the extremal

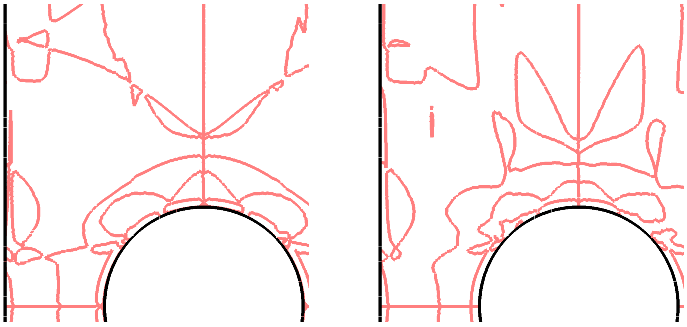

Figure 5.10: *Comparison of the extremal surfaces for the tensile bar with the circular notch in the center. The results are computed with the I-invariants (left) and the K-invariants (right).*

surfaces show rather large deviations. In Figure 5.10, a comparison of the results for the I- and the K-invariants is shown. Presumably, this is a negative effect of the additional factor $3\sqrt{6}/\|\tilde{T}\|$ in the expression of the determinant of $J\bar{K}$ compared to the determinant of $J\bar{I}$, see equation 5.7 and 5.8, respectively. For the same reason, we obtain similar results if we use the R-invariants instead of the K-invariants.

Having chosen a proper set of invariants, the computation of the extremal surfaces is still challenging. As mentioned above, the computation of the Jacobi sets is still subject to research and is very sensitive to noise. Irrespective of noise, we obtain many extremal surfaces for complex data. Thus there is a demand for simplification strategies in order to analyze complex data. To the best of our knowledge, all simplification strategies deal with Jacobi sets of two functions which are not suitable for the extraction of extremal surfaces of three-dimensional tensor fields.

For the examples discussed here it was possible to reduce the effect of noise by extracting the extremal surfaces from the determinant of the Jacobian. However, using the marching cubes algorithm produces some artifacts. If there are extremal surfaces which intersect, then there occur gaps, see Figure 5.8. Such intersections are caused by critical points of the scalar function defined by the determinant. At least in the examples considered here, this happens frequently when extracting extremal surfaces, so there might be a demand for methods treating these intersections. Moreover, the value of the determinant is interpolated linearly within each tetrahedron, although a more precise computation would be possible. This linear interpolation can only produce a single plane within each tetrahedron. The linear datasets shown in Figure 5.4 demonstrate that much more complex surfaces are possible within a single tetrahedron. Especially for data with lower resolutions the mentioned limitations of a plain marching cubes method become apparent.

For the moment, it is not possible to give a precise physical interpretation for all extremal curves and surfaces occurring in the tensor fields. The interpretation of a tensor is generally highly dependent on the respective application. But there are a huge number of applications where mostly the invariant part of the tensor is studied and especially extrema of certain tensor invariants are relevant. Examples are several yield criteria for isotropic materials like the von Mises stress, the maximum principal stress or the maximum shear stress, as well as the trace and the fractional anisotropy, which are studied in diffusion tensor imaging. It was shown that the extremal points of the tensor field contain the extrema of many widely-used invariants. And many more invariants might have this property, unless they introduce additional extrema like the fractional anisotropy which has a minimum for traceless tensors. Consequently, for applications where extrema of invariants of the tensor are important, it is not necessary to consider the whole data. It is possible to reduce analysis to extremal points, since the extremal points include all possibly interesting parts of the field. This restricts analysis to a lower dimensional subset of the data. Moreover, the extremal points also serve as a characterization of the invariant part of the tensor field, similarly as the tensor field topology characterizes the behavior of the eigenvector fields. The detection of planes of symmetry serves as an example for this property.

5.7 Conclusion

The notion of extremal points for tensor fields was introduced in this chapter. The main contribution is the shown property that different widely-used sets of invariants produce the same extremal curves or surfaces. In case of the eigenvalues, this shows that extremal surfaces are inherent to the field. They are not properties of the respective invariants. The I-invariants allow for an numerically robust computation. The equivalence to the extremal points with respect to K- and R-invariants (in the latter case only for positive definite tensor fields) shows that the extrema of additional widely used invariants are contained in the set of extremal points. This makes extremal curves and surfaces promising in different applications. Moreover, we have proposed different ways for the computation of the extremal points and discussed their properties.

Synthetic datasets were used as simple examples which demonstrate basic properties of extremal points, this includes linear tensor fields as well as a double point load dataset. Simulated stress tensor fields for different tensile bars are used as first examples of realistic datasets. The patterns produced by the extremal surfaces make it possible to detect similar states of stress in different datasets, as well as fundamental differences.

This makes extremal points a promising tool for the analysis of tensor fields. There are very few methods which analyze the global structure of a tensor field. The most prominent example, the tensor field topology, is very difficult to compute if separating surfaces are included. Moreover, the tensor field topology largely neglects the invariant part of the tensor field, only points where two eigenvalues are equal are detected. But the invariant part of the tensor field is crucial in most applications. Thus analyzing the global structure of the invariant part is important to detect the interesting regions of the field. Extremal points can offer interesting possibilities in this direction. In many cases it might be even sufficient to restrict analysis to the extremal curves or surfaces of the tensor field, since they include all relevant features of the field.

6

Visualization of Two-Dimensional Symmetric Tensor Fields Using the Heat Kernel Signature

The Heat Kernel Signature (HKS) is a a powerful shape signature and has been introduced by Sun et al. in [SOG09]. They have shown that the HKS is an isometric invariant and contains almost all intrinsic information of a surface. Thus it is well suited for detecting similar shaped regions of surfaces. The HKS is derived from the process of heat diffusion and consequenlty equipped with a time parameter. This multiscale property allows to adjust the size of the neighborhood that influences the value of the HKS at a point. Additionally, the HKS is not sensitive to small perturbations of the underlying surface, e. g. a tunnel between small sets of points. Several methods employ the HKS to detect similar shaped surfaces globally, see [OBBG09] [BK10] [DLL$^+$10] [RBBK10]. Also from a visual point of view the HKS characterizes a surface very well, since, for small time values, it is closely related to the Gaussian curvature of the surface. For large time values it can be considered as the curvature on a larger scale. Motivated by these useful properties, the HKS is proposed for the visualization of tensor fields in this chapter. The basic idea is to consider a positive definite tensor field as Riemannian metric, i. e. together with its domain the tensor field forms a Riemannian manifold. In this way the definition of the HKS is also applicable for positive definite tensor fields. Loosely speaking, we obtain a scalable Gaussian curvature of the tensor field.

The relation between the HKS of a two dimensional surface M and a positive definite tensor field (i. e. the metric tensor field of the surface) is illustrated in Figure 6.1. If g is the metric of the surface M and $f : \mathbb{R}^2 \supset U \mapsto \mathbb{R}^3$ a parametrization

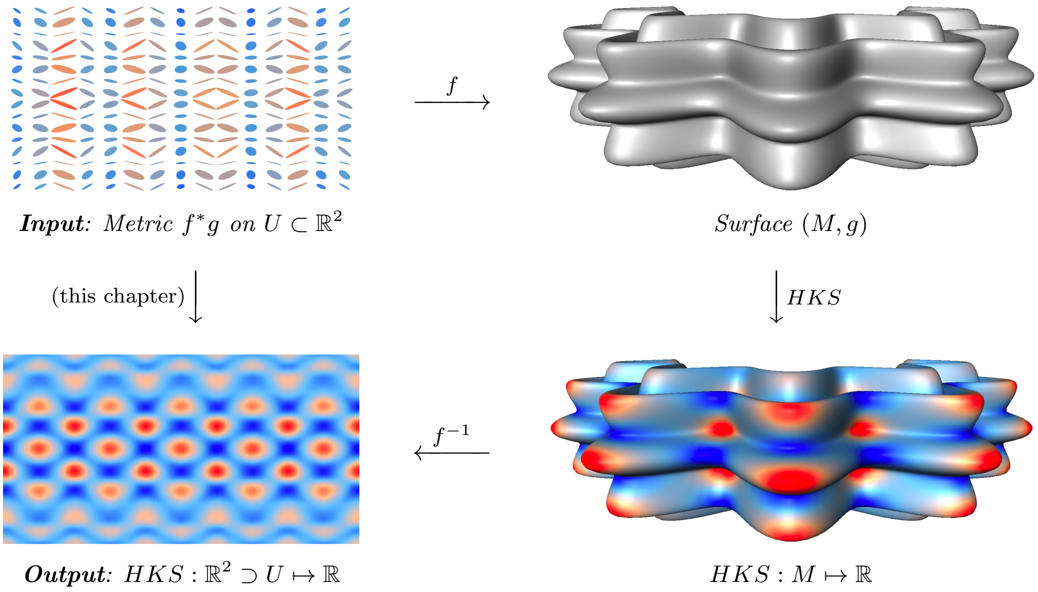

Figure 6.1: *Commutative diagram illustrating the relation between the HKS of a surface and a positive definite tensor field. The metric of the surface depicted as ellipses (top left), the parametrized surface (top right), the HKS on the surface (bottom right) and the HKS on U (bottom right).*

of M, i. e. $f(U) = M$, then we can compute the pull back of the metric g on U by f, denoted by f^*g. The metric f^*g is a positive definite tensor field on U which is well characterized by the HKS of the surface. We can thereby compute the HKS for a positive definite tensor field defined on $U \subset \mathbb{R}^2$, by interpreting the tensor field as the metric of a surface.

In this chapter, a method is proposed which allows to compute the HKS directly for a positive definite tensor field defined on $U \subset \mathbb{R}^2$, the tensor field is interpreted as the metric of a surface. But it is not necessary to compute an explicit embedding of the associated surface into some Euclidean space to compute the HKS of a given tensor field. This results in a significant difference for the computation of the HKS. While in case of surfaces the embedding is utilized to compute the HKS, in the case of general tensor fields all computations can be done using the tensor only. To do this efficiently, a finite element method is employed, see Section 6.3.

The method is restricted to two-dimensional tensor fields in this chapter, but the definition of the HKS and the numerical realization presented here is also valid in higher dimensions. However, the computational complexity will be a problem in higher dimensions, see also the remark in Section 6.5. Moreover, the HKS is only defined for positive definite tensor fields. For other tensor fields, e.g. stress tensor fields, this method is not directly applicable. Thus the interpretation of such tensor fields as a generator of a time dependent deformation via a positive monotonic mapping is suggested. So we obtain a field which describes a process close to a diffusion process, see [HFH+04]. This enables us to analyze these fields using the HKS.

Section 6.1 gives a short introduction to the HKS. The application of the HKS to tensor fields is explained in Section 6.2. To compute the HKS we need to compute the eigenvalues of a the Laplacian on a Riemannian manifold (M, g). In case of surfaces the embedding in the Euclidean space can be utilized, whereas, in the case of tensor fields, all computations must be done by using the tensor only. A finite element method to achieve this for tensor fields is proposed in Section 6.3, alongside with some numerical tests. Experiments and results of the method are shown in Section 6.4.

6.1 Heat Kernel Signature

The Heat Kernel Signature (HKS) is typically used for the comparison of surfaces. It is derived from the heat equation and assigns each point of the surface a time dependent function $[0, \infty) \to \mathbb{R}$ which depends only on the metric of the surface. Conversely, all information about the metric are contained in the HKS under quite weak assumptions. For smaller time values the HKS at a point is governed by smaller neighborhoods, i. e. one can control the portion of surface which should be taken into account. This makes the HKS a powerful tool for the identification of similar shaped parts with different level of detail by comparing the HKS for different time values. However, the HKS is not restricted to surfaces, it is defined for arbitrary Riemannian manifolds. We employ this fact to apply the HKS on positive definite tensor fields. A short introduction to the HKS is given in this section, for details see [SOG09]. A detailed treatment of the heat operator and the heat kernel can be found in [Ros97].

Let (M, g) be a compact, oriented Riemannian manifold and Δ the Laplace-Beltrami operator (also called just Laplacian) on M, which is equivalent to the usual Laplacian in case of flat spaces. Given an initial heat distribution

$$h(p) = h(0, p) \in C^\infty(M)$$

on M, considered to be perfectly insulated, the heat distribution

$$h(t, p) \in C^\infty(\mathbb{R}^+ \times M)$$

at time t is governed by the *heat equation*

$$(\partial_t + \Delta)h(t,p) = 0 \ .$$

One can show that there exists a function $k(t,p,q) \in C^\infty(\mathbb{R}^+ \times M \times M)$ satisfying

$$\begin{aligned}(\partial_t + \Delta_p)k(t,p,q) &= 0 \ , \\ \lim_{t \to 0} \int k(t,p,q)h(q)\,dq &= h(p) \ ,\end{aligned}$$

where ∂_t denotes differentiation with respect to t and Δ_p denotes the Laplacian acting in the p variable. The function $k(t,p,q)$ is called *heat kernel.* Let now H_t be the integral operator defined by

$$H_t h(p) = \int_M k(t,p,q)h(q)\,dq \ ,$$

then $h(t,p) = H_t h(p)$ satisfies the heat equation. Consequently H_t takes an initial heat distribution $h(p)$ to the heat distribution $h(t,p)$ at time t. The operator H_t is called *heat operator.*

The heat kernel can be computed by the formula

$$k(t,p,q) = \sum_i e^{-\lambda_i t}\phi_i(p)\phi_i(q) \ , \tag{6.1}$$

where λ_i and ϕ_i are the eigenvalues and eigenfunctions of Δ. Since Δ is invariant under isometries, equation (6.1) shows that this is also true for the heat kernel. Moreover, the metric can be computed from the heat kernel by the formula

$$\lim_{t \to \infty} t \log k(t,p,q) = -\frac{1}{4}d^2(p,q) \ ,$$

where $d(p,q)$ denotes the geodesic distance between two points $p, q \in M$. Thus, for a given manifold M, the information contained by the heat kernel and the metric are equivalent. Another important property of the heat kernel is its multi-scale property. For the heat kernel t plays the role of a spatial scale of influence, i. e. $k(t,p,\cdot)$ depends mainly on small neighborhoods of p for small t, whereas $k(t,p,\cdot)$ is influenced by larger neighborhoods of p for larger t.

The HKS is defined in [SOG09] to be the function $HKS \in C^\infty(\mathbb{R}^+ \times M)$ given by

$$HKS(t,p) = k(t,p,p) \ . \tag{6.2}$$

Since the heat kernel is much more complex than the HKS, one might expect to loose a lot of information when regarding the HKS instead of the heat kernel. But, as shown in [SOG09], the metric can be reconstructed from the HKS under quite weak assumptions. This means that the HKS of a positive definite tensor field contains almost all information of the tensor field.

Relation to Curvature

In order to obtain a more intuitive understanding of the HKS we study its relation to the curvature of the manifold M. For small values of the time parameter t the HKS has the row expansion

$$HKS(t,p) = \frac{1}{4\pi t}\sum_{i=1}^{\infty} u_i(p)t^i \ . \tag{6.3}$$

The general form of the functions $u_i(p)$ is discussed in [Ros97]. For the two-dimensional manifolds considered in this chapter the first three functions can be written as

$$\begin{aligned} u_0(x) &= 1 \ , \\ u_1(x) &= \frac{1}{3}K(p) \ , \\ u_2(x) &= \frac{1}{45}\left(4K(p)^2 - 3\Delta K(p)\right) \ , \end{aligned}$$

where K is the Gaussian curvature of M. Consequently, for a small value of t, the value of the HKS consists mainly of $\frac{1}{3}K$ plus a constant. The derivation of the stated u_i from the general case can be found in Appendix A.2.

6.2 HKS for Tensor Fields

The HKS introduced in Section 6.1 is defined for any compact, oriented Riemannian manifold. Thus the HKS is not restricted to surfaces embedded in some $\mathbb{R}^d$. If we have a metric tensor g, i. e. a symmetric positive definite tensor field, defined on a region $U \subset \mathbb{R}^d$, then (U, g) forms a Riemannian manifold. Since there is a Riemannian manifold associated with a positive definite tensor field in this way, we can compute the HKS for any positive definite tensor field. In this section the relation of the HKS for surfaces and positive definite tensor fields is illustrated by considering a parametrized surface and the pullback of its metric. Moreover, a mapping of the tensor field is suggested in order to apply the HKS for indefinite tensor fields.

Let $f : \mathbb{R}^2 \supset U \to \mathbb{R}^3$ be a parametrized surface. On the one hand, we can compute the HKS for the surface $f(U)$. On the other hand, we can define the metric tensor g on U at each point $p \in U$ by

$$g(p) \;:\; \mathbb{R}^2 \times \mathbb{R}^2 \to \mathbb{R} \;, \quad (v, w) \mapsto \langle [Jf(p)]v \,,\, [Jf(p)]w \rangle \;, \tag{6.4}$$

where $Jf(p)$ denotes the Jacobian of f at p and $\langle \cdot\,,\cdot \rangle$ the standard inner product on $\mathbb{R}^3$. That is, g is the pullback $f^*\langle \cdot\,,\cdot \rangle$ of $\langle \cdot\,,\cdot \rangle$ by f. The components of $g(p)$ are given by $g_{ij}(p) = ([Jf(p)]^T [Jf(p)])_{ij}$.

This makes (U, g) a Riemannian manifold which is isometric to $f(U)$ (equipped with the metric induced by the inner product $\langle \cdot\,,\cdot \rangle$ of $\mathbb{R}^3$) and f the associated isometry. Now we can compute the HKS directly on U by using g as metric. This is equivalent to computing the HKS on the surface $f(U)$ and then pull it back to the parameter space U by f, i. e.

$$HKS_U(t, p) = HKS_{f(U)}(t, f(p)) \;,$$

where HKS_U and $HKS_{f(U)}$ denote the HKS on U and $f(U)$, respectively. In other words: The diagram in Figure 6.1 commutes.

Figure 6.1 also shows that the HKS of (U, g) (bottom left) is a meaningful visualization of the metric. Thus we are interested in a method for computing the HKS directly for tensor fields, so that no embedded surface with the tensor field as metric tensor needs to be constructed. Such a method is proposed in Section 6.3.

Indefinite Tensor Fields

In order to compute the HKS for an indefinite tensor field, we can map the tensor field to a positive definite tensor field using a positive and monotonic function, e. g. the exponential function. Let T be a two-dimensional symmetric tensor field, $\lambda_1 \leq \lambda_2$ its eigenvalues and U the orthogonal matrix, such that

$$T = U^T \begin{bmatrix} \lambda_1 & \\ & \lambda_2 \end{bmatrix} U \;.$$

Now, for any positive, monotonic function $h : \mathbb{R} \to \mathbb{R}$ the mapped Tensor $h(T)$ is defined by

$$h(T) = U^T \begin{bmatrix} h(\lambda_1) & \\ & h(\lambda_2) \end{bmatrix} U \;.$$

The tensor $h(T)$ is now positive definite while its eigenvector fields remain unchanged.

The selection and parametrization of the mapping h influences the HKS. Thus this choice has to be made carefully, but as the example in Section 6.4 shows, for reasonably chosen mappings the results are quite similar.

6.3 Numerical Realization

Apparently, the HKS has been used only for triangulated surfaces, so far. We want to use the HKS for the visualization of two-dimensional symmetric positive definite tensor fields T defined on a rectangular region $U \subset \mathbb{R}^2$. Thus we need a method to compute the HKS of T or, more precisely, of the Riemannian manifold (U, T) associated with T. A finite element method for solving this problem is proposed in this section. Moreover, the boundary conditions are discussed and the correctness of the results is checked numerically.

From equation (6.1) follows that we can compute the heat kernel signature by the formula

$$HKS(t,p) = \sum_i e^{-\lambda_i t} \phi_i(p) \phi_i(p) \ ,$$

where λ_i and ϕ_i are the eigenvalues and eigenfunctions of the Laplacian Δ on (U, T). Thus we need a suitable discretization of Δ. A first idea was to adapt the Laplacian from the framework of discrete exterior calculus, see [DKT06], which is closely related to the cotangent Laplacian and widely used for triangulated surfaces. This discretization makes intensive use of edge lengths. However, triangulating the domain U and computing edge lengths by the metric g results in triangles which might not even satisfy the triangle inequality. Thus there seems to be no easy modification of this approach. Instead, a finite element method to compute the eigenvalues of the Laplacian is proposed.

According to Section 6.2 we can think of T as the metric of a surface in local coordinates. In this case the Laplacian is given by

$$\Delta f = \frac{1}{\sqrt{|T|}} \operatorname{div}\left(\sqrt{|T|}\, T^{-1} \nabla f\right)$$

for any function $f \in C^\infty(M)$, where div and ∇ denote the divergence and the gradient on U, respectively. Hence we have to solve the eigenvalue equation

$$\frac{1}{\sqrt{|T|}} \operatorname{div}\left(\sqrt{|T|}\, T^{-1} \nabla \phi\right) = \lambda \phi \ ,$$

or equivalently

$$\operatorname{div}\left(\sqrt{|T|}\, T^{-1} \nabla \phi\right) = \lambda \sqrt{|T|}\, \phi \ .$$

The weak formulation of this problem is given by

$$\int_U \operatorname{div}\left(\sqrt{|T|}\, T^{-1} \nabla \phi\right) \psi \, dp = \lambda \int_U \sqrt{|T|}\, \phi \psi \, dp$$

while this equation must hold for every smooth function ψ. We can rewrite the left hand side to

$$\begin{aligned}
&\int_U \operatorname{div}\left(\sqrt{|T|}\,T^{-1}\nabla\phi\right)\psi\,dp \\
&= \int_U \operatorname{div}\left(\sqrt{|T|}\,T^{-1}(\nabla\phi)\psi\right)dp - \int_U \left\langle \sqrt{|T|}\,T^{-1}\nabla\phi\,,\nabla\psi\right\rangle dp \\
&= \int_{\partial U} \left\langle \sqrt{|T|}\,T^{-1}(\nabla\phi)\psi\,,n\right\rangle dp - \int_U \left\langle \sqrt{|T|}\,T^{-1}\nabla\phi\,,\nabla\psi\right\rangle dp \ ,
\end{aligned}$$

where n denotes the outward pointing normal of the boundary. If we apply Neumann boundary conditions, i. e. $\langle\nabla\phi\,,n\rangle = 0$, the first term vanishes. Finally, we have to solve the equation

$$\int_U \left\langle \sqrt{|T|}\,T^{-1}\nabla\phi\,,\nabla\psi\right\rangle dp = -\lambda \int_U \sqrt{|T|}\,\phi\psi\,dp \ .$$

Choosing basis functions h_i the stiffness matrix L and the mass matrix M are given by

$$\begin{aligned}
L_{ij} &= \int_U \left\langle \sqrt{|T|}\,T^{-1}\nabla h_i\,,\nabla h_j\right\rangle dp \ , \\
M_{ij} &= -\int_U \sqrt{|T|}\,h_i h_j\,dp \ ,
\end{aligned}$$

and we solve the generalized eigenvalue equation

$$Lv = \lambda M v \ .$$

In our examples the tensor fields are given on regular grids and we use bilinear basis functions h_k.

Boundary Conditions

Usual boundary conditions like Dirichlet or Neumann boundary conditions influence the HKS significantly. In particular, for large time values the influence is not limited to the immediate vicinity of the boundary. Neumann boundary conditions cause the HKS to have higher values close to the boundary; their physical meaning is that the heat is perfectly insulated. Dirichlet boundary conditions cause the HKS to have a fixed value at the boundary. To overcome this problem we reflect a part of the field at the boundary. Now we can use Neumann boundary conditions for the sake of simplicity and obtain a significantly reduced influence of the boundary, see Figure

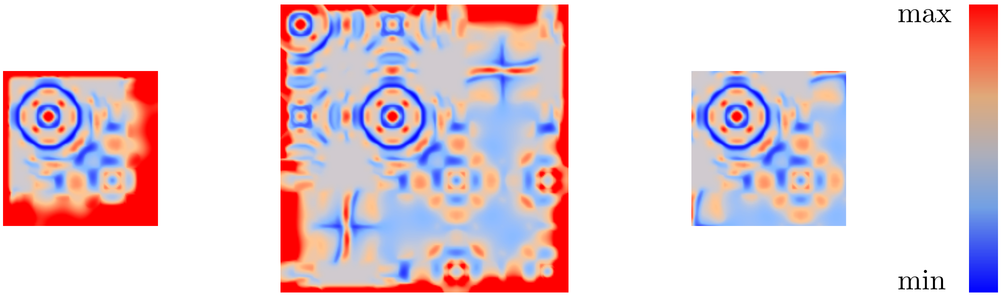

Figure 6.2: *The result of the two point load dataset on the left is strongly influenced by the boundary. This effect can be reduced significantly by reflecting a portion of the tensor field on the boundary (middle) and cropping the result (right).*

6.2. The physical meaning of these reflected boundaries is that the heat at the boundary can diffuse outwards in the same way than inwards.

Numerical Verification

We check the correctness of the FEM described above experimentally by comparing the HKS for a surface with the pull back of its metric, i. e. the commutativity of Figure 6.1 is reflected by our verification. Consider a bumpy torus parametrized by

$$f(u,v) = \begin{bmatrix} cos(u)\,(r_1(u) + r_2(v)cos(v)) \\ sin(u)\,(r_1(u) + r_2(v)cos(v)) \\ r_2(v)sin(v) \end{bmatrix} \; ,$$

where the radii are modulated, i. e. major radius and minor radius are given by $r_1(u) = 3 + \frac{1}{2}cos(10u)$ and $r_2(v) = 1 + \frac{1}{5}cos(8v)$, respectively. This results in the surface that is also used in Figure 6.1. The metric of the bumpy torus is computed on $[0, 2\pi]^2$ by formula (6.4) and the resulting tensor field is sampled with four different resolutions of 50^2, 100^2, 200^2 and 400^2 points. For this four datasets the HKS is computed with the FEM described above. The results are compared with the HKS for the bumpy torus given as a triangulated surface with 400^2 points, while the HKS is computed by the standard FEM Laplacian for triangulated surfaces, see e. g. [ZvKD10]. If we denote the HKS for the tensor field by HKS_T and for surfaces by HKS_S, the relative difference for $t = 1$ is given by

$$\frac{\|HKS_T(1,\cdot) - HKS_S(1,\cdot)\|_{L_2}}{\|HKS_S(1,\cdot)\|_{L_2}} = \frac{\left(\int_{[0,2\pi]^2} \left(HKS_T(1,x) - HKS_S(1,x)\right)^2\, dx\right)^{\frac{1}{2}}}{\left(\int_{[0,2\pi]^2} \left(HKS_S(1,x)\right)^2\, dx\right)^{\frac{1}{2}}} \; .$$

Resolution	50^2	100^2	200^2	400^2
Relative difference	0.38369	0.07599	0.00920	0.00075

Table 6.1: *Relative difference between HKS for tensors and surfaces.*

See Table 6.1 for the relative difference between HKS_T for different resolutions and HKS_S. It is obvious that HKS_T approaches HKS_S quickly for increasing resolutions.

6.4 Results

Several results of this method are shown in this section. In the following we investigate the significance of the HKS and the meaning of Gaussian curvature in the general tensor context. To get a more intuitive understanding, the influence of the eigenvalues and eigenvectors on the HKS is analyzed by considering synthetic tensor fields with constant eigenvectors and eigenvalues, respectively. Isolated degenerate points are considered, as they are central structural components of the eigenvector fields. As real world example the method is applied to a diffusion tensor data set of the brain. Moreover, a two-dimensional slice of a two point load dataset is considered as an example for an indefinite stress tensor field. To investigate the sensitivity with respect to the mapping function, two mappings with various parametrizations are used. During the whole section the colormap shown in Figure 6.2 is used, which ranges from the minimum to the maximum over all results in one figure, unless otherwise stated.

Figure 6.3 shows easy examples of diagonal tensor fields, i. e. $T_{12} = 0$. These fields serve as examples of tensor fields with variable eigenvalues but constant eigenvectors. For the tensor field $T^{(1)}$, where component $T^{(1)}_{11}$ is a Gaussian function depending on u_1 and $T^{(1)}_{22}$ is constant, the HKS is constant. The field $T^{(2)}$ is very similar to $T^{(1)}$, the only difference is that $T^{(2)}_{11}$ depends on u_2. In this case the HKS is not constant anymore. To understand this we consider the formula (6.3) for $t = 1$, i. e.

$$HKS(1,p) = \frac{1}{4\pi}\left(1 + \frac{1}{3}K(p) + \frac{1}{45}\left(4K(p)^{(2)} - 3\Delta K(p)\right) + \dots\right) \quad , \tag{6.5}$$

while the Gaussian curvature for diagonal T is given by

$$K = -\frac{1}{2\sqrt{T_{11}T_{22}}}\left(\partial_{u_1}\frac{\partial_{u_1}T_{22}}{\sqrt{T_{11}T_{22}}} - \partial_{u_2}\frac{\partial_{u_2}T_{11}}{\sqrt{T_{11}T_{22}}}\right) \quad . \tag{6.6}$$

Consequently, if $\partial_{u_1}T_{22} = 0$ and $\partial_{u_2}T_{11} = 0$ we have $K = 0$ and thus $HKS(1, x)$ is constant for $T^{(1)}$. The tensor field $T^{(3)}$ has components $T^{(3)}_{11}$ and $T^{(3)}_{22}$ depending on

u_2 and u_1, respectively, consequently both diagonal components have influence on the HKS. The field $T^{(4)}$ satisfies $T^{(4)}_{11} = T^{(4)}_{22}$ where $T^{(4)}_{11}$ and $T^{(4)}_{22}$ depend radially on u. As expected, the HKS depends also radially on u.

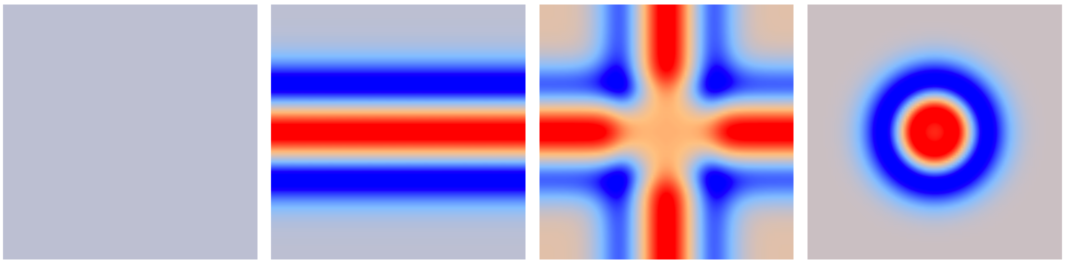

$T^{(1)} = \begin{pmatrix} f(u_1) & \\ & 1 \end{pmatrix}$ $T^{(2)} = \begin{pmatrix} f(u_2) & \\ & 1 \end{pmatrix}$ $T^{(3)} = \begin{pmatrix} f(u_2) & \\ & f(u_1) \end{pmatrix}$ $T^{(4)} = \begin{pmatrix} f(|u|) & \\ & f(|u|) \end{pmatrix}$

Figure 6.3: *HKS of diagonal tensor fields for small* t. *The function* f *is given by* $f(x) = 1 + 10e^{-x^2}$ *and the tensor fields are defined for* $u \in [-5, 5]^2$.

The HKS for tensor fields with constant eigenvalues and variable eigenvectors is shown in Figure 6.4. These fields are defined by choosing fixed eigenvalues and a variable major eigenvector field, which is visualized by some integral lines. We observe that the HKS is also influenced by the eigenvectors and has high values in compressing regions and low values in expanding regions. This shows that the HKS for a certain time value is not a scalar invariant (cf. Section 2.3), since it does not only depend on the eigenvalues.

In Figure 6.5 we consider degenerate points of tensor fields with indices between -2 and 3. The index *ind* is defined to be the number of rotations of the eigenvector fields along a curve enclosing the degenerate point (and no other degenerate points). For a more formal definition see [DH94]. The results show that the HKS also hints at topological features like degenerate points, although there seems to be no obvious way to derive the tensor field topology from the HKS.

An example of the HKS for a symmetric positive definite tensor field is given in Figure 6.6, a diffusion tensor dataset of a brain. Instead of using the diffusion tensor T itself we consider the metric $g = T^{-1}$. Large eigenvalues of the diffusion tensor correspond to high diffusivity in direction of the respective eigenvector, whereas small eigenvalues correspond to low diffusivity. Since a high diffusivity should reflect small distances, considering the inverse tensor is a natural way of assigning a metric to a diffusion tensor. For a detailed discussion see [OHW02]. The HKS is evaluated for different time steps. Although the extraction of a single slice might discard valuable information, the structure of the brain becomes obvious by the HKS. The defined metric implies that blue regions (low values) reflect high diffusivity, whereas red regions (high values) reflect low diffusivity. Moreover, the time parameter t allows to focus on small- as well as large-scale structures.

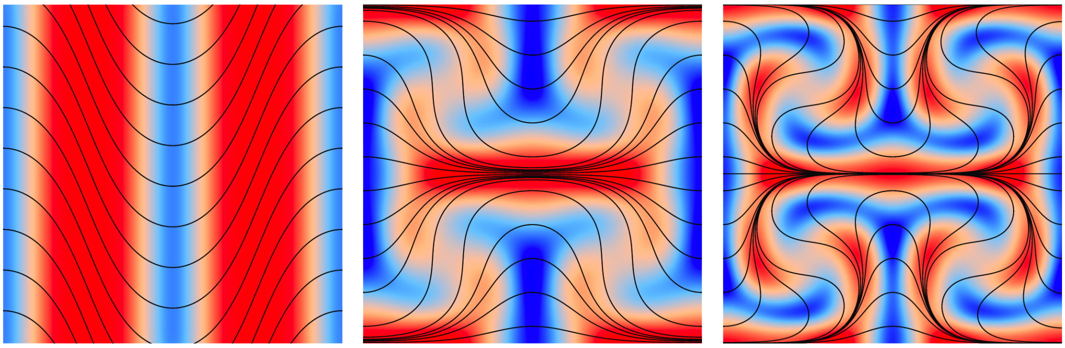

$\begin{bmatrix} \cos\left(\frac{3}{8}\pi\sin(2\pi x)\right) \\ \sin\left(\frac{3}{8}\pi\sin(2\pi x)\right) \end{bmatrix}$ $\begin{bmatrix} \cos\left(\frac{\pi}{2}\sin(2\pi x)\sin(2\pi y)\right) \\ \sin\left(\frac{\pi}{2}\sin(2\pi x)\sin(2\pi y)\right) \end{bmatrix}$ $\begin{bmatrix} \cos\left(\pi\sin(2\pi x)\sin(2\pi y)\right) \\ \sin\left(\pi\sin(2\pi x)\sin(2\pi y)\right) \end{bmatrix}$

Figure 6.4: *Tensor fields defined on* $[0,1]^2$ *by constant eigenvalues and an anlytic major eigenvector field (see caption). The HKS is shown for small* t *and the major eigenvector field is visualized by some integral lines. The dependency of the HKS on the eigenvectors demonstrates its difference to scalar invariants. The colormap ranges from the minimum to the maximum of the single images.*

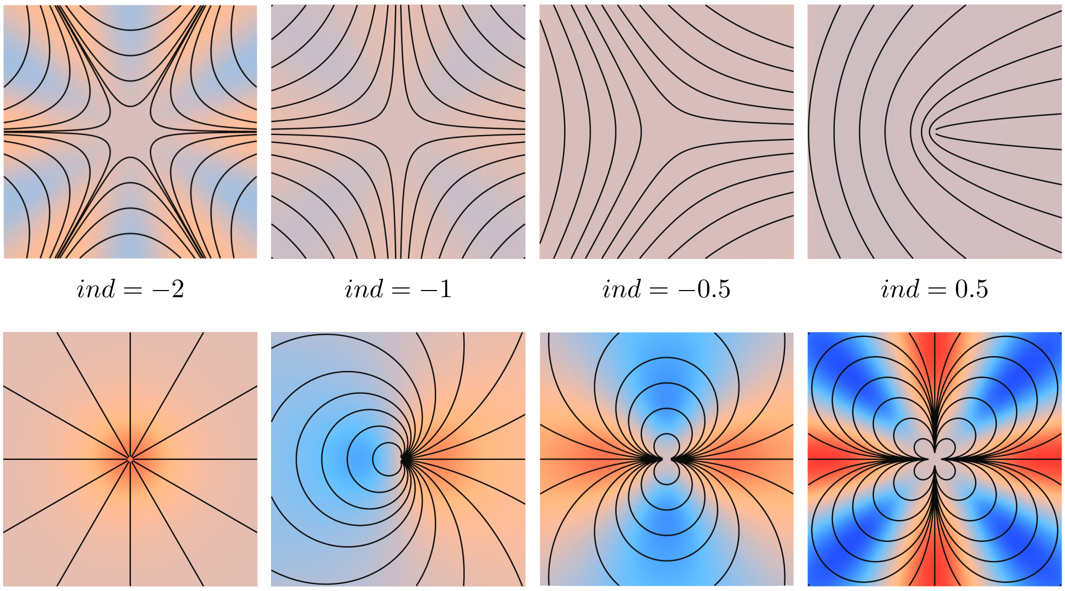

$ind = -2$ $ind = -1$ $ind = -0.5$ $ind = 0.5$

$ind = 1$ $ind = 1.5$ $ind = 2$ $ind = 3$

Figure 6.5: *HKS of degenerate points with different index* ind *for small* t*. The tensor field is defined on* $u \in [-1,1]^2$ *and the eigenvalues are given by* $10 + 3|u|$ *and* $10 - 3|u|$.

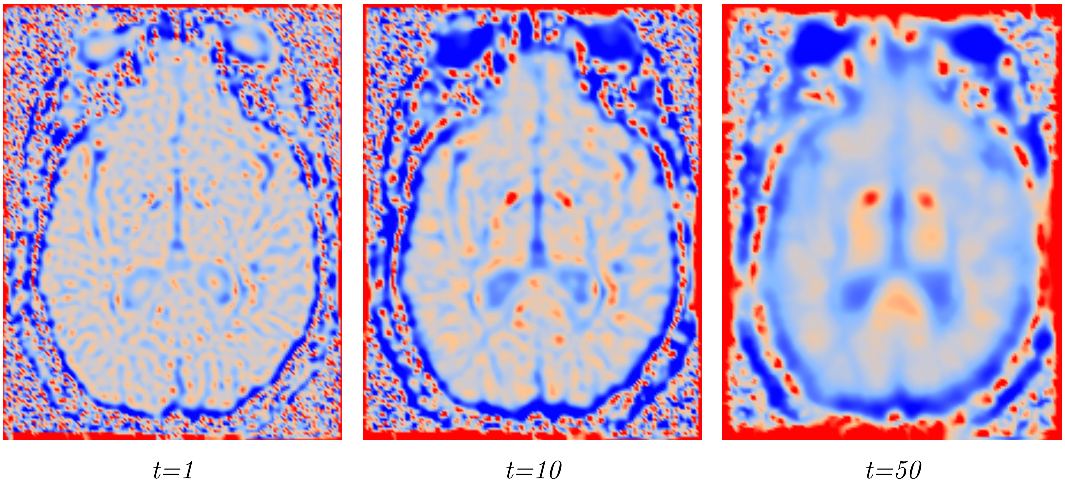
t=1 t=10 t=50

Figure 6.6: *HKS of a brain dataset*^{0} *for different* t*. The inverse of the diffusion tensor is considered. The colormap ranges from the minimum (blue) to the maximum (red) of each individual image.*

As a last example, we consider numerical experiments with an indefinite stress tensor field. The used example is a two-dimensional slice of a two point load dataset with one pushing and one pulling force. To investigate the sensitivity with respect to the mapping function, two mappings with various parametrizations are used. In Figure 6.7 the exponential mapping is used to obtain a positive definite tensor field. The HKS is evaluated for different time steps. Very similar results are obtained if the tensor field is scaled with 0.01 before applying the mapping, i. e. we consider the tensor field $\exp(0.01T)$, see Figure 6.8. We observe that the scaling has very little influence on the result. In Figure 6.9 and Figure 6.10 the arc tangent mapping is applied to the tensor field. The tensor field is scaled with 0.1 and 0.001, respectively, and shifted by $\frac{\pi}{2}$ to obtain a positive definite field, i. e. we consider $\arctan(0.1T) + \frac{\pi}{2}$ and $\arctan(0.001T) + \frac{\pi}{2}$. Using this mapping, the influence of the scaling is bigger than for the exponential mapping. Nevertheless, all results are rather similar for reasonable chosen mappings, which justifies this approach.

6.5 Conclusion and Future Work

Applying the HKS to tensor fields serves as a new method for the visualization of tensor fields. Compared to common scalar invariants like the trace or the determi-

---

[0] Dataset courtesy of Gordon Kindlmann at the Scientific Computing and Imaging Institute, University of Utah, and Andrew Alexander, W. M. Keck Laboratory for Functional Brain Imaging and Behavior, University of Wisconsin-Madison

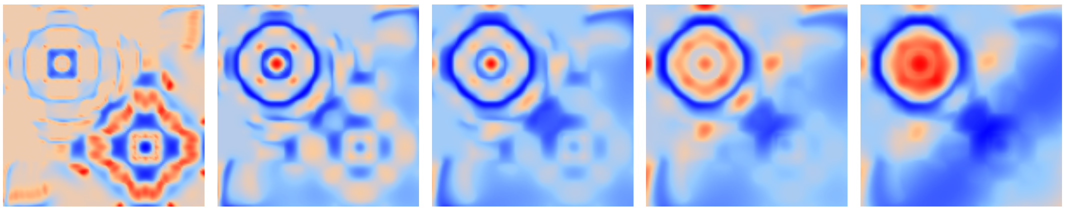

$t=0.1$ $t=1$ $t=2$ $t=5$ $t=10$

Figure 6.7: *HKS of a two point load dataset mapped by* $\exp(T)$.

$t=0.1$ $t=1$ $t=2$ $t=5$ $t=10$

Figure 6.8: *HKS of a two point load dataset mapped by* $\exp(0.01T)$.

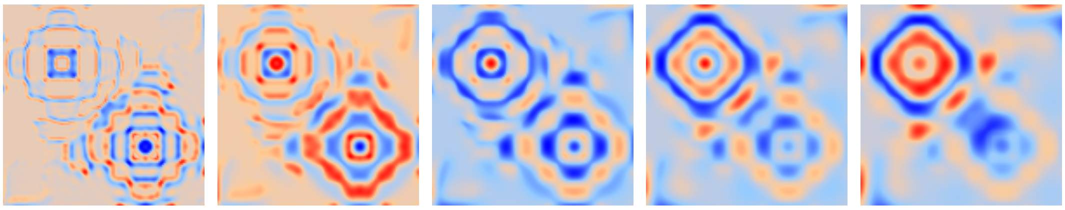

$t=0.1$ $t=1$ $t=2$ $t=5$ $t=10$

Figure 6.9: *HKS of a two point load dataset mapped by* $\arctan(0.1T)$.

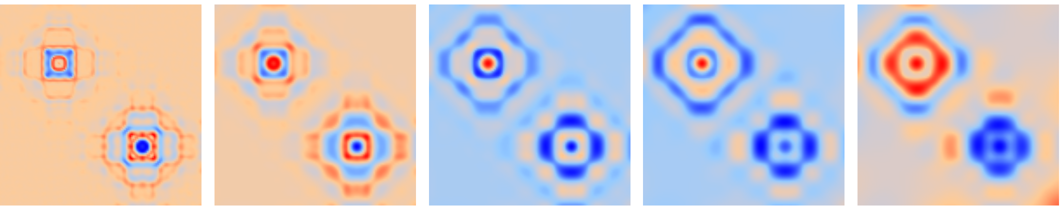

$t=0.1$ $t=1$ $t=2$ $t=5$ $t=10$

Figure 6.10: *HKS of a two point load dataset mapped by* $\arctan(0.001T)$.

nant it provides additional information, as Figure 6.4 shows. A special strength of the method is its inherent level of detail property. Thus, it is possible to emphasize smaller or larger structures. In contrast to naive Gaussian smoothing the scaling is directly driven by the tensor data itself. For diffusion tensor data the results are very promising. For other applications, the significance of the HKS demands further investigations.

If the HKS is directly used for visualization, its interpretation might be difficult, but the HKS for tensor fields can also be used for its original purpose. As the HKS characterizes the metric of a Riemannian manifold at a point, the HKS can be also used for the detection of similar points of a tensor field. This offers a wide range of applications ranging from image registration to feature detection.

Also an extension to three-dimensional tensor fields is desirable, since due to the projection of three-dimensional tensors on two-dimensional slices much valuable information is lost. From a theoretical point of view the method can be generalized easily to three-dimensional tensor fields. With the exception of the formulas indicating the relation to Gaussian curvature, all formulas are valid in higher dimensions. The problem is that the computation of the eigenvalues of the Laplacian takes very long for most three-dimensional data. The computation of the first 500 eigenvalues for a dataset with 256^2 points already takes a few minutes, thus the computation time for a dataset with 256^3 points will not be feasible. For tensor fields defined on surfaces a generalization is also no problem from a theoretical point of view, but in this case the interpretation is even more difficult. The HKS of the standard metric on the surface results in the usual HKS for surfaces, i. e. the HKS is influenced not only by the tensor field but also by the surface itself.

7

Thesis Conclusion

The goal of this thesis was the visual analysis of second and third order tensor fields. Tensor fields from structural mechanics served as the major example, especially stress tensor fields. Four new methods were proposed, showing different approaches and motivations for the visualization of tensor fields. The first two methods were motivated by applications and developed in close collaboration with mechanical engineers. The second two methods were mainly driven by theoretical considerations. Different techniques were employed to solve the respective tasks. Features and scalar quantities were defined in order to reveal global structures of tensor fields. Local methods, namely tensor glyphs, were used for an in-depth analysis of tensor fields.

The objective of the method proposed in Chapter 3 was to show the engineer how far a given fiber orientation strengthens a component under a given load condition. The major challenge was to combine the two tensor fields which respectively define stresses and fiber orientations, and show them in an comprehensible way. This led to a feature based visualization which indicates where the fiber orientation should be improved. Moreover, a glyph was used for a closer inspection. It shows admissible fiber directions and the fiber orientation tensor at the same time. This application demonstrates that there is a demand for user-specific methods in tensor field visualization. For example, there are glyphs that encode the complete tensor information, but it would be very hard for an engineer to obtain the desired information from them. But the features defined here are able to tell the engineer if a certain fiber orientation is suitable for the given stressing condition. And the stress tensor is visualized by showing the admissible fiber directions under the respective stressing condition, an information which is hard to read from other glyphs used for stress tensor visualization.

Chapter 4 aimed at the visualization of gradients of stress tensor fields, as the gradient might also have an effect on the stability of a material. This is particularly challenging because the gradient of a second order tensor field is a third order tensor field. Almost no methods are available to visualize such tensors. Well-known depictions of stress tensors served as a basis for designing glyphs for stress gradients, in order to simplify the interpretation. Due to the large amount of information contained in the stress gradient, several simplifications were proposed in order to emphasize certain properties.

Starting point of Chapter 5 was the observation that most applications rely on the analysis of tensor fields using scalar invariants. This led to the idea of analyzing the complete invariant part of a tensor. A major contribution is the theoretical result that the proposed extremal points are the same for several meaningful sets of tensor invariants. Consequently, extremal points serve as important features of tensor fields, as they include minima and maxima of multiple widely-used scalar invariants. Thus the extremal points are characteristic for the invariant part of a tensor field. Moreover, if the focus is on extrema of scalar invariants, then analysis can be restricted to the extremal points, i. e. the problem is reduced to a lower dimensional subset.

The method proposed in Chapter 6 is also mainly based on theoretical considerations. As the Heat Kernel Signature (HKS) is well suited for the characterization of shapes, it was desirable to employ it for the analysis of tensor fields. A numerical method was proposed in order to compute the HKS for two-dimensional tensor fields. Due to the time parameter of the HKS it is possible to visualize tensor fields on different scales. Additionally, apart from visualization the HKS might be used for the detection of similar points in tensor fields.

The variety of the proposed methods reflect the challenge of visualizing tensor fields. As it is not possible to show the complete information of a three-dimensional tensor field in a comprehensible way, a single method will hardly be perfect for any tensor field. Thus a reduction of the information is necessary, while it depends on the application which properties of the field are relevant. Accordingly, the visual analysis of tensor fields demands for application specific methods. Also a combination of different methods seems mandatory for a comprehensive analysis of a tensor field.

A

Appendix

A.1 Jacobian Matrices of Tensor Invariants

The rows of the Jacobian matrices of $\bar{I}$, $\bar{K}$, $\bar{R}$ are the gradients of the respective invariant functions, i. e.

$$\begin{aligned} J\bar{I} &= \begin{bmatrix} \nabla\bar{I}_1 & \nabla\bar{I}_2 & \nabla\bar{I}_3 \end{bmatrix}^\top \ , \\ J\bar{K} &= \begin{bmatrix} \nabla\bar{K}_1 & \nabla\bar{K}_2 & \nabla\bar{K}_3 \end{bmatrix}^\top \ , \\ J\bar{R} &= \begin{bmatrix} \nabla\bar{R}_1 & \nabla\bar{R}_2 & \nabla\bar{R}_3 \end{bmatrix}^\top \ . \end{aligned}$$

The gradients of the invariant functions depending on the eigenvalues $\lambda_1, \lambda_2, \lambda_3$ are given by

$$\nabla\bar{I}_1 = \nabla\bar{K}_1 = \begin{bmatrix} 1 \\ 1 \\ 1 \end{bmatrix} \ , \quad \nabla\bar{I}_2 = \begin{bmatrix} \lambda_2 + \lambda_3 \\ \lambda_1 + \lambda_3 \\ \lambda_1 + \lambda_2 \end{bmatrix} \ ,$$

$$\nabla\bar{I}_3 = \begin{bmatrix} \lambda_2\lambda_3 \\ \lambda_1\lambda_3 \\ \lambda_1\lambda_2 \end{bmatrix} \ , \quad \nabla\bar{K}_2 = \begin{bmatrix} \frac{1}{\|\tilde{T}\|}\tilde{\lambda}_1 \\ \frac{1}{\|\tilde{T}\|}\tilde{\lambda}_2 \\ \frac{1}{\|\tilde{T}\|}\tilde{\lambda}_3 \end{bmatrix} \ ,$$

$$\nabla\bar{R}_2 = \begin{bmatrix} \frac{1}{\sqrt{6}}\|T\|^{-3}\|\tilde{T}\|^{-1}(\operatorname{tr} T)(\lambda_1\lambda_2 + \lambda_1\lambda_3 - \lambda_2^2 - \lambda_3^3) \\ \frac{1}{\sqrt{6}}\|T\|^{-3}\|\tilde{T}\|^{-1}(\operatorname{tr} T)(\lambda_2\lambda_1 + \lambda_2\lambda_3 - \lambda_1^2 - \lambda_3^3) \\ \frac{1}{\sqrt{6}}\|T\|^{-3}\|\tilde{T}\|^{-1}(\operatorname{tr} T)(\lambda_3\lambda_1 + \lambda_3\lambda_2 - \lambda_1^2 - \lambda_2^3) \end{bmatrix} \ ,$$

$$\nabla \bar{K}_3 = \nabla \bar{R}_3 = \begin{bmatrix} \sqrt{6}\|\tilde{T}\|^{-5}(\lambda_2-\lambda_3)^2(\lambda_1-\lambda_2)(\lambda_1-\lambda_3) \\ \sqrt{6}\|\tilde{T}\|^{-5}(\lambda_1-\lambda_3)^2(\lambda_2-\lambda_1)(\lambda_2-\lambda_3) \\ \sqrt{6}\|\tilde{T}\|^{-5}(\lambda_1-\lambda_2)^2(\lambda_3-\lambda_1)(\lambda_3-\lambda_2) \end{bmatrix} .$$

A.2 Row expansion of the Heat Kernel Signature

The row expansion of the HKS for small values of t is given by

$$HKS(t,p) = \frac{1}{4\pi t}\sum_{i=1}^{\infty} u_i(p)t^i \ .$$

In the general case the functions u_i are given by

$$\begin{aligned} u_0(p) &= 1 \ , \\ u_1(p) &= \frac{1}{6}R(p) \ , \\ u_2(p) &= \frac{1}{360}\left(2R_{ijkl}R^{ijkl}(p) + 2R_{jk}R^{jk}(p) + 5R^2(p) - 12\Delta R(p)\right) \ , \end{aligned}$$

where R_{ijkl} is the Riemann curvature Tensor, $R_{jk} = R^i_{jik}$ the Ricci tensor and $R = R^j_j$ the Ricci scalar or scalar curvature. For surfaces these tensors can be written in terms of the Gaussian curvature by

$$\begin{aligned} R_{ijkl} &= K(g_{ik}g_{jl} - g_{il}g_{jk}) \ , \\ R_{jk} &= Kg_{jk} \ , \\ R &= 2K \ . \end{aligned}$$

Thus we find

$$\begin{aligned} R_{ijkl}R^{ijkl} &= K(g_{ik}g_{jl} - g_{il}g_{jk})K(g^{ik}g^{jl} - g^{il}g^{jk}) \\ &= K^2\left(g_{ik}g_{jl}g^{ik}g^{jl} - g_{ik}g_{jl}g^{il}g^{jk} - g_{il}g_{jk}g^{ik}g^{jl} + g_{il}g_{jk}g^{il}g^{jk}\right) \\ &= K^2\left(\delta^i_i\delta^j_j - \delta^l_k\delta^k_l - \delta^l_k\delta^k_l + \delta^i_i\delta^j_j\right) \\ &= K^2\left(4-2-2+4\right) = 4K^2 \ , \end{aligned}$$

$$R_{jk}R^{jk} = K^2 g_{jk}g^{jk} = K^2\delta^j_j = 2K^2 \ ,$$

And consequently the functions u_i can be expressed in terms of K by

$$\begin{aligned}
u_0(p) &= 1 \ , \\
u_1(p) &= \frac{1}{3}K(p) \ , \\
u_2(p) &= \frac{1}{45}\big(4K(p)^2 - 3\Delta K(p)\big) \ .
\end{aligned}$$

Bibliography

[BAH13] Andrea Brambilla, Øyvind Andreassen, and Helwig Hauser. Integrated multi-aspect visualization of 3d fluid flows. In *Proc. of VMV 2013: Vision, Modeling & Visualization*, pages 1–9, Sept. 2013.

[BG68] R.L. Bishop and S.I. Goldberg. *Tensor Analysis on Manifolds.* Dover Books on Mathematics. Dover Publications, 1968.

[BK10] M.M. Bronstein and I. Kokkinos. Scale-invariant heat kernel signatures for non-rigid shape recognition. In *Computer Vision and Pattern Recognition (CVPR), 2010 IEEE Conference on*, pages 1704–1711. IEEE, 2010.

[BKC+13] Rita Borgo, Johannes Kehrer, David H Chung, Eamonn Maguire, Robert S Laramee, Helwig Hauser, Matthew Ward, and Min Chen. Glyph-based visualization: Foundations, design guidelines, techniques and applications. *Eurographics State of the Art Reports*, pages 39–63, 2013.

[Boo86] W.M. Boothby. *An introduction to differentiable manifolds and Riemannian geometry.* Academic Press Inc, 1986.

[BW08] Sven Bachthaler and Daniel Weiskopf. Continuous scatterplots. *IEEE Transactions on Visualization and Computer Graphics*, 14(6):1428–1435, 2008.

[BWN+15] Harsh Bhatia, Bei Wang, Gregory Norgard, Valerio Pascucci, and Peer-Timo Bremer. Local, smooth, and consistent jacobi set simplification. *Computational Geometry*, 48(4):311–332, 2015.

[CHDH00] John C Criscione, Jay D Humphrey, Andrew S Douglas, and William C Hunter. An invariant basis for natural strain which yields orthogonal stress response terms in isotropic hyperelasticity. *Journal of the Mechanics and Physics of Solids*, 48(12):2445–2465, 2000.

[CJTI95] Joaquim S Cintra Jr and Charles L Tucker III. Orthotropic closure approximations for flow-induced fiber orientation. *Journal of Rheology (1978-present)*, 39(6):1095–1122, 1995.

[DC76] Manfredo Perdigao Do Carmo. *Differential geometry of curves and surfaces*, volume 2. Prentice-hall Englewood Cliffs, 1976.

[DGBW09] Christian Dick, Joachim Georgii, Rainer Burgkart, and Rüdiger Westermann. Stress tensor field visualization for implant planning in orthopedics. *Visualization and Computer Graphics, IEEE Transactions on*, 15(6):1399–1406, 2009.

[DH94] Thierry Delmarcelle and Lambertus Hesselink. The topology of symmetric, second-order tensor fields. In *Proceedings of the conference on Visualization'94*, pages 140–147. IEEE Computer Society Press, 1994.

[DKT06] Mathieu Desbrun, Eva Kanso, and Yiying Tong. Discrete differential forms for computational modeling. In *SIGGRAPH '06: ACM SIGGRAPH 2006 Courses*, pages 39–54, New York, NY, USA, 2006. ACM.

[dLGALW09] Rodrigo de Luis-García, Carlos Alberola-López, and Carl-Fredrik Westin. Segmentation of tensor fields: Recent advances and perspectives. In *Tensors in Image Processing and Computer Vision*, pages 35–58. Springer, 2009.

[DLL$^+$10] T.K. Dey, K. Li, C. Luo, P. Ranjan, I. Safa, and Y. Wang. Persistent heat signature for pose-oblivious matching of incomplete models. In *Computer Graphics Forum*, volume 29, pages 1545–1554. Wiley Online Library, 2010.

[DT06] Issam Doghri and Laurent Tinel. Micromechanics of inelastic composites with misaligned inclusions: numerical treatment of orientation. *Computer methods in applied mechanics and engineering*, 195(13):1387–1406, 2006.

[EH02] Herbert Edelsbrunner and John Harer. Jacobi sets of multiple morse functions. *Foundations of Computational Mathematics, Minneapolis*, pages 37–57, 2002.

[EK06] Daniel B Ennis and Gordon Kindlmann. Orthogonal tensor invariants and the analysis of diffusion tensor magnetic resonance images. *Magnetic Resonance in Medicine*, 55(1):136–146, 2006.

[GZZ$^+$11] Xiaosheng Gao, Tingting Zhang, Jun Zhou, Stephen M Graham, Matthew Hayden, and Charles Roe. On stress-state dependent plasticity modeling: significance of the hydrostatic stress, the third invariant of stress deviator and the non-associated flow rule. *International Journal of Plasticity*, 27(2):217–231, 2011.

[HFH$^+$04] Ingrid Hotz, Louis Feng, Hans Hagen, Bernd Hamann, Boris Jeremic, and Kenneth I. Joy. Physically based methods for tensor field visualization. In *VIS '04: Proceedings of IEEE Visualization 2004*, pages 123–130. IEEE Computer Society Press, oct 2004.

[HG06] Hans Hagen and Christoph Garth. An introduction to tensors. In *Visualization and Processing of Tensor Fields*, pages 3–13. Springer, 2006.

[Hil50] Rodney Hill. *The mathematical theory of plasticity*, volume 11. Oxford university press, 1950.

[Hol00] Gerhard A Holzapfel. *Nonlinear solid mechanics*, volume 24. Wiley Chichester, 2000.

[HSH07] Mario Hlawitschka, Gerik Scheuermann, and Bernd Hamann. Interactive glyph placement for tensor fields. In *Advances in Visual Computing*, pages 331–340. Springer, 2007.

[HYW$^+$03] Youssef Hashash, John I Yao, Donald C Wotring, et al. Glyph and hyperstreamline representation of stress and strain tensors and material constitutive response. *International journal for numerical and analytical methods in geomechanics*, 27(7):603–626, 2003.

[JS04] David A Jack and Douglas E Smith. Assessing the use of tensor closure methods with orientation distribution reconstruction functions. *Journal of composite materials*, 38(21):1851–1871, 2004.

[JSF$^+$02] Boris Jeremić, Gerik Scheuermann, Jan Frey, Zhaohui Yang, Bernd Hamann, Kenneth I Joy, and Hans Hagen. Tensor visualizations in computational geomechanics. *International Journal for Numerical and Analytical Methods in Geomechanics*, 26(10):925–944, 2002.

[Kai13] Jan-Martin Kaiser. *Beitrag zur mikromechanischen Berechnung kurzfaserverstärkter Kunststoffe-Deformation und Versagen.* PhD thesis, Universität des Saarlandes, 2013.

[KASH13] Andrea Kratz, Cornelia Auer, Markus Stommel, and Ingrid Hotz. Visualization and Analysis of Second-Order Tensors: Moving Beyond the Symmetric Positive-Definite Case. *Computer Graphics Forum - State of the Art Reports*, 32(1):49–74, 2013.

[KEWW07] Gordon Kindlmann, Daniel B Ennis, Ross T Whitaker, and Carl-Fredrik Westin. Diffusion tensor analysis with invariant gradients and rotation tangents. *Medical Imaging, IEEE Transactions on*, 26(11):1483–1499, 2007.

[KfW06] G. Kindlmann and C. f. Westin. Diffusion tensor visualization with glyph packing. *IEEE Transactions on Visualization and Computer Graphics*, 12(5):1329–1336, Sept 2006.

[Kin04] Gordon Kindlmann. Superquadric tensor glyphs. In *Proceedings of the Sixth Joint Eurographics-IEEE TCVG conference on Visualization*, pages 147–154. Eurographics Association, 2004.

[KKH11] Andrea Kratz, Nino Kettlitz, and Ingrid Hotz. Particle-based anisotropic sampling for two-dimensional tensor field visualization. In *Proceedings of Vision, Modeling, and Visualization.* The Eurographics Association, 2011.

[KSZ$^+$14] Andrea Kratz, Marc Schoeneich, Valentin Zobel, Ingrid Hotz, Bernhard Burgeth, Gerik Scheuermann, and Markus Stommel. Tensor visualization driven mechanical component design. In *IEEE Pacific Visualization Symposium*, pages 145–152. IEEE, 2014.

[KYHR05] RD Kriz, M Yaman, M Harting, and AA Ray. Visualization of zeroth, second, fourth, higher order tensors, and invariance of tensor equations. *Computer Graphics*, 21(6), 2005.

[Mag85] Jan R Magnus. On differentiating eigenvalues and eigenvectors. *Econometric Theory*, 1(02):179–191, 1985.

[MRK03] Ian Milne, Robert O Ritchie, and Bhushan L Karihaloo. *Comprehensive structural integrity: cyclic loading and fatigue*, volume 4. Elsevier, 2003.

[OBBG09] M. Ovsjanikov, A.M. Bronstein, M.M. Bronstein, and L.J. Guibas. Shape google: a computer vision approach to isometry invariant shape retrieval. In *Computer Vision Workshops (ICCV Workshops), 2009 IEEE 12th International Conference on*, pages 320–327. IEEE, 2009.

[OHW02] Lauren O'Donnell, Steven Haker, and Carl-Fredrik Westin. New approaches to estimation of white matter connectivity in diffusion tensor mri: Elliptic pdes and geodesics in a tensor-warped space. In *International Conference on Medical Image Computing and Computer-Assisted Intervention*, pages 459–466. Springer, 2002.

[PPVWS95] Frits H Post, Frank J Post, Theo Van Walsum, and Deborah Silver. Iconic techniques for feature visualization. In *Proceedings of the 6th conference on Visualization'95*, page 288. IEEE Computer Society, 1995.

[PYW$^+$16] J. Palacios, H. Yeh, Wenping Wang, Yue Zhang, R. S. Laramee, R. Sharma, T. Schultz, and E. Zhang. Feature surfaces in symmetric tensor fields based on eigenvalue manifold. *IEEE Transactions on Visualization and Computer Graphics*, 22(3):1248–1260, March 2016.

[Rad13] Dieter Radaj. *Ermüdungsfestigkeit: Grundlagen für Leichtbau, Maschinen-und Stahlbau.* Springer-Verlag, 2013.

[RBBK10] D. Raviv, M.M. Bronstein, A.M. Bronstein, and R. Kimmel. Volumetric heat kernel signatures. In *Proceedings of the ACM workshop on 3D object retrieval*, pages 39–44. ACM, 2010.

[Ros97] S. Rosenberg. *The Laplacian on a Riemannian manifold: an introduction to analysis on manifolds.* Cambridge Univ Pr, 1997.

[SD03] MN Som and SC Das. *Theory and practice of foundation design.* PHI Learning Pvt. Ltd., 2003.

[SK10] Thomas Schultz and Gordon L Kindlmann. Superquadric glyphs for symmetric second-order tensors. *Visualization and Computer Graphics, IEEE Transactions on*, 16(6):1595–1604, 2010.

[SN09] Heinz Schade and Klaus Neemann. *Tensoranalysis.* Walter de Gruyter, 2009.

[SN11] N Suthambhara and Vijay Natarajan. Simplification of jacobi sets. In *Topological Methods in Data Analysis and Visualization*, pages 91–102. Springer, 2011.

[SOG09] J. Sun, M. Ovsjanikov, and L. Guibas. A concise and provably informative multi-scale signature based on heat diffusion. In *Proc. Eurographics Symposium on Geometry Processing (SGP)*, 2009.

[TKW08] Xavier Tricoche, Gordon Kindlmann, and Carl-Fredrik Westin. Invariant crease lines for topological and structural analysis of tensor fields. *IEEE Transactions on Visualization and Computer Graphics*, 14(6):1627–1634, 2008.

[TS04] Xavier Tricoche and Gerik Scheuermann. Topology simplification of symmetric, second-order 2d tensor fields. In *Geometric Modeling for Scientific Visualization*, pages 275–291. Springer, 2004.

[TSH01] Xavier Tricoche, Gerik Scheuermann, and Hans Hagen. Tensor topology tracking: A visualization method for time-dependent 2d symmetric tensor fields. *Computer Graphics Forum*, 20:461–470, 2001.

[TW71] Stephen W Tsai and Edward M Wu. A general theory of strength for anisotropic materials. *Journal of composite materials*, 5(1):58–80, 1971.

[vM13] R. von Mises. Mechanik der festen Körper im plastisch-deformablen Zustand. *Nachrichten von der Gesellschaft der Wissenschaften zu Göttingen, Mathematisch-Physikalische Klasse*, 1913:582–592, 1913.

[WPG$^+$97] Carl-Fredrik Westin, Sariel Peled, Hakon Gudbjartsson, Ron Kikinis, Ferenc A Jolesz, et al. Geometrical diffusion measures for mri from tensor basis analysis. *ISMRM '97*, page 1742, 1997.

[ZP04] Xiaoqiang Zheng and Alex Pang. Topological lines in 3d tensor fields. In *Visualization, 2004. IEEE*, pages 313–320. IEEE, 2004.

[ZPP05a] X. Zheng, B. Parlett, and A. Pang. Topological structures of 3d tensor fields. In *Visualization, 2005. VIS 05. IEEE*, pages 551–558, Oct 2005.

[ZPP05b] X. Zheng, B. N. Parlett, and A. Pang. Topological lines in 3d tensor fields and discriminant hessian factorization. *IEEE Transactions on Visualization and Computer Graphics*, 11(4):395–407, July 2005.

[ZRH14] Valentin Zobel, Jan Reininghaus, and Ingrid Hotz. Visualization of two-dimensional symmetric positive definite tensor fields using the heat kernel signature. In *Topological Methods in Data Analysis and Visualization III*, pages 249–262. Springer, 2014.

[ZRH15] Valentin Zobel, Jan Reininghaus, and Ingrid Hotz. Visualizing symmetric indefinite 2d tensor fields using the heat kernel signature. In *Visualization and Processing of Higher Order Descriptors for Multi-Valued Data*, pages 257–267. Springer, 2015.

[ZS17] Valentin Zobel and Gerik Scheuermann. Extremal curves and surfaces in symmetric tensor fields. *The Visual Computer*, 2017.

[ZSS15] Valentin Zobel, Markus Stommel, and Gerik Scheuermann. Feature-based tensor field visualization for fiber reinforced polymers. In *2015 IEEE Scientific Visualization Conference (SciVis)*, pages 49–56. IEEE, 2015.

[ZSS17] Valentin Zobel, Markus Stommel, and Gerik Scheuermann. Visualizing gradients of stress tensor fields. In *Modeling, Analysis, and Visualization of Anisotropy*, pages 65–81. Springer, 2017.

[ZvKD10] H. Zhang, O. van Kaick, and R. Dyer. Spectral mesh processing. In *Computer Graphics Forum*. John Wiley & Sons, 2010.